Investigations in

Real-Time Confocal Microscopy

by

Cian M. Taylor

A thesis submitted for the degree of Doctor of Philosophy

at the University of Dublin

Department of Pure and Applied Physics

Trinity College Dublin

University of Dublin

Dublin 2

October 2001
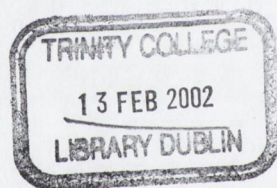
Declaration

This thesis has not been submitted as an excerise for a degree at any other University. The work described is entirely my own, except for the assistance mentioned in the acknowledgements and the collaborative work noted in the list of publications. I agree that Trinity College Library may lend or copy this thesis on request.

Cian Taylor

Cian M. Taylor

SUMMARY

This thesis is a study of imaging in real-time confocal imaging systems. The particular instrument examined is the direct-view microscope (DVM), an instrument which allows real-time confocal imaging through the use of an array of pinholes rather than the usual single pinhole. The emphasis is placed on the depth sectioning side of the imaging: the greatest advantage offered by confocal systems, and also on the use of coherent illumination sources in such systems.

We begin by introducing the elementary theory underlying all equations used in the thesis. The theory is both scalar and paraxial and describes the imaging accurately in systems of low angular aperture. The operation of the DVM in fluorescence mode is first studied. We experimentally examine the predictions of the scalar diffraction theory with respect to source coherence in such systems. Predictions of the theory are verified by employing a further paraxial modification of the usual equations to account for the non-ideal nature of our experimental setup. We make some broad comments about the general trade-offs between coherent and incoherent sources in fluorescence direct-view microscopy.

We next present a novel design for a programmable DVM which uses a pair of ferroelectric liquid crystal spatial light modulators to achieve confocal operation. Limitations of the system are discussed. The system employs a coherent source and we present examples of the effects of such source coherence on the depth imaging. We derive equations describing the depth response of a DVM employing square rather than the usual circular apertures and describe the effects of this on the imaging. Finally, we present recorded images before moving on to describe an implementation of throughput enhancing aperture correlation for the system.

We continue a theoretical analysis of effects of source coherence in brightfield direct-view microscopy. Effects of source coherence which have not previously been described are presented. By examining the infinite array limit of such systems we make some general comments about the depth imaging, in particular with regard to the use of rectangular arrays. We discuss the particular dimensions of rectangular arrays which are likely to exhibit quality imaging.
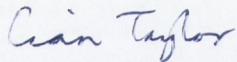
Finally, we present a novel design for a confocal endoscope employing a coherent fibre bundle and an array of variable focal length microlenses. A preliminary investigation of the feasibility of the design is performed and possible improvements are presented.

Acknowledgements

The work presented in this thesis would not have been possible without the help of many people in the optoelectronics group at Trinity.

Firstly, I am indebted to Professor Eithne McCabe for suppling the resources for my work and travel and for an excellent introduction to the field of confocal microscopy. Her encouragement and guidance is greatly appreciated. I would also like to thank Dr. Dave Fewer for providing me with an introduction to experimental aspects of confocal microscopy during an all too short overlap between our times at Trinity. In addition, his excellent thesis served as an invaluable source of reference relavent to much of the work. Thanks to Dr. Paddy Smith who joined our group in 1998 and provided me with invaluable support and expertise. Thanks also for life-changing introductions to both Linux and LaTeX. I am grateful to Dr. Christophe Jordan for help in the early days and to Dr. Alan Dalton for a quick tutorial in the art of thin-film manufacture.

Credit is due to both Professor John Hegarty and Dr. John Donegan for the inception and maintenance of an excellent optoelectronics research group. For financial assistance and provision of resources I would like to thank Trinity College, Optronics Ireland, and Enterprise Ireland. Thanks also to the Trinity College Travel fund for funding my travel and to the Centre for Supercomputing in Ireland for providing me with access to a state-of-the-art parallel processor network. Also, thanks to Professor Adrian Ottewill for help with code optimisation and for allowing me access to an additional fast parallel computer.

For me, Trinity has always been an enjoyable place to work and that is due to the relaxed atmosphere created by the people who work/worked there: thanks to Stephen Lynch, Fergal McAleavey, Tom Aherne, Adrian Donohoe, Gary Laird, Tom McCormack, Stephanie Lanne, Louise Bradley, Fred Logue, Richie Paul, Eamonn Murphy, Brendan Roycroft, Cedric Medea, Anaïs Champenois, John Patchell, Canice O'Brien, Daire Byrne, Hèrve Folliot, Paul McEvoy, Declan Byrne, Tara Kavanagh, Pascal Landais, Karl Boylan, Richard Phelan, Adrian Lavin, Michaël Lecoutre, Shane Robinson, Dave McDonald, Dave Martin, James O'Gorman, Vincent Weldon, & Mick Lynch.

On a personal note, I owe a debt of sanity to Andrea for her limitless support and her infectious 'glass half-full' attitude. Also thanks to Gerry, Eddie, Barry and Alan for some memorable times which always distracted me from work.

Finally, I would like to thank my parents Maureen and David for their love and support over many years of study and my brothers Fergus, Ronan, and Donal for not ever wanting to talk about Physics.

Contents

iv

Chapter 1

Introduction

The first reference to the use of a refracting object to magnify a subject is attributed to Seneca and dates from the 1st century BC. After observation of a page of text through a water-filled glass globe he remarked: "Letters, however small and indistinct, are seen enlarged and more clearly … ". The more sophisticated use of solid refracting objects such as polished gem stones (the first recorded direct precursor of modern day lenses) was remarked on by Pliny the Elder between 23-79 AD: "Emeralds are usually concave so that they may concentrate the visual rays. The emperor Nero used to watch, in an emerald, the gladatorial combats". This apparent reference to the use of an emerald monocle to correct for near-sightedness, although widely-read in some circles at the time, did not lead to an explosion in the use of lenses for correction of sight. In fact, it was not until the 13th century that the use of spectacles became wide-spread. It was then only a matter of time before two spectacle lenses were combined together to form the first compound microscope, the progenitor of all modern-day optical microscopes.

The actual discovery was erroneously credited to Galileo Galilei and also Antonie van Leeuwenhoek but it is now generally accepted that the the first such instrument was constructed by Dutchman Zacharias Janssen around 1595. The design is thought to have been derived from that of an early refracting telescope constructed in reverse. The 17th and early 18th centuries produced some great mechanical improvements for the microscope, making it much more sturdy and easy to use. However the images obtained

remained rather blurry with colorful halos around the objects. These imaging artifacts were found to be due to both chromatic and aspheric (spherical) aberration [1] and the first to address them was Chester More Hall who in the 1730s invented the achromatic doublet. This element took advantage of the fact that a convex lens made of crown glass has reciprocal dispersion properties to a concave lens of flint glass [2]. Thus, a balancing of the chromatic dispersion could be achieved.

The problem of spherical aberration remained however until 1830 when Joseph Jackson Lister showed mathematically that the use of a multi-element lens, consisting of a series of low power lenses placed precise distances from each other, could greatly reduce spherical aberration. Even with correction for chromatic and spherical aberration, early microscopists faced another conundrum: it was noticed that some lenses exhibited superior resolution to others. Empirically, it was noted that resolution seemed to increase with the angular aperture of the lens. The exact relationship remained a mystery until the 1870s when Ernst Abbe, working for Carl Zeiss, presented his formula for the minimum resolvable distance, d [2].

$$d = \frac{\lambda}{2n\sin\alpha},\qquad(1.1)$$

with λ being the illumination wavelength and α the half-angle of the cone of light subtended by the lens. The factor $n\sin\alpha$ represents the numerical aperture (NA) of the lens with n denoting the refractive index of the immersion medium between the lens and the sample. By the 1880s, the use of high aperture immersion lenses brought the resolution limits for optical microscopes down to $\sim 0.25\mu$m, essentially what they remain today in non-specialised microscopes. Abbe's resolution limit for a lens is a result of diffraction effects at the finite-sized lens pupil and is a fundamental limit for a lens. There are however a number of ways in which resolution in microscopes can be improved beyond this limit, one of which, confocal microscopy, is the subject of this thesis.

1.1　Choice of instrument

The ability to examine sub-micron features in a wide variety of samples is an essential tool vital to much of the research being performed by the scientific community today. The trade-offs which exist between the advantages and disadvantages of the various different types of microscopes must be carefully considered before choosing the particular system relevant to the research involved. For example, if resolution on the nanometre scale is required, an electron microscope [3] could be employed: in theory the resolution is limited by diffraction and the ultra short (de Broglie [4]) wavelength of an electron beam ensures extremely high resolution (see Equation (1.1)). In practice, aberrations which result from the use of non-ideal electron lenses ensures the resolution does not approach the diffraction limit but is, nevertheless, an improvement on optical microscopes. This method has the cost of potential degradation of the sample due to the invasive and time-consuming sample preparation required to achieve image contrast.

An alternative to electron microscopy which also affords resolution within the classical optical diffraction limit is near-field microscopy [5, 6]. A tiny aperture is placed very close to the surface of the sample to be imaged. If the aperture is close enough to the sample (within the evanescent fields), then the resolution is determined by the size of the aperture rather than by diffraction. In practice, tapered fibre tips are often used in near-field microscopes and resolutions of $20 - 30$nm are commonly achieved [7]. However, this technique can only be used if sample surface topography varies on a very small scale ($\sim<$ 1nm). In cases where more modest resolutions are required then a 'conventional' optical microscope may be the tool of choice.

Traditionally, in a conventional optical microscope, images would be viewed directly through the eyepiece and indeed for many applications it is entirely satisfactory to operate the microscope in this way. There are however some cases where direct-viewing of a sample is either impossible or undesirable. For example, if a laser is used to illuminate the sample then it may be too dangerous to allow light reflected from the

3

object to fall directly on the eye. In addition, if procedures such as particle sizing and counting are to be performed then a computer algorithm operating on a digitised image would certainly be more trustworthy than a strained human eye. Finally, many resolution enhancement algorithms are available which can allow improved image contrast. Therefore, a more versatile instrument may be one in which the images are sampled and recorded on digital media. One microscope implementation which is well suited towards the recording of digital images is the scanning optical microscope.

1.2   Scanning optical microscopes

The first scanning optical microscope was reported by Young and Roberts in 1951 [8]. In their flying spot microscope, the light from the face of a flying spot scanner tube was directed through conventional microscope optics in reverse with the result that a tiny spot was focused onto a sample. The light transmitted by the sample was directed towards a photocell the output of which was used to modulate the intensity of a synchronously scanned TV display. Modern day scanning optical microscopes operate in a similar way. A (generally) diffraction-limited spot is scanned across the surface of a sample imaging it serially rather than in parallel. The magnification can be varied continuously simply by varying the total extent of the scan, with a lower limit which is imposed by the size of the diffraction-limited spot. Further, the sequential nature of the data acquisition makes the images obtained well suited to being digitised and thus suited to electronic post-processing. Scanning microscopes, while being generally more versatile than conventional microscopes, have identical imaging properties and thus all of the problems associated with conventional microscopes. The foremost of these may be the blur caused by light reflected/transmitted from out-of-focus regions of the sample. A not entirely satisfactory solution to this problem is the physical sectioning of samples into thin slices before mounting on the sample stage:– an invasive procedure which can perturb the very structure of the sample.

An elegant solution to this problem was first proposed by Minsky [9] who, in 1961,

first presented the confocal idea. In a memoir on his discovery [10] he describes how his desire to image the 3-D connections between neurons within brain matter (with a view to engineering an intelligent machine) led him to his discovery. Minsky realised that, with a conventional microscope it would not be possible to perform such a 3-D measurement due to the 'noise' which would result from cells outside the focal plane. He envisaged the ideal microscope as imaging a sample point by point with no interference from neighbouring points and implemented such an instrument by placing pinholes in the source and detector planes of a conventional scanning microscope. Before discussing the merits of this approach it is instructive to introduce some differ-
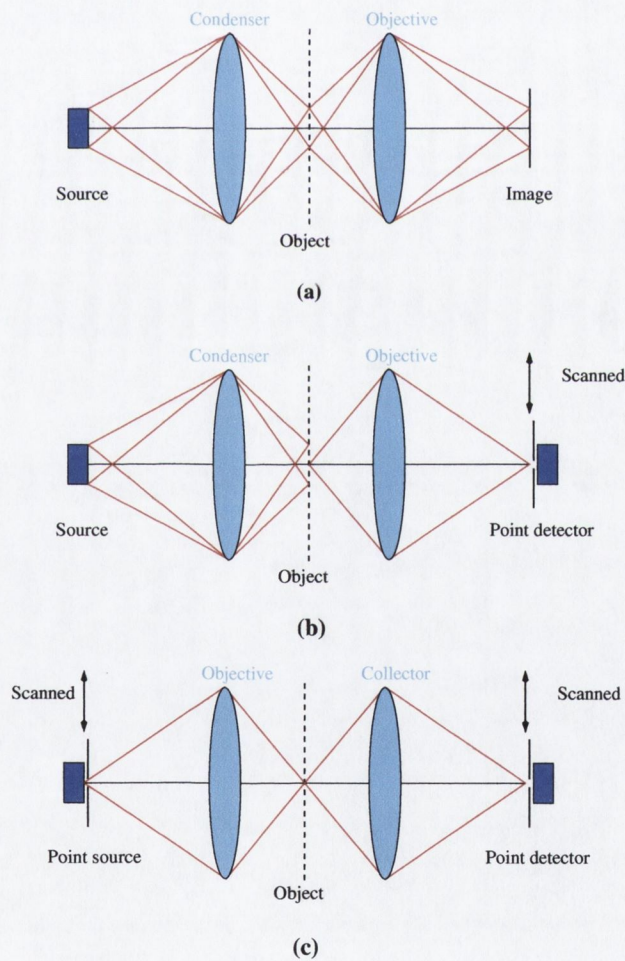
Figure 1.1: Scanning optical microscope arrangements. (a) Conventional (non-scanning) microscope; (b) Type 1 scanning microscope; (c) Type 2 or 'confocal' scanning microscope.

ent types of scanning microscope. Following Wilson and Sheppard [11] we introduce Figure 1.1. The figure shows microscopes operating in transmission mode, however the following arguments apply equally to those which operate in reflection mode. Figure 1.1 (a) depicts the standard optical setup for a conventional (non-scanning) optical microscope. An extended light source is focused by a condenser lens onto a wide area of an object. Light transmitted by the object is imaged by the objective lens, the image being viewed directly through an eyepiece lens. In this case, the resolution of the image is primarily dependent on the objective lens while the aberrations of the condenser lens are unimportant. Figure 1.1 (b) shows the setup of a microscope designated the Type 1 scanning optical microscope. In this case, the optical configuration differs from that of the conventional microscope only in that a point detector is placed in the image plane. The optical field in the image plane can be recorded by scanning the point detector transversely and such a setup is well suited towards the recording of digitised images. A matrix of intensities, each corresponding to a particular point in the image plane, is built up and sent to a storage medium. In this case the imaging properties are identical to the system featured in Figure 1.1 (a).

Part (c) of Figure 1.1 shows a scanning optical microscope which employs both a point source and a point detector. The point source is focused by the objective lens to illuminate a small area of the sample, the light intensity transmitted from this area is then registered at the point detector. In order to build up an extended image of the object, the source and detector are scanned transversely in synchronism. In this configuration both lenses play an equal role in the imaging and we might expect this fact to cause an improvement in resolution over a conventional microscope. Such a resolution enhancement is predicted by a principle due to Lukosz [12] which states that resolution can be improved at the expense of field of view. We note in the case of the Type 2 or confocal[1] scanning optical microscope (CSOM) featured in Figure 1.1 (c), the field of view is essentially the extent of a (generally) diffraction-limited spot

---

[1] So-called because both the objective and collector lenses are focused at the same point in the object.

and thus a resolution enhancement can be expected.

The lateral resolution of a CSOM is predicted by scalar diffraction theory to be improved over that of a conventional microscope by $\sim 29\%$. The equations which predict such an improvement are presented in some detail in Chapter 2. The actual resolution improvement itself is presented in Figure 2.3 for an instrument which is entirely analogous to the CSOM. Such a theory also predicts an even more striking benefit of the CSOM, its ability to preferentially image features within the focal plane of the objective lens. Thus, high quality 'optically sectioned' images of thick samples can be recorded; there is no longer a need for the physical sectioning of samples. The physical principle behind optical sectioning or 'depth sectioning' in a CSOM is demonstrated by Figure 1.2 [13].

Light emanating from a point source (red line) passes a beamsplitter and is imaged by an objective lens to form a tiny spot in the image plane. In the figure, the image plane is referred to as the focal plane, in reality this will be the case only when an infinity corrected objective is used in conjunction with collimating optics. If a reflecting sample, such as a plane mirror, is placed in the focal plane then the back reflected light (also depicted by red line) passes the lens and is (partially) reflected by the beamsplitter and focused to a point somewhere in the region of the detector. The confocal principle relies on the accurate positioning of a pinhole detector at the exact point where light reflected from the focal plane is focused. In this configuration, the point source and point detector are said to be at conjugate positions (relative to the objective lens). With the point detector so positioned, light from the focal plane of the objective is strongly detected whereas light from out-of-focus planes (blue line in figure) will be weakly detected at the detector. In practice, high NA objectives used in conjunction with low wavelength illumination can allow efficient detection of reflected light from a region of much less than $1\mu m$ either side of the focal plane. Figure 1.3 shows an example of the depth resolution obtainable in a confocal microscope. The curves represent the intensity recorded at the detector as a planar featureless sample (*e.g.* a plane mirror) is scanned through the focal plane of the objective lens. The point of zero defocus
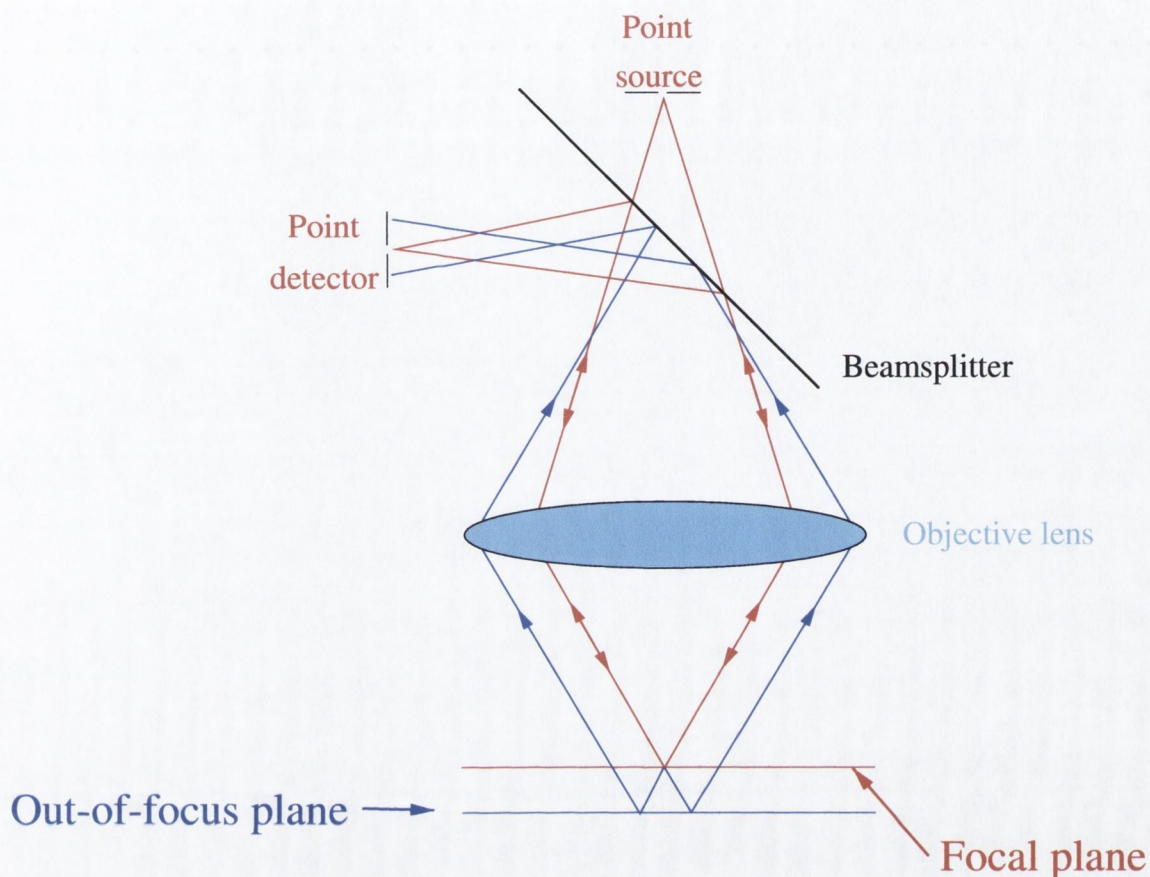
Figure 1.2:   The origin of depth sectioning.

corresponds to the planar sample being in the focal plane of the objective. The solid curve was calculated (using the theory described in Chapter 2) for a confocal microscope employing infinitesimal pinholes with laser illumination at 457.9nm and a ×50/0.6 NA objective lens. This curve is often called a 'depth response' or 'planar object response' and its full width at half maximum (FWHM) gives a measure of the depth resolution of the system. By comparison, the depth response of the conventional optical microscope (dashed line) shows no depth sectioning properties, being constant for all values of defocus.

In order to image an area greater than the size of the diffraction-limited spot, the object under inspection is generally scanned transversely relative to the stationary
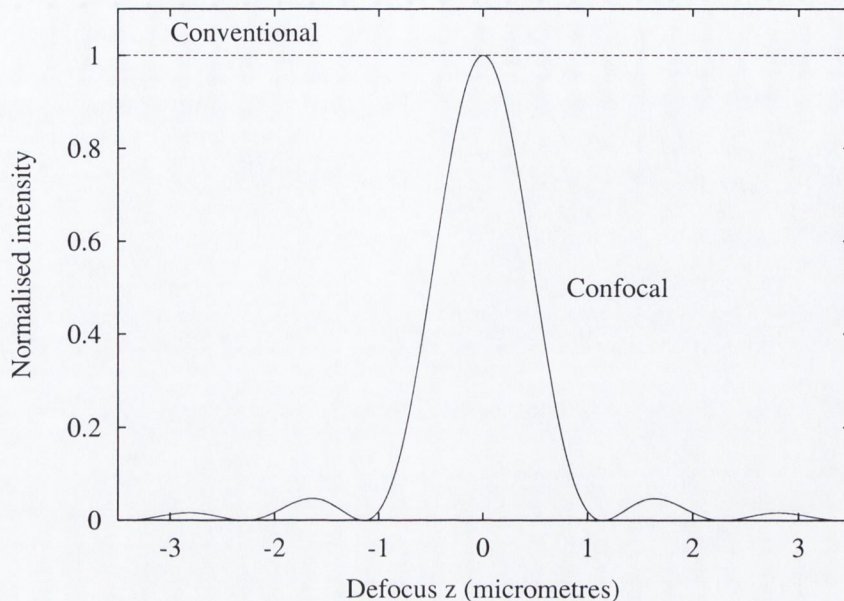
Figure 1.3: Depth sectioning in both conventional (dashed line) and confocal (solid line) microscopes. Predictions of scalar diffraction theory.

point source/detector. However, other scanning regimes, discussed in Section 1.3, are also possible. An example of a confocal image is presented in Figure 1.4 [14]. Part (a) of the figure shows a reflected light (brightfield) confocal image of a semiconductor laser. The bright sections of this image correspond to features of the sample which were at the focal plane of the objective lens when the image was recorded.

Other types of images are possible, for example in order to build up a picture of the surface topology of the sample, the following procedure can be performed: the sample is scanned axially. Each point in the sample is in the focal plane when it registers its highest intensity at the detector. The intensity at each point is recorded for every step during the axial scan, and a composite image containing the maximum value recorded at each point constructed. Such an image is called an auto-focus image [11, 15] and has the property of having all features in focus throughout an extended axial range which is limited only by the total extent of the axial scan. Figure 1.4 (b) shows an auto-focus image recorded of the sample featured in Figure 1.4 (a). The image shows

9
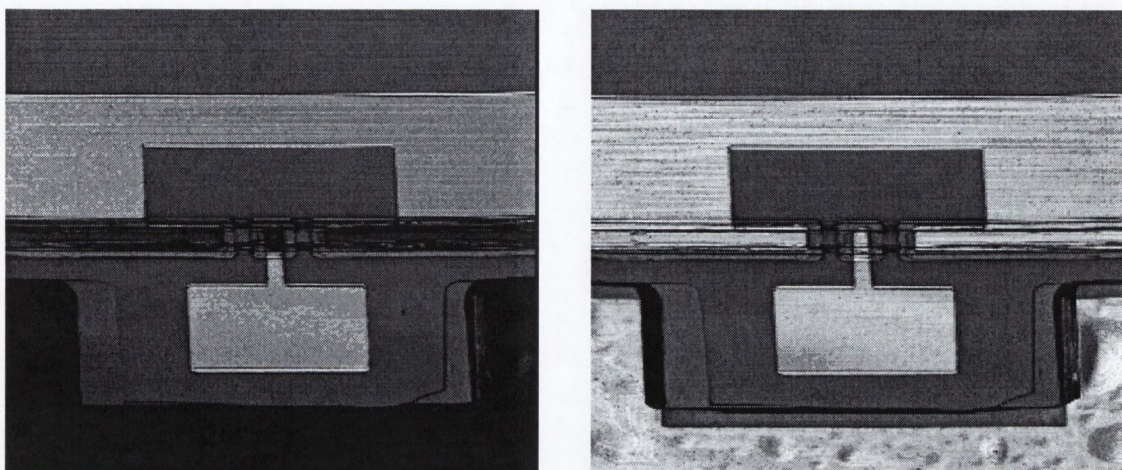
<div align="center">(a)   (b)</div>

Figure 1.4: Images of a semiconductor laser sample. (a) Confocal image; (b) auto-focus image.

a large depth of focus however unlike images recorded in a conventional microscope, all features in the auto-focus image appear sharply focused.

Other imaging modes are also possible, for example: while recording an auto-focus image, the axial position at which each maximum occurred could also be recorded so that the relative heights of features in the sample can be determined. Such an image is called a range-by-maximum image [11] and can be used in conjuction with an auto-focus image to build a 3-D plot of the sample.

1.3 Scanning techniques

The primary disadvantage of the CSOM is the time required for image acquisition. In some cases, where static events are being monitored and time is not a priority, raster scanning of the object is wholly satisfactory. The object is scanned relative to a stationary beam which has the advantage that cheap objective lenses without

corrections for off-axis aberration[2] can be used. With such scanning systems, the recording of an image typically takes between 1 and 4 seconds. Such a scanning regime can however place limits on the mass of the sample which can be imaged, due to its inertia, also the total maximum field of view obtainable can be restricted. Finally, the dead-time associated with raster scanning makes the imaging less than optimum.

It is also possible to mount the sample on a stationary stage; scanning of either the objective lens or the beam gives the required field of view. The former [16], while permitting the examination of bulky or heavy specimens, is still limited to scan times of a few seconds. Faster rates of image acquisition are possible in beam-scanning systems. For example, systems employing fast galvanometric mirrors [17] or acousto-optic beam deflectors [18] have been reported which enable image acquisition at video rates ($>$ 25Hz). Such imaging is often described as real-time in that the image is updated at rates faster than the human eye can perceive, in this thesis whenever we refer to real-time imaging systems it is meant in this sense. A disadvantage of real-time beam-scanning systems of the type mentioned above is that they generally require a more complicated optical arrangement and expensive objective lenses which include correction for off-axis aberrations.

Perhaps the most successful real-time microscope implementation which has come to light since the inception of the confocal microscope is the tandem-scanning microscope. This instrument is a step back towards conventional microscope design in that the imaging is again parallelised to a degree and, often, the sample is viewed directly with the naked eye via an eyepiece. Alternatively, the placement of any of the currently available 2-D detectors (such as a CCD camera) in the image plane of the eyepiece, allows digitised images to be taken without the need for point-by-point data collection.

---

[2]Departure of the wavefront from its ideal form predicted by ray or Gaussian optics [1].

1.4 The tandem-scanning, real-time, or direct-view microscope

The 'tandem-scanning reflected-light microscope' was first presented in the late 1960s by Egger and Petráň [19, 20]. Such an instrument employs an array of pinholes rather than the usual single pinhole and can deliver real-time quasi-confocal imaging. The imaging is parallelised to a degree, however, scanning of the pinhole array is still required in order to image a continuous field of view. In order to facilitate such scanning, the pinholes were arranged by Egger *et al.* on a thin circular disc in the form of interleaving Archimedean spirals which have a field filling property when rotated.

Such a configuration of pinholes is identical to the geometry of a disc invented by Nipkow in 1884 [21] which was used in the development of early television systems. The use of a Nipkow disc configuration of pinholes has the advantage of allowing very fast scanning of the pinhole array and thus very fast imaging rates are possible. The imaging has none of the dead-time associated with raster or galvanometric scanning however such systems are prone to mechanical wear and tear. In its original configuration, the tandem-scanning microscope was a two-sided instrument, using one sector of the Nipkow disc for illumination and an opposite sector for detection. Such a configuration requires a rather complicated optical system and also precise positioning of the pinholes throughout the disc so that illumination pinholes can be perfectly matched with detection pinholes. Further, the optical alignment required to achieve such matching is quite precise.

A somewhat simpler design for a similar instrument was presented in 1988 by Xiao *et al.* [22] as the real-time confocal scanning optical microscope. The optical configuration used by Xiao *et al.* was similar to that shown in Figure 1.5. A light source is used to illuminate the (spinning) Nipkow disc and light diverges from each of the illuminated pinholes. In the figure we have indicated the light diverging from only one pinhole for clarity. A tube lens collimates the light and an infinity corrected objective lens focuses an array of spots onto the sample. Light reflected from the sample traverses the same

Light source

Polariser →

Analyser ↓

Detector

Eyepiece

Beamsplitter

Nipkow
disc

Motor

Tube lens

Quarter-wave
plate

Objective lens

Illuminated
region
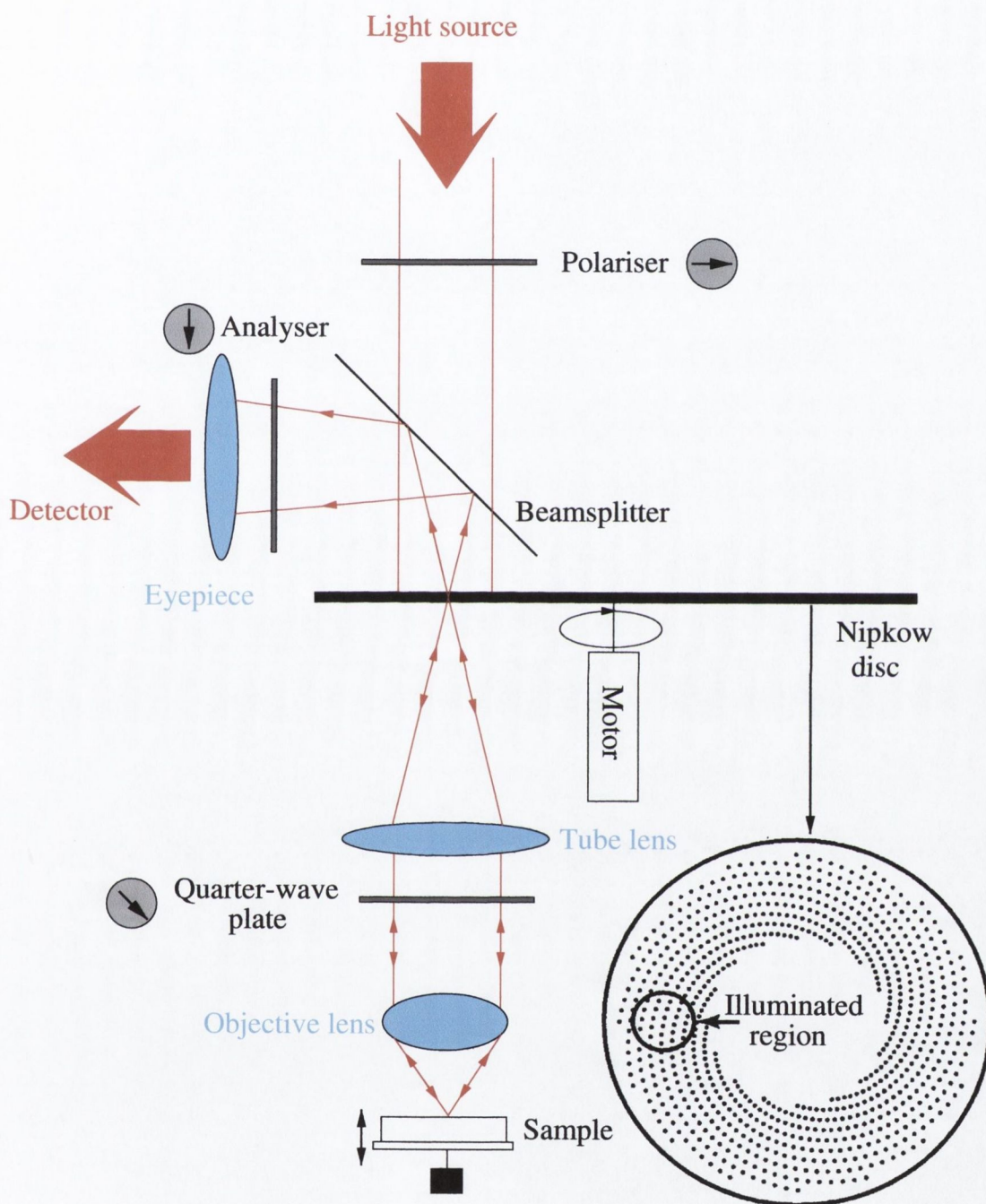
Sample

Figure 1.5:   The optical configuration of a single-sided DVM.

13

path in reverse and is imaged to a spot centred on the same pinhole from whence it originated. The size of this spot is determined by the distance of the illuminated part of the sample from the focal plane of the objective lens. If the point in the sample associated with this pinhole is far from the focal plane, then the spot may be large enough to overlap pinholes adjacent to the original pinhole. This phenomenon is called crosstalk and generally manifests itself as a loss of the contrast in recorded images. It is for this reason that the imaging is often described as being quasi-confocal. The arrangement of polarisers and a quarter-wave plate in Figure 1.5 ensure that only light which has traversed the quarter-wave plate twice (*i.e.* been reflected from the sample) is allowed to reach the eyepiece. Light which passes the Nipkow disc in reverse is directed by a beamsplitter to an eyepiece where direct-viewing of the sample is possible. For this reason, this and related systems are often called direct-view microscopes.

In this thesis, we use the term direct-view microscope (DVM) to describe any system which uses a Nipkow disc arrangement of pinholes to achieve real-time quasi-confocal imaging. For convenience, we use this terminology regardless of whether or not the image is viewed directly by the naked eye via an eyepiece.

1.5 Practical direct-view microscopes

Since the emergence of the DVM as a versatile instrument capable of real-time quasi-confocal imaging, it has found application in a diverse range of fields. For example, Boyde *et al.* have used the system extensively in brightfield or reflection mode for the imaging of low-contrast biological specimens, in particular bone and teeth [23]. Fluorescence imaging (see Chapter 3 for a discussion) of intra-cellular components has also been achieved to good effect [24]. Other important applications include the imaging of integrated circuits [22] and semiconductor device metrology. More recently, DVMs which use a programmable aperture mask rather than a Nipkow disc have been successfully implemented (see Chapter 4). Exotic DVMs which operate in multiphoton fluorescence mode have also been reported by several workers (see Chapter 3 for a

discussion).

The primary problem encountered by workers using DVM systems is the extremely low light throughput of the Nipkow disc. In order to reduce crosstalk between neighbouring pinholes in the disc, they are kept as far apart as possible and thus the fraction of the area of the disc covered by pinholes is small. For incoherent source DVMs the important factor which determines the level of crosstalk has been shown to be the ratio between the pinhole spacing and the pinhole diameter, the mark-space ratio m_s. Early DVMs used arrays of pinholes with $m_s = 10$ however more recently it has been shown [25] that mark-space ratios as low as $m_s = 5$ can be used without compromising resolution. Nevertheless, such a mark-space ratio places the light throughput of the disc at $\sim 4\%$ and thus the instrument is still very wasteful of illumination light.

Various attempts have been made to improve throughput, for example, Baer *et al.* [26] have employed slits in the Nipkow disc in an attempt to improve throughput while inevitably losing some resolution. Yin *et al.* [27] have used phase masks to build a highly throughput efficient kinoform-based Nipkow disc. Wilson and co-workers [28, 29] have developed a technique which can eliminate crosstalk while maintaining a high level of throughput. The idea uses a method of aperture correlation which is discussed further in Chapter 4. In fluorescence-mode DVMs which achieve confocal operation via the process of two- or multi-photon absorption fluorescence, recent developments have shown great promise in reducing crosstalk related problems entirely by ensuring that adjacent confocal channels are switched on at different times. This idea is discussed further in the introductory section of Chapter 3.

While the properties of DVM systems employing incoherent light sources are quite well understood, DVMs which use coherent illumination have been neglected to a large extent. This has been because of perceived problems related to speckle effects and coherent crosstalk which causes enhanced sidelobes in the depth response. However, if the pinhole array dimensions are carefully chosen, these effects can be negated to an extent and the benefits of high brightness, highly directional and spectrally narrow coherent sources can be reaped.

The main focus of this thesis will be to examine various effects of source coherence with emphasis on the depth sectioning side of the imaging. We make this choice for the reason that Hewlett *et al.* have stated [30] that provided the ratio of pinhole spacing to pinhole radius is ≥ 10, lateral resolution in the brightfield DVM is independent of source coherence. In the case of fluorescence DVMs, Fewer *et al.* [31] have predicted that coherent source F-DVMs have similar lateral resolution characteristics to incoherent source F-DVMs provided pinhole spacings of ≥ 20 optical units (in the object plane) are employed. Thus, if the problems related to the depth sectioning side of coherent source imaging can be addressed, the benefits of both brightfield and fluorescence-mode coherent source DVMs can be fully accrued.

1.6   Thesis layout

In Chapter 2 we present a well-accepted theory which can be used to accurately predict the imaging properties of a multitude of imaging instruments. We demonstrate how such a theory has been applied to the direct-view microscope. The equations resulting from this analysis are commonly used in studies of all types of confocal microscopes and will be used extensively in this thesis.

Chapter 3 addresses the depth sectioning properties of fluorescence mode DVMs (F-DVMs) employing both coherent and incoherent light sources. Predictions of the theory of Chapter 2, where possible, are validated by experiment.

Chapter 4 presents our design for a DVM which uses a programmable aperture mask (using liquid crystal technology), rather than the usual Nipkow disc, to achieve confocal operation. The system uses a coherent light source and effects of this source coherence and limitations of the system are discussed.

In Chapter 5, we perform a theoretical analysis of coherent source DVMs and attempt to broadly describe the behaviour which can be expected. We present some equations which will find use in the study of coherent source DVMs. We also show how the use a asymmetric arrays of pinholes can improve the imaging considerably, and attempt to

deduce a minimal pinhole spacing condition for pinholes in the array similar to that presented above for incoherent source DVMs.

In Chapter 6 we present a novel design for a confocal endoscope which is based upon variable-focal-length microlens array technology and perform some preliminary examinations of the feasibility of such a design. Finally, in Chapter 7, we present our conclusions and suggest future avenues of research which could be explored.

Chapter 2

Basic theory and equations

This chapter introduces a well-accepted method [11] by which scalar diffraction theory can be used to describe the imaging behaviour of an optical system. The Huygens-Fresnel principle is used, together with Kirchoff's boundary conditions. This, along with the thin lens approximation, allows the optical field in an observation plane of an optical system to be expressed in terms of the field in the object plane and a function describing the effects of the optical elements. Application of this technique to the direct-view microscope will allow us to derive expressions for both the point object response (lateral resolution) and the planar object response (depth resolution) which are valid for systems of low angular aperture. Thus, the imaging properties of various DVM configurations can be described in mathematical form [30, 31, 32, 33]. We experimentally verify some of the predications of this theoretical approach in Chapters 3 (fluorescence DVM) and 4 (coherent source brightfield DVM). The chapter should serve as a reference point for the reader interested in the basic theory behind all equations presented in this thesis.

2.1 Propagation of an optical wavefront through space

A complete description of an electromagnetic field requires the expression of the magnitudes of all the field components along with their directions, or polarisations, as functions of position and time. The inherent coupling between the electric and magnetic components of the field must be considered as well as the boundary conditions when the fields cross any discontinuities, as implied by Maxwell's equations. Fortunately, in many cases of practical interest it is sufficient to consider a scalar representation of a single component of the electric field which obeys a scalar wave equation [1].

In what follows, we apply scalar diffraction theory to the problem of image formation in a low NA imaging system. In order to formulate an expression for the propagation of light through a medium, we first draw on an idea of Christian Huygens who, in 1678, proposed the following: if each point on an optical wavefront is considered to be a secondary source of spherical wavelets, then the wavefront at any later time can be represented by the envelope of these secondary wavelets. One hundred and forty years later, Augustin Jean Fresnel improved on this hypothesis by supplementing Thomas Young's principle of interference to Huygens' idea: the secondary wavelets were allowed to interfere. The work was further added to by Gustav Kirchoff who placed the idea on solid mathematical ground by showing that it was equivalent to an approximate form of Helmholtz's integral theorem [34]. Following the 'Huygens-Fresnel principle', the optical field, U_0, in a plane described by points (x_0, y_0) can be related to the field, U_1, in a downstream plane of observation (x_1, y_1) as:

$$U_1(x_1, y_1) = \iint_{-\infty}^{\infty} \frac{\exp(jkr)}{j\lambda z} U_0(x_0, y_0) dx_0 dy_0, \tag{2.1}$$

where r is the distance between points (x_0, y_0) and (x_1, y_1); z is the axial distance between the two planes containing these points. Assuming monochromatic illumination, λ is the free space wavelength of the light and $k = \frac{2\pi}{\lambda}$ is the propagation constant of

the wavefront. Here, and throughout this thesis, $j = \sqrt{-1}$.

We shall employ the Fresnel approximation to the above integral which is essentially a paraxial approximation which is valid so long as the field amplitudes are appreciable only in the vicinity of the optic axis and are small compared to the distance between the two planes of interest. Thus, Equation (2.1) can be written:

$$U_1(x_1, y_1) = \frac{\exp(jkz)}{j\lambda z} \iint_{-\infty}^{\infty} U_0(x_0, y_0) \exp\left(\frac{jk}{2z}[(x_1 - x_0)^2 + (y_1 - y_0)^2]\right) dx_0 dy_0.$$

(2.2)

Equation(2.2) describes the evolution of an optical wavefront as it propagates through space.

2.2 Propagation of an optical wavefront through a lens

We consider a lens to have two effects on an incident wavefront:

- (1) A restriction is imposed on the lateral size of the wavefront due to the finite size of the lens pupil (vignetting).

- (2) Assuming the lens to have a different refractive index from the surrounding medium, a phase transformation is applied to an incident wavefront. For a convex spherical lens, the amount of phase transformation varies across the wavefront, being dependent on the thickness of lens material traversed.

In view of (1), above, we define a window function, $\mathrm{Circ}(\epsilon, \eta)$, which, for a lens with a circular pupil of radius a, has the following property:

$$\mathrm{Circ}(\epsilon, \eta) = \begin{cases} 1, & \sqrt{\epsilon^2 + \eta^2} \leq a \\ 0, & \text{otherwise,} \end{cases}$$

(2.3)

20

(ϵ, η) represents a point in the plane of the lens. In order to describe the phase transformation mentioned in (2) above, we use the thin lens approximation. Essentially, this assumes that the wavefront suffers no lateral translation due to refraction at the curved lens surface. For a spherical lens, the phase transformation, t, suffered by any part of the wavefront depends on the transverse co-ordinate (ϵ, η) of the lens on which it is incident as follows [35]:

$$t(\epsilon, \eta) = \exp\left(\frac{-jk}{2f}(\epsilon^2 + \eta^2)\right),\qquad(2.4)$$

for a lens of focal length f.

2.3 The lens point spread function

We now consider the optical system shown in Figure 2.1. A radiant object, at a distance d_0 from a convex lens is transformed by the lens to form an optical disturbance in an observation plane at a distance d_1 from the opposite side of the lens. By repeated application of Equations (2.2), (2.3), & (2.4), we attempt to describe the field $V_1(x_1, y_1)$ in an observation plane, which results from a perfect point source of light being present at (x_0, y_0) in the object plane.

Using Equation (2.2), and assuming a perfect point source of monochromatic radiation at (x_0, y_0) in the object plane, it is possible to write the field amplitude, U_l, directly in front of the lens as:

$$U_l(\epsilon, \eta) = \frac{1}{j\lambda d_0} \exp\left(\frac{jk}{2d_0}[(\epsilon - x_0)^2 + (\eta - y_0)^2]\right).\qquad(2.5)$$

Application of Equations (2.3) & (2.4), followed by Equation (2.2), allows us to write
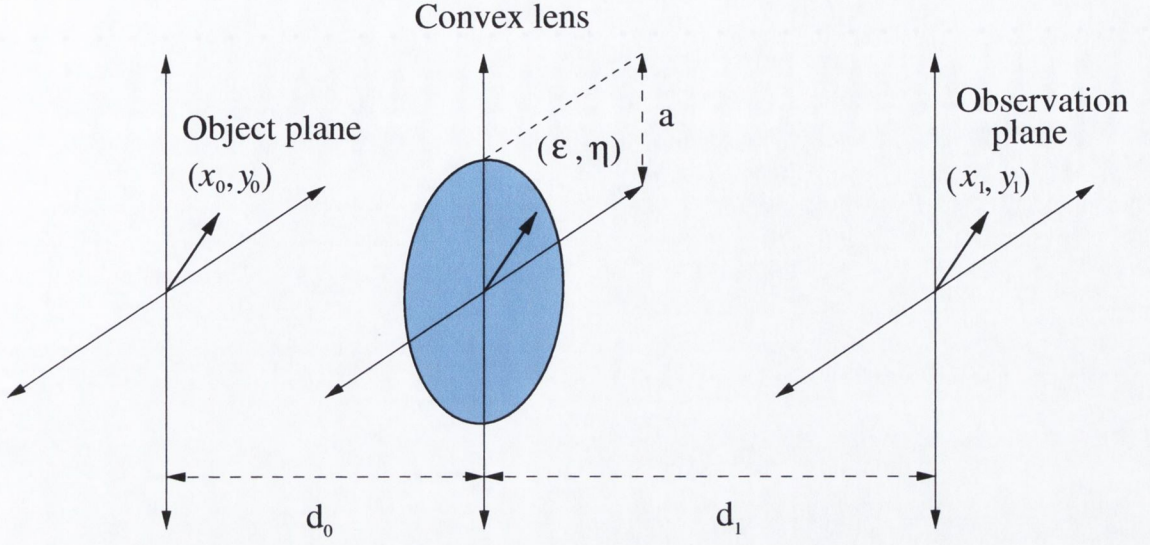
Figure 2.1:   The geometry of a simple optical system.

the field amplitude, $V_1(x_1, y_1)$ in the observation plane as:

$$V_1(x_1, y_1) = \frac{1}{\lambda^2 d_0 d_1} \exp\left(\frac{jk}{2d_1}(x_1^2 + y_1^2)\right) \exp\left(\frac{jk}{2d_0}(x_0^2 + y_0^2)\right) \iint_{-\infty}^{\infty} \mathrm{Circ}(\epsilon, \eta)$$

$$\times \exp\left(\frac{jk}{2}\left(\frac{1}{d_0} + \frac{1}{d_1} - \frac{1}{f}\right)(\epsilon^2 + \eta^2)\right)$$

$$\times \exp\left(-jk\left[\left(\frac{x_0}{d_0} + \frac{x_1}{d_1}\right)\epsilon + \left(\frac{y_0}{d_0} + \frac{y_1}{d_1}\right)\eta\right]\right) d\epsilon \, d\eta. \quad (2.6)$$

By introducing the magnification, M, of the system via:

$$M = \frac{d_1}{d_0}, \quad (2.7)$$

and, noting that in most cases of practical interest we can drop the premultiplying phase factors, along with any constant factors outside the integral [35], we may write

22

$V_1(x_1, y_1)$ as:

$$V_1(x_1, y_1) = \iint_{-\infty}^{\infty} \mathrm{Circ}(\epsilon, \eta) \exp\left(\frac{jk}{2}\left(\frac{1}{d_0} + \frac{1}{d_1} - \frac{1}{f}\right)(\epsilon^2 + \eta^2)\right)$$
$$\times \exp\left(-\frac{jk}{d_0}\left[\left(x_0 + \frac{x_1}{M}\right)\epsilon + \left(y_0 + \frac{y_1}{M}\right)\eta\right]\right) d\epsilon d\eta. \tag{2.8}$$

The optical disturbance denoted by $V_1(x_1, y_1)$ represents the field amplitude in the observation plane which results from a **perfect point source** being present at (x_0, y_0) in the object plane. It is straightforward to show that the field amplitude $U_1(x_1, y_1)$ in the observation plane due to **any object field amplitude**, $U_0(x_0, y_0)$, can now be expressed as the following superposition integral[1]:

$$U_1(x_1, y_1) = \iint_{-\infty}^{\infty} V_1(x_1, y_1; x_0, y_0) U_0(x_0, y_0) dx_0 dy_0, \tag{2.9}$$

where the notation $V_1(x_1, y_1; x_0, y_0)$ should be understood to denote the field amplitude at a point (x_1, y_1) in the observation plane which results from a perfect point source being present at (x_0, y_0) in the object plane.

We can simplify our notation somewhat by defining a function $h(x, y)$ such that:

$$h(x, y) = \iint_{-\infty}^{\infty} \mathrm{Circ}(\epsilon, \eta) \exp\left(\frac{jk}{2}\left(\frac{1}{d_0} + \frac{1}{d_1} - \frac{1}{f}\right)(\epsilon^2 + \eta^2)\right)$$
$$\times \exp\left(-\frac{jk}{d_0}[x\epsilon + y\eta]\right) d\epsilon d\eta. \tag{2.10}$$

We now recast Equation (2.9) in terms of h in the following form:

$$U_1(x_1, y_1) = \iint_{-\infty}^{\infty} h\left(x_0 + \frac{x_1}{M}, y_0 + \frac{y_1}{M}\right) U_0(x_0, y_0) dx_0 dy_0. \tag{2.11}$$

$h(x, y)$ is the point spread function of the lens and describes the fidelity with which the image of a point object can be reproduced and thus represents the resolution of the

---

[1]This is possible because the imaging process is linear and can be represented, point-by-point, by a space-invariant transfer function [35].

lens. Equation (2.10) has been widely used in the theoretical study of imaging systems including confocal microscopes [11, 13].

Looking at Equations (2.10) & (2.11), we can make an interesting observation: from elementary geometrical optics we can relate the Gaussian image plane of a thin lens to the object plane via:

$$\frac{1}{f} = \frac{1}{d_0} + \frac{1}{d_1},$$ (2.12)

It is interesting to note that if we choose d_1, for a given object distance d_0, so that Equation (2.12) is satisfied, the image plane, as predicted by Gaussian optics, and the observation plane will coincide. In this case, $U_1(x_1, y_1)$, as given by Equation (2.11), represents the 'best-focused' image of the object. When the Gaussian lens equation is not satisfied we describe the system to be defocused.

2.4 Normalised optical co-ordinates

It is possible to collect all explicit occurrences of parameters of the optical system from Equation (2.10): the distances d_0 and d_1, the focal length f, the lens radius a and the light wavelength λ, and regroup these parameters into a single versatile quantity. We achieve this by transforming all lateral and axial co-ordinates to form a new co-ordinate system. The **normalised optical co-ordinate system** [1] is constructed as follows: the lateral lens co-ordinates are normalised to unity at the edge of the lens so that (ϵ, η) becomes $(\epsilon/a, \eta/a)$. From the 2nd exponential term in Equation (2.10) we next extract all occurrences of the optical system parameters so that transverse co-ordinates are now expressed in the form:

$$t, w = \frac{2\pi a x, y}{\lambda d_0}.$$ (2.13)

Or, in the paraxial approximation:

$$t, w = \frac{2\pi x, y}{\lambda} n \sin \alpha. \tag{2.14}$$

Where $n \sin \alpha$ is the NA [2] of the lens and we have introduced n to allow for the use of the use of an immersion medium[1] between the objective lens and sample. Moving, now to the first exponential term of Equation (2.10), we again group the system parameters to form the axial normalised optical co-ordinate, u, as:

$$u = \frac{2\pi a^2}{\lambda} \left(\frac{1}{f} - \frac{1}{d_0} - \frac{1}{d_1} \right), \tag{2.15}$$

which reduces to [11]:

$$u = \frac{8\pi n}{\lambda} z \sin^2 \left(\frac{\alpha}{2} \right), \tag{2.16}$$

provided the real defocus, $z << d_{0,1}$. We can now recast Equation (2.10) in the form:

$$h(u, t, w) = \iint_{-\infty}^{\infty} P(u, \epsilon, \eta) \exp(-j[t\epsilon + w\eta]) d\epsilon d\eta, \tag{2.17}$$

with the complex lens Pupil function, $P(u, \epsilon, \eta)$, defined by:

$$P(u, \epsilon, \eta) = \begin{cases} \exp\left(-\frac{1}{2}ju[\epsilon^2 + \eta^2]\right) = \exp(-\frac{1}{2}ju\rho^2), & |\rho| \leq 1 \\ 0, & \text{otherwise.} \end{cases} \tag{2.18}$$

In the case of circular lens pupils the lens point spread function can now be expressed as a Hankel transform [1, 11, 35]:

$$h(u, t, w) = h(u, \sqrt{t^2 + w^2}) = \int_0^1 P(u, \rho) J_0(\rho\sqrt{t^2 + w^2})\rho d\rho, \tag{2.19}$$

---

[1]Such immersion media are typically employed in order to increase the lateral resolving power of the lens, having the further advantage of reducing refraction-induced aberration in the imaging. This can be achieved by matching the refractive indices of the immersion medium and the sample.

where J_0 is a zero-order Bessel function. Applying the co-ordinate transformations to Equation (2.11), allows us to write:

$$U_1(t_1, w_1) = \iint_{-\infty}^{\infty} h\left(u, t_0 + \frac{t_1}{M}, w_0 + \frac{w_1}{M}\right) U_0(t_0, w_0) dt_0 dw_0, \qquad (2.20)$$

with all variables expressed in the normalised optical co-ordinate system as defined by Equations (2.14) & (2.16). Due to the growing complexity of our equations, it is prudent to express Equations (2.20) & (2.17) using vector notation via the following definitions:

$$(t, w) = \underline{t}, \quad (t_0, w_0) = \underline{t}_0, \quad (t_1, w_1) = \underline{t}_1, \quad (\epsilon, \eta) = \underline{\epsilon}. \qquad (2.21)$$

We also drop the explicit occurrences of limits in integrations to be performed over the infinite plane: the absence of limits in any integrals hereafter will indicate the fact the in integration is to be performed from $-\infty \rightarrow \infty$. We may now write for Equation (2.17):

$$h(u, \underline{t}) = \int P(u, \underline{\epsilon}) \exp(-j\underline{t}.\underline{\epsilon}) \mathrm{d}^2\underline{\epsilon}, \qquad (2.22)$$

and for Equation (2.20):

$$U_1(\underline{t}_1) = \int h\left(u, \underline{t}_0 + \frac{\underline{t}_1}{M}\right) U_0(\underline{t}_0) \mathrm{d}^2\underline{t}_0. \qquad (2.23)$$

Because, in many practical situations, we will be dealing with detectors of light **intensity** rather than its amplitude, we require the intensity analogue of Equation (2.23). This is dependent on the nature of the object under inspection and the nature of the illumination source.

For example, an object illuminated with coherent light gives rise to a coherent wavefront $U_0(\underline{t}_0)$, which interacts with the lens in a coherent manner (*i.e.* via field **ampli-**

tudes) and so the intensity, I_1 in the observation plane must be written:

$$I_1(\underline{t}_1) = \left| \int h\left(u, \underline{t}_0 + \frac{\underline{t}_1}{M}\right) U_0(\underline{t}_0) \mathrm{d}^2\underline{t}_0 \right|^2. \tag{2.24}$$

In the case of incoherent illumination, the object gives rise to an incoherent wavefront $I_0 = |U_0|^2$, which interacts with the lens in an incoherent manner (*i.e.* via field **intensities**) and so the intensity, I_1 in the observation plane must be written:

$$I_1(\underline{t}_1) = \int \left| h\left(u, \underline{t}_0 + \frac{\underline{t}_1}{M}\right) \right|^2 |U_0(\underline{t}_0)|^2 \mathrm{d}^2\underline{t}_0. \tag{2.25}$$

2.5 Application of theory to a confocal microscope

We now set out to show how Equation (2.23) can be applied to a practical optical instrument, in our case, the direct-view microscope. Essentially, we assume a stationary object which is illuminated via an array of source apertures described by S. The light which is reflected/fluoresced by the object is directed towards a detector array D where an intensity image is recorded. The source and detector arrays are scanned in synchronism in order to image the desired field of view on the object. Following the approach of Wilson and Hewlett [33] we now derive expressions for the intensity image in the detector plane of such a microscope which employs an incoherent source.

2.5.1 Direct-view microscope

Figure 2.2 shows the unfolded light path of a reflection-mode direct-view microscope: in this case one lens serves as both an objective and collector lens. Furthermore, both lenses have the same defocus relative to the object. Continuing our vector notation, we define source and detector arrays $S(\underline{t}_1)$ & $D(\underline{t}_2)$ which are scanned synchronously relative to a stationary object, according to a scan co-ordinate $\underline{t}_s$ which is referenced to the object plane. The source array configuration is imaged via a lens with pupil function P_1 onto an object with amplitude reflectance given by $\tau(\underline{t}_0)$. The resulting
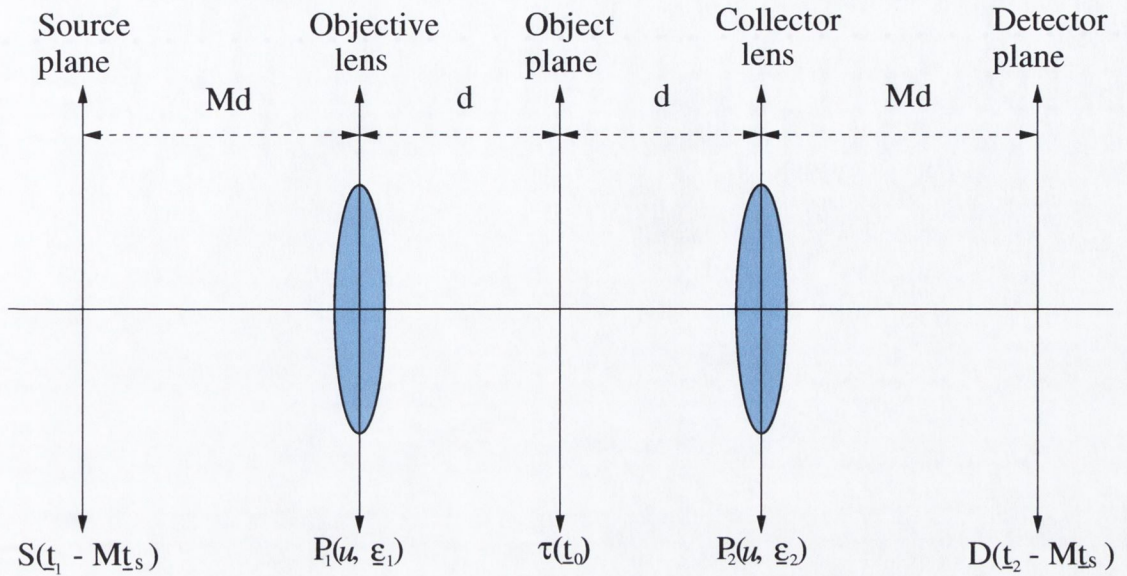
Figure 2.2: Geometry of the direct-view microscope.

disturbance on the object is imaged by a second lens with pupil function P_2 onto the detector array.

Brightfield imaging

Assuming an incoherent light source, the intensity, I_0, in the object plane of a brightfield DVM can be expressed via Equation (2.23) as:

$$I_0(u, \underline{t}_0) = \int S(\underline{t}_1 - M\underline{t}_s) \left| \tau(\underline{t}_0) h_1 \left(u, \underline{t}_0 + \frac{\underline{t}_1}{M} \right) \right|^2 d^2\underline{t}_1 \qquad (2.26)$$

With h_1 related to the pupil function P_1 via Equation (2.22). Assuming a detector array which responds to light intensity, a further application of Equation (2.23) allows us to express the intensity at $\underline{t}_2$ in the detector plane for a given scan position $\underline{t}_s$ as:

$$I_2(u, \underline{t}_2, \underline{t}_s) = \int S(\underline{t}_1 - M\underline{t}_s) D(\underline{t}_2 - M\underline{t}_s)$$

$$\times \left| \int \tau(\underline{t}_0) h_1 \left(u, \underline{t}_0 + \frac{\underline{t}_1}{M} \right) h_2 \left(u, \underline{t}_0 + \frac{\underline{t}_2}{M} \right) d^2\underline{t}_0 \right|^2 d^2\underline{t}_1. \qquad (2.27)$$

28

Now, integrating across all possible scan positions $\underline{\mathbf{t}}_s$ gives the final intensity image formed by the instrument.

Fluorescence imaging

In a completely analogous way, the intensity image formed by a fluorescence DVM employing an incoherent light source can be written:

$$I_2(u, \underline{\mathbf{t}}_2) = \iiint S(\underline{\mathbf{t}}_1 - M\underline{\mathbf{t}}_s) D(\underline{\mathbf{t}}_2 - M\underline{\mathbf{t}}_s)$$

$$\times \left| h_1\left(u, \underline{\mathbf{t}}_0 + \frac{\underline{\mathbf{t}}_1}{M}\right) h_2\left(\frac{u}{\beta}, \frac{\underline{\mathbf{t}}_0 + \frac{\underline{\mathbf{t}}_2}{M}}{\beta}\right) \right|^2 f(\underline{\mathbf{t}}_0) \mathrm{d}^2\underline{\mathbf{t}}_0 \mathrm{d}^2\underline{\mathbf{t}}_1 \mathrm{d}^2\underline{\mathbf{t}}_s. \tag{2.28}$$

The factor $\beta = \lambda_f/\lambda_e$ accounts for the fact that the fluorescence wavelength, λ_f differs from the excitation wavelength λ_e. This results in a change in the normalised optical co-ordinate system between the objective and collector lenses: u becomes u/β etc. We have defined f as the fluorescence generation function of the object. Following Cox *et al.* [36], we assume that the generated fluorescence is proportional to the **intensity** of the incident light and thus is convolved with the effective **intensity** point spread function.

2.6 Comparison of conventional and confocal microscopes

We now briefly examine the imaging properties of basic incoherent source brightfield DVM systems by looking at some of the limiting cases of Equation (2.27). Two particular cases serve illustrative purposes well: A single aperture DVM employing:

A. An infinitesimal source aperture and large-area detector aperture (conventional microscope).

B. An infinitesimal source and infinitesimal detector aperture (confocal microscope). We choose to refer to **A** above as a **Type A** DVM; **B** is referred to as a **Type B** DVM.

2.6.1 The point object response (lateral resolution)

The point object response of a microscope is an order of merit which describes its lateral resolution. We now compare Type A and Type B DVMs, as defined above, from a lateral resolution point of view. The point object is represented mathematically by a Dirac delta function , $\delta(x)$ [1] (see also Appendix A). In Equation (2.27) we make the following substitution:

$$\tau(\underline{\mathbf{t}}_0) = \delta(\underline{\mathbf{t}}_0), \tag{2.29}$$

so that we now have:

$$I_{\text{POINT}}(u, \underline{\mathbf{t}}_2) = \iint S(\underline{\mathbf{t}}_1 - M\underline{\mathbf{t}}_s) \left| h_1\left(u, \frac{\underline{\mathbf{t}}_1}{M}\right) h_2\left(u, \frac{\underline{\mathbf{t}}_2}{M}\right) \right|^2 D(\underline{\mathbf{t}}_2 - M\underline{\mathbf{t}}_s) \mathrm{d}^2\underline{\mathbf{t}}_1 \mathrm{d}^2\underline{\mathbf{t}}_s. \tag{2.30}$$

'

- In the case of a Type A DVM ($S(\underline{\mathbf{t}}) = \delta(\underline{\mathbf{t}})$, $D(\underline{\mathbf{t}}) = 1$), the in-focus point object response can be expressed [11]:

$$I_{\text{POINT}_A}(0, \underline{\mathbf{t}}_s) = |h_1(0, \underline{\mathbf{t}}_s)|^2. \tag{2.31}$$

- While, for a Type B DVM ($S, D(\underline{\mathbf{t}}) = \delta(\underline{\mathbf{t}})$), the in-focus point object response is expressed [11]:

$$I_{\text{POINT}_B}(0, \underline{\mathbf{t}}_s) = |h_1(0, \underline{\mathbf{t}}_s)|^2 |h_2(0, \underline{\mathbf{t}}_s)|^2. \tag{2.32}$$

Assuming circular lens pupils and identical lenses, we may write [1]:

$$h_{1,2}(0, \underline{\mathbf{t}}_s) = h(0, |\underline{\mathbf{t}}_s|) = \frac{2J_1(|\underline{\mathbf{t}}_s|)}{|\underline{\mathbf{t}}_s|}, \tag{2.33}$$

where J_1 is a 1st order Bessel function of the first kind. Figure 2.3 compares point object responses for Type A and Type B DVMs. An improvement of $\sim 29\%$ in lateral
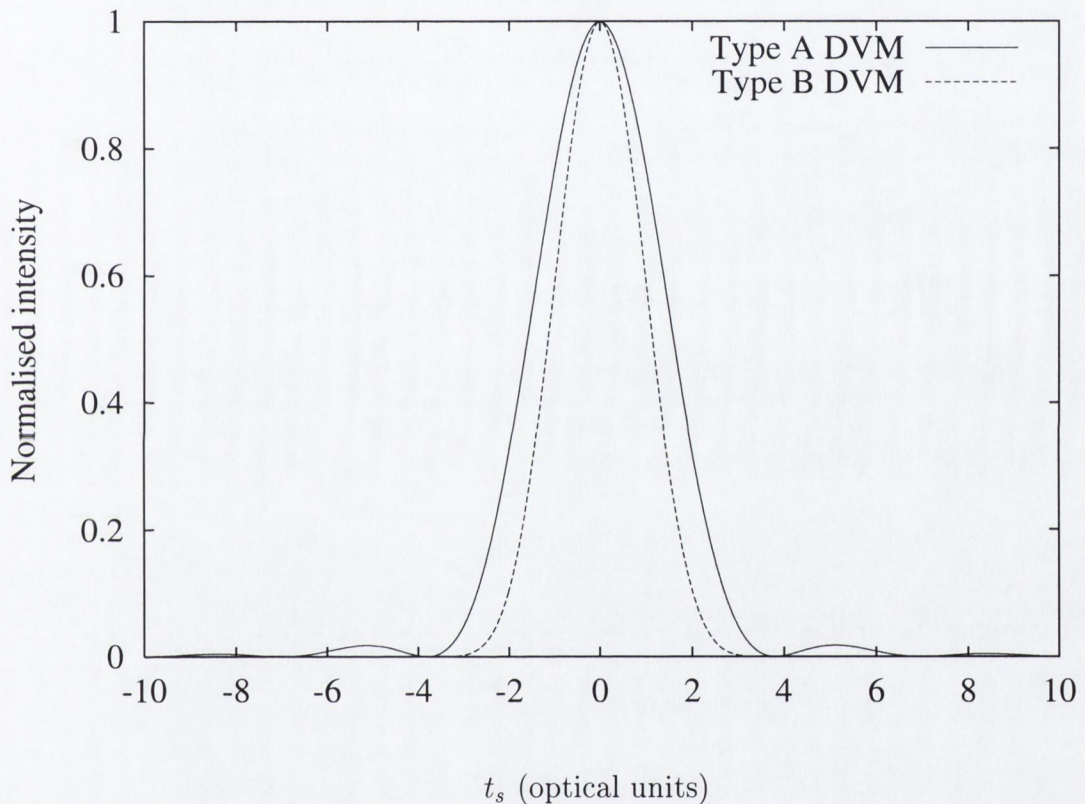
Figure 2.3: The point object responses of Type A & B DVMs. The lateral resolution enhancement offered by the Type B DVM (confocal microscope) is clear.

resolution (measured at half the peak intensity) can be seen for the Type B DVM over the Type A DVM. Evidently, the use a point detecting aperture gives rise to superior lateral resolution. We also notice from the figure that the sidelobes of the point response are very much reduced in the case of the Type B DVM, predicting fewer artefacts in recorded images. The situation is analogous to that of the CSOM

31

which we discussed in Chapter 1 : the introduction of a point detector gives both the objective and collector lenses an equal role in the imaging. The effective point spread functions of both lenses are multiplied, and a sharpening of the image results.

In practical DVM systems, arrays of finite sized apertures are typically used with the result that in general, the imaging will fall between the two extremes outlined above. The exact form of the point object response of DVM systems has been dealt with comprehensively, from a theoretical point of view, in the literature, (see for example Hewlett *et al.* [30]) and shown to be heavily dependent both on the aperture array configuration and the source coherence. With the dependence on source coherence breaking down for pinhole spacing to radius ratios of ≥ 10. Theoretical predictions of lateral resolution enhancement have been verified by experiment [37, 38, 39] in single aperture CSOM/DVM systems. In the course of this thesis, for reasons outlined in Chapter 1, we choose to focus on the more striking benefit offered by the confocal microscope:– namely the depth resolution enhancements offered.

2.6.2 The planar object response (depth resolution)

Reverting again to Equation (2.27), in an attempt to ascertain the depth resolution of simple DVMs, we now examine the intensity responses of the Type A and Type B DVMs as a planar object is scanned through the focal plane of the objective lens: the so-called depth response. We specify a planar object mathematically, simply by describing the object's amplitude reflectance to be:

$$\tau(\underline{t}_0) = 1. \tag{2.34}$$

We then integrate Equation (2.27) over the detector plane $\underline{t}_2$, which allows us to write the total intensity in the detector plane as a function of defocus alone:

$$I_{\text{PLANE}}(u) = \iiint S(\underline{t}_1 - M\underline{t}_s) \left| \int h_1 \left(u, \underline{t}_0 + \frac{\underline{t}_1}{M} \right) h_2 \left(u, \underline{t}_0 + \frac{\underline{t}_2}{M} \right) d^2\underline{t}_0 \right|^2$$
$$D(\underline{t}_2 - M\underline{t}_s) d^2\underline{t}_1 d^2\underline{t}_s d^2\underline{t}_2. \tag{2.35}$$

Assuming identical objective and condenser lenses we may write:

- In the case of a Type A DVM ($S(\underline{t}) = \delta(\underline{t})$, $D(\underline{t}) = 1$) [11]:

$$I_{\text{PLANE}_A}(u) = \int |h \otimes h(u, \underline{t}_2/M)|^2 \, d^2\underline{t}_2 = \text{constant}. \qquad (2.36)$$

where $\otimes$ represents the convolution operation [35].

- While, in the case of a Type B DVM (S, $D(\underline{t}) = \delta(\underline{t})$) [11]:

$$I_{\text{PLANE}_B}(u) = |h \otimes h(u, 0)|^2 = |h(2u, 0)|^2 = \left(\frac{\sin(u/2)}{u/2} \right)^2. \qquad (2.37)$$

We have plotted the planar object depth responses of both cases in Figure 2.4. The difference between the two curves demonstrates the main advantage of confocal microscopes over their more conventional counterparts, i.e. the introduction of preferential depth selection into the imaging. Again, the exact form of the planar response of a DVM is heavily dependent on the aperture array dimensions and the degree of source coherence as described by several authors [7, 25, 30, 32, 40]. In this thesis we further add to this work, with a particular emphasis on the effects of source coherence. In order to complete such a study, we require equations which describe the depth response characteristics of multi-aperture DVMs employing finite apertures in a variety of imaging environments.

2.7 The optical transfer function

It is convenient for our purposes to examine the depth sectioning properties of the DVM via its optical transfer function: a function describing the spatial frequency response of the instrument. We thus move from describing the imaging in the space domain to a description of the imaging in the Fourier spatial frequency domain.
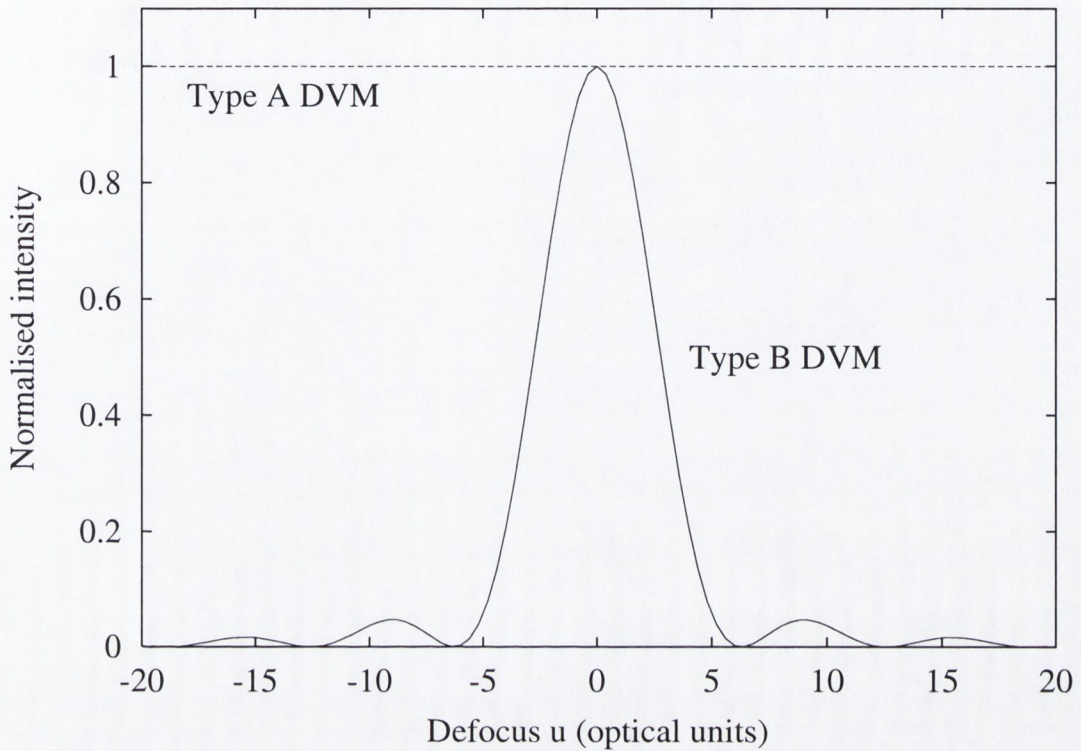
Figure 2.4: The planar object responses of Type A & B DVMs. Note that in the case of the Type B DVM (confocal microscope) light emanating from objects close to the focal plane ($u = 0$) is more likely to reach the detector.

2.7.1 Brightfield DVM

As a first step, we introduce the spatial frequency spectrum $T(\underline{\mathbf{m}})$ of the object amplitude reflectance via:

$$T(\underline{\mathbf{m}}) = \int \tau(\underline{\mathbf{t}}_0) \exp(-j\underline{\mathbf{m}}.\underline{\mathbf{t}}_0) \mathrm{d}^2\underline{\mathbf{t}}_0. \tag{2.38}$$

We retain our use of the normalised optical co-ordinate system for spatial frequencies, so that the normalised spatial frequency $\underline{\mathbf{m}}$ is related to the real spatial frequency $\underline{\mathbf{m}}'$

via:

$$\underline{\mathbf{m}} = \frac{\mathbf{m}'\lambda}{n \sin \alpha}. \tag{2.39}$$

By substitution of Equation (2.38) into Equation (2.27), we can arrive at [30]:

$$I(u, \underline{\mathbf{t}}_2) = \iint C(u, \underline{\mathbf{m}}; \underline{\mathbf{p}}) T(\underline{\mathbf{m}}) T^*(\underline{\mathbf{p}}) \exp\left(\frac{-j(\underline{\mathbf{m}} - \underline{\mathbf{p}}).\underline{\mathbf{t}}_2}{M}\right) \mathrm{d}^2\underline{\mathbf{m}}\mathrm{d}^2\underline{\mathbf{p}}, \tag{2.40}$$

with $C(u, \underline{\mathbf{m}}; \underline{\mathbf{p}})$ given by:

$$C(u, \underline{\mathbf{m}}; \underline{\mathbf{p}}) = \iint F_{S\otimes\overline{D}}\left(\frac{\underline{\boldsymbol{\epsilon}} - \underline{\boldsymbol{\epsilon}}'}{M}\right) P_1(u, \underline{\boldsymbol{\epsilon}}) P_1^*(u, \underline{\boldsymbol{\epsilon}}') P_2(u, \underline{\mathbf{m}} - \underline{\boldsymbol{\epsilon}}) P_2^*(u, \underline{\mathbf{p}} - \underline{\boldsymbol{\epsilon}}') \mathrm{d}^2\underline{\boldsymbol{\epsilon}}\mathrm{d}^2\underline{\boldsymbol{\epsilon}}'. \tag{2.41}$$

$\underline{\mathbf{p}}$ represents an additional normalised spatial frequency and $F_{S,D}$ is given by the Fourier transform relationship:

$$F_{S,D}(\underline{\boldsymbol{\epsilon}}) = \int S, D(\underline{\mathbf{t}}) \exp(-j\underline{\boldsymbol{\epsilon}}.\underline{\mathbf{t}}) \mathrm{d}^2\underline{\mathbf{t}}. \tag{2.42}$$

In the case of a planar object, $\tau(\underline{\mathbf{t}}_0) = 1$ and so $T(\underline{\mathbf{m}}) = \delta(\underline{\mathbf{m}})$; $T^*(\underline{\mathbf{p}}) = \delta(\underline{\mathbf{p}})$. Equation (2.40) becomes a function of defocus alone and reduces to:

$$I_{\mathrm{PLANE}}(u) = C(u, 0; 0). \tag{2.43}$$

We thus have a method [30] by which the planar response can be derived from the optical transfer function.

2.7.2 Fluorescence DVM

In order to arrive at an expression for the transfer function of a fluorescence DVM, we follow a similar procedure to that outlined above: we first define the spatial frequency

spectrum, $\underline{F}(\underline{m})$ of the fluorescence generation function $f(\underline{t}_0)$:

$$\underline{F}(\underline{m}) = \int f(\underline{t}_0) \exp(-j\underline{m}.\underline{t}_0) d^2\underline{t}_0. \tag{2.44}$$

Equation (2.28) may now be expressed in the form:

$$I(u, \underline{t}_2) = \iint C(u, \underline{m}) \underline{F}(\underline{m}) \exp\left(\frac{-j\underline{m}.\underline{t}_2}{M}\right) d^2\underline{m}, \tag{2.45}$$

with $C(u, \underline{m})$ given by:

$$C(u, \underline{m}) = \int g_1(u, \underline{\epsilon}) g_2\left(\frac{u}{\beta}, \beta(\underline{m} - \underline{\epsilon})\right) F_{S\otimes\overline{D}}\left(\frac{\underline{\epsilon}}{M}\right) d^2\underline{\epsilon}, \tag{2.46}$$

where the convolution function, g, is defined by:

$$g(u, \underline{\epsilon}) = P \otimes P^*(u, \underline{\epsilon}), \tag{2.47}$$

with a functional form [41]:

$$g(u, \underline{\epsilon}) = \begin{cases} \dfrac{4}{\pi u |\underline{\epsilon}|} \displaystyle\int_0^{\cos^{-1}(|\underline{\epsilon}|/2)} \sin\left[u|\underline{\epsilon}|\left(\cos\theta - \dfrac{|\underline{\epsilon}|}{2}\right)\right] \cos\theta d\theta, & |\underline{\epsilon}| \leq 2 \\[4mm] 0, & |\underline{\epsilon}| > 2. \end{cases} \tag{2.48}$$

Which, for $u = 0$, reduces to [33]:

$$g(0, \underline{\epsilon}) = \frac{2}{\pi}\left[\cos^{-1}\left(\frac{|\underline{\epsilon}|}{2}\right) - \frac{|\underline{\epsilon}|}{2}\sqrt{1 - \frac{|\underline{\epsilon}|^2}{4}}\right]. \tag{2.49}$$

As with the brightfield case, we have the relationship

$$I_{\mathrm{PLANE}}(u) = C(u, 0; 0). \tag{2.50}$$

As with the brightfield case, again we have a method [31] by which the depth response can be derived from the optical transfer function.

2.8 Direct-view microscope transfer functions

Following the procedure as outlined above, transfer functions can be derived for brightfield and fluorescence mode DVMs employing both incoherent and coherent sources along with incoherent detectors[2]. Without giving the details, we reproduce the results below. The transfer functions, thus presented, are identical to those derived by Hewlett *et al.* [30] (brightfield transfer functions) and Fewer *et al.* [31] (fluorescence transfer functions) both of whom have used them to derive expressions for the depth responses of various DVM configurations.

2.8.1 Brightfield DVM

Incoherent source

The optical transfer function of a DVM employing an incoherent source and detector is described by Equation (2.41).

---

[2]An incoherent detector is one which responds to optical field **intensity**.

Coherent source

The optical transfer function of a DVM employing an coherent source and incoherent detector can be written as [30]:

$$C(u, \underline{\mathbf{m}}; \underline{\mathbf{p}}) = \iint F_{\overline{D}}\left(\frac{\boldsymbol{\epsilon} - \boldsymbol{\epsilon}'}{M}\right) F_{S_A}\left(\frac{\boldsymbol{\epsilon}}{M}\right) F_{S_A}^*\left(\frac{\boldsymbol{\epsilon}'}{M}\right)$$
$$P_1(u, \boldsymbol{\epsilon}) P_1^*(u, \boldsymbol{\epsilon}') P_2(u, \underline{\mathbf{m}} - \boldsymbol{\epsilon}) P_2^*(u, \underline{\mathbf{p}} - \boldsymbol{\epsilon}') \mathrm{d}^2\underline{\boldsymbol{\epsilon}}\mathrm{d}^2\boldsymbol{\epsilon}'. \tag{2.51}$$

2.8.2 Fluorescence DVM

Incoherent source

The optical transfer function of a fluorescence DVM employing an incoherent source and detector is described by Equation (2.46).

Coherent source

The optical transfer function of a fluorescence DVM employing a coherent source and incoherent detector can be written as [31]:

$$C(u, \underline{\mathbf{m}}) = \iint F_{SA}\left(\frac{\boldsymbol{\epsilon}}{M}\right) F_{SA}^*\left(\frac{\boldsymbol{\epsilon} - \boldsymbol{\epsilon}'}{M}\right) F_{\overline{D}}\left(\frac{\boldsymbol{\epsilon}'}{M}\right) P_1(u, \boldsymbol{\epsilon}) P_1^*(u, \boldsymbol{\epsilon} - \boldsymbol{\epsilon}')$$
$$g_2(u/\beta, \beta(\underline{\mathbf{m}} - \boldsymbol{\epsilon}')) \mathrm{d}^2\underline{\boldsymbol{\epsilon}}\mathrm{d}^2\boldsymbol{\epsilon}', \tag{2.52}$$

with g_2 given by:

$$g_2(u, \underline{\boldsymbol{\epsilon}}) = P_2 \otimes P_2^*(u, \underline{\boldsymbol{\epsilon}}). \tag{2.53}$$

2.9 Summary

We have introduced the theory underlying the operation of a direct-view microscope. In particular we have given expressions from which the planar object response, or 'depth response', of brightfield and fluorescence DVMs can be derived via the optical

transfer function. The chapter contains the theoretical foundations underlying all of the formulae which will be used in the thesis and should serve as a useful point of reference for the reader.

Chapter 3

Fluorescence direct-view microscopy

Confocal fluorescence microscopy is a widely used tool, particularly for the inspection of dyed biological samples, where it is preferred to conventional microscopy because samples need not be physically sectioned, but can instead be 'optically' sectioned. We perform an examination of the optical sectioning properties of a direct-view microscope, operating in fluorescence mode. In particular, we contrast the optical sectioning behaviour of fluorescence-mode direct-view microscopes (F-DVMs) employing both (spatially) coherent and incoherent illumination sources by presenting both experimental and theoretical depth response curves.

Using spin-coated laser-dye films as sources of fluorescence, we find that the finite thickness of the films used gives rise to a broadening of the depth response. By employing a paraxial modification of the usual scalar diffraction theory, we show that the experimental results are in agreement with the trends of the theoretical prediction. Further theoretical analysis allows us to postulate that the use of coherent sources in F-DVMs gives similar optical sectioning performance to the corresponding incoherent source F-DVM provided aperture arrays of appropriate dimensions are used.

3.1 Introduction

Conventional fluorescence microscopy [42] generally involves the staining , with fluorescent dyes, of tissues within biological samples. Optically pumping the sample with a light source of appropriate wavelength gives rise to excited fluorescence which emanates from the tissues and allows high contrast images to be recorded. The advantage of the technique over brightfield imaging lies in the fact that the tissues themselves, which in general tend to be weakly reflecting, can be accentuated within the sample. Because certain dye molecules bind more efficiently with particular tissues, in some cases, selected tissues can be examined [42]. If the tissues are highly localised within the sample, then it may be possible to record fluorescence images with little sample preparation. However, in the more general case of a thick sample with a somewhat homogenous distribution of tissues of interest, the sample itself may need to be prepared in a special way in order to render it suitable for imaging. For example, thick biological samples are often sliced thinly before being mounted in the microscope in order to reduce the blur which would result from out-of-focus light reaching the detector. Such sample preparation unfortunately can often damage the sample and in some cases interfere with the biological processes or features under examination.

Confocal microscopes offer an improvement on this situation due to their inherent 'non-invasive' depth-sectioning ability. In fluorescence-mode confocal microscopes [13, 43], a point source of illumination light is focused by an objective lens to excite fluorophores in a fluorescent sample. The fluoresced light is imaged onto the point detector via a filter which removes the unwanted excitation light. Because of the depth sectioning ability of the confocal microscope, captured images exhibit none of the blur usually associated with fluorescence images of thick translucent dyed samples. The method also has the advantage of a highly localised excitation spot which is continuously scanned across the sample thus reducing the rate of photobleaching[1] [42] of the dye molecules. Direct-view or tandem-scanning microscopes have also been operated

---

[1]Reduction in fluorescence intensity, over time, due to degradation of fluorophores.

in fluorescence mode. Although such instruments can suffer from extremely low light levels due to the low transmissivity of the Nipkow disc/aperture array and a fluorescence generation efficiency which is always less than 100%, direct-view images have been successfully recorded [24].

In 1994, Tanaami *et al.* [44] reported a system exhibiting improved throughput over traditional DVMs which is well suited to fluorescence imaging. Illumination light is prefocused by a microlens array with microlens pitch and geometry matched to those of a Nipkow disc (see Chapter 1). Thus, the light throughput of the disc has been improved from a typical value of $\sim 4\%$ [25] to $\sim 60\%$. The system is distributed by PerkinElmer as the 'CSU 10' real-time confocal imaging system. Recently, direct-view fluorescence microscopes operating in two-photon absorption mode, again using microlens arrays to achieve a multitude of foci which are scanned across the sample, have been reported by several workers [45, 46]. Such systems can operate without the need of a Nipkow disc: the two-photon absorption process in itself provides the necessary depth sectioning [47].

Another multifocal multiphoton system which allows an even higher level of throughput than microlens array-type systems has been reported by Nielsen *et al.* [48]. The multiple foci are generated by a high efficiency beamsplitter which has the additional advantage of applying a time delay between each of the foci which is longer than the duration of the pulse. Such 'time-multiplexed multifocal multiphoton' microscopes have also been reported by Egner and Hell [49] and have the advantage of suppressing crosstalk between adjacent foci. Yet another method of improving throughput in direct-view microscopes is the use of aperture correlation [28] (see also Chapter 4): theoretically a throughput of 50% can be achieved.

With an arrangement such as Tanaami's, that of a spiral array of microlenses matched to the pinholes of a Nipkow disc, a coherent source provides better optical throughput than an extended incoherent source. This is due to the fact that plane wave (coherent) illumination of the microlens array gives rise to an array of diffraction limited spots on the surface of the Nipkow disc which could be perfectly matched to the diameters

of the pinholes in the disc. When operated in fluorescence mode such coherent source systems have the advantage that problematic interference effects associated with coherent source brightfield DVMs are negated somewhat due to the incoherent nature of the fluorescence generation process[2]. In fact, Fewer *et al.* [31] have performed a theoretical study of imaging in F-DVMs employing both coherent and incoherent sources, stating that, from an optical sectioning point of view, the instrument is independent of source coherence. In fact, as we will show this is not quite the case: the exact relationship between coherent and incoherent source depth responses is dependent on the size of the apertures in the aperture array as well as their separation. The main thrust of this chapter is an attempt to quantify the effects of source coherence on optical sectioning strength in direct-view microscopy from an experimental point of view.

There can be problems in quantifying the depth resolution of fluorescence-mode confocal microscopes in that the usual depth response to a planar object (see Chapter 1) is not easy to perform experimentally: flat, uniformly fluorescent samples of sufficiently bright fluorescence and negligible thickness are difficult to manufacture. Certain workers [50, 51] have managed to manufacture such films and successfully perform depth response measurements, however the film production process used is quite involved. Another measure of optical sectioning strength is the so-called sea response [52]: the intensity response of the instrument to a thick fluorescent object which is wider than the full width of the optical probe. A metric which approximates the usual depth response can be derived from the sea-response by calculation of the 1st derivative of the sea-response along the optical axis. This is due to the fact that the sea-response can be approximated mathematically by:

$$I_{\text{SEA}}(u) = \int I_{\text{PLANE}}(u + u')\mathrm{d}u', \qquad (3.1)$$

with the integration performed over the axial extent of the sea. We note however,

---

[2]With concomitant advantages of high brightness, high directionality, and narrow linewidth and thus efficient excitation of the fluorophore.

that because of the aberrations associated with focusing into a thick fluorescent object (discussed in Section 3.2.3), Equation (3.1) will fail considerably because the nature of the sea response requires focusing deep within a fluorescent object. Unless it is possible to calculate the full vectorial aberrated PSFs within the object [52, 53, 54, 55] (a computationally intensive undertaking), it may be more accurate to examine the depth response to a thin fluorescent film. For the purposes of our study, this is the approach we take.

The film thickness and its refractive index are incorporated into the theory describing the expected depth response. We discuss the justifications for this approach further in Section 3.2.3. Using spin-coated films of laser dye in solution as our test samples we show that using a paraxial approach [56] to take film thickness into account gives theoretical curves which follow experimental trends. Finally, we examine the effect of aperture diameter and spacing on the optical sectioning of coherent and incoherent source F-DVMs.

3.2 Theory: F-DVM optical sectioning strength

By using the appropriate optical transfer functions as described in Section 2.7 we may derive expressions for the intensity response of the F-DVM to a planar object. We first present equations describing incoherent source systems before detailing the corresponding coherent source equations. We then show how these equations can be modified to account for finite film thickness. We will be concerned solely with DVMs employing arrays of circular apertures (pinholes) throughout.

3.2.1 Incoherent source F-DVM

Following Fewer *et al.* [31], the depth response of an incoherent source F-DVM may be derived via Equations (2.46) & (2.50). As described in Section 2.8, the planar response of the instrument is given by $C(u,0)$. We now specify a finite array of N source pinholes each of intensity distribution $S_1(\underline{t}_1)$ centred at points $\underline{T}_1, \underline{T}_2, ..., \underline{T}_N$

such that the source array S can be written as:

$$S(\underline{t}_1) = \sum_{i=1}^{N} S_1(\underline{t}_1 - \mathbf{T}_i). \tag{3.2}$$

We represent the detector array by $\overline{S}$ where the over-line indicates the fact that the light is travelling in an opposing direction to that of the excitation light and so the co-ordinate system is inverted. By further specifying the source/detector Fourier transforms by:

$$F_S(\underline{\epsilon}) = \sum_{i=1}^{N} \int S_1(\underline{t} - \mathbf{T}_i) \exp(-j\underline{\epsilon}.\underline{t}) d^2\underline{t}$$

$$= \sum_{i=1}^{N} \exp(-j\underline{\epsilon}.\mathbf{T}_i) F_{S_1}(\underline{\epsilon}), \tag{3.3}$$

we may write:

$$I_{\text{PLANE}}(u) = \sum_{i=1}^{N} \sum_{k=1}^{N} \int g_1(u,\underline{\epsilon}) g_2\left(\frac{u}{\beta}, \beta\underline{\epsilon}\right) F_{S_1 \otimes \overline{S}_1}\left(\frac{\underline{\epsilon}}{M}\right) \exp\left(\frac{j\underline{\epsilon}.(\mathbf{T}_i - \mathbf{T}_k)}{M}\right) d^2\underline{\epsilon}. \tag{3.4}$$

$F_{S_1 \otimes \overline{S}_1}$ represents the Fourier Transform of the convolution of a source and detector pinhole and is given by:

$$F_{S_1 \otimes \overline{S}_1}(\underline{\epsilon}) = F_{S_1}(\underline{\epsilon}) F_{\overline{S}_1}(\underline{\epsilon}) = F_{S_1}(\underline{\epsilon}) F_{S_1}(-\underline{\epsilon}) = |F_{S_1}(\underline{\epsilon})|^2 = \left(\frac{2J_1(v_p|\underline{\epsilon}|)}{v_p|\underline{\epsilon}|}\right)^2, \tag{3.5}$$

for pinholes of radius v_p in normalised optical co-ordinates. Reverting to polar co-ordinates via $\underline{\epsilon} = (\rho\cos\phi, \rho\sin\phi)$ and $d^2\underline{\epsilon} = \rho d\rho d\phi$ and performing the angular integration using the identity of Equation (A.13) allows us to write [33, 31]:

$$I_{\text{PLANE}}(u) = \sum_{i=1}^{N} \sum_{k=1}^{N} \int_0^{2/\beta} g(u,\rho) g\left(\frac{u}{\beta}, \beta\rho\right) F_{S_1 \otimes \overline{S}_1}\left(\frac{\rho}{M}\right) J_0\left(\frac{\rho}{M}|\mathbf{T}_i - \mathbf{T}_k|\right) \rho d\rho. \tag{3.6}$$

45

The integration is performed over the range of spatial frequencies, ρ, passed by the optical system.

3.2.2 Coherent Source F-DVM

Again, following Fewer *et al.* [31] and using Equation (2.52) as a starting point, and a similar procedure to that outlined above, we may write the depth response of a F-DVM employing a **coherent** source as:

$$I_{\text{PLANE}}(u) = \iint F_{S_A}\left(\frac{\boldsymbol{\epsilon}}{M}\right) F_{S_A}^*\left(\frac{\boldsymbol{\epsilon} - \boldsymbol{\epsilon}'}{M}\right) F_{\overline{S}}\left(\frac{\boldsymbol{\epsilon}'}{M}\right) P_1(u, \boldsymbol{\epsilon}) P_1^*(u, \boldsymbol{\epsilon} - \boldsymbol{\epsilon}')$$
$$\times P_2 \otimes P_2\left(\frac{u}{\beta}, \beta\boldsymbol{\epsilon}\right) \mathrm{d}^2\boldsymbol{\epsilon}\mathrm{d}^2\boldsymbol{\epsilon}'. \qquad (3.7)$$

By defining an effective pupil function via $P_{1\text{eff}}(\boldsymbol{\epsilon}) = P_1(u, \boldsymbol{\epsilon}) F_{S_A}(\boldsymbol{\epsilon})$ we have:

$$I_{\text{PLANE}}(u) = \int P_{1\text{eff}} \otimes P_{1\text{eff}}(\boldsymbol{\epsilon}) P_2 \otimes P_2\left(\frac{u}{\beta}, \beta\boldsymbol{\epsilon}\right) F_{\overline{S}}\left(\frac{\boldsymbol{\epsilon}}{M}\right) \mathrm{d}^2\boldsymbol{\epsilon}. \qquad (3.8)$$

Which, through the convolution and similarity theorems of Fourier transforms [35] can be written as [33, 31]:

$$I_{\text{PLANE}}(u) = \sum_{k=1}^{N} \int |h_{1\text{eff}}(u, \underline{\mathbf{t}})|^2 \left[\left|h_2\left(\frac{u}{\beta}, \frac{\underline{\mathbf{t}}}{\beta}\right)\right|^2 \otimes \overline{S}_1\left(M\underline{\mathbf{t}} + \underline{\mathbf{T}}_k\right)\right] \mathrm{d}^2\underline{\mathbf{t}}. \qquad (3.9)$$

The integration is performed in the plane of $\underline{\mathbf{t}}$ across the extent of the effective source and detector point spread functions. In the case of pinholes of radius v_p (in normalised optical co-ordinates) the convolution function from above reduces to that derived by

Wilson and Carlini [57]:

$$
\left| h_2 \left(\frac{u}{\beta}, \frac{\mathbf{t}}{\beta} \right) \right|^2 \otimes \overline{S}_1 \left(M\underline{\mathbf{t}} + \mathbf{T}_k \right) =
\begin{cases}
2\pi \int_0^{\frac{v_p}{M}-r} \left| h_2 \left(\frac{u}{\beta}, \frac{t}{\beta} \right) \right|^2 t\,dt \\[3em]
+2 \int_{\frac{v_p}{M}-r}^{\frac{v_p}{M}+r} \left| h_2 \left(\frac{u}{\beta}, \frac{t}{\beta} \right) \right|^2 \cos^{-1}(\alpha) t\,dt, \quad r < \frac{v_p}{M} \\[4em]
2 \int_{r-\frac{v_p}{M}}^{r+\frac{v_p}{M}} \left| h_2 \left(\frac{u}{\beta}, \frac{t}{\beta} \right) \right|^2 \cos^{-1}(\alpha) t\,dt, \qquad r \geq \frac{v_p}{M},
\end{cases}
$$

(3.10)

with $t = |\underline{\mathbf{t}}|$, $r = |\underline{\mathbf{t}} + \mathbf{T}_k/M|$, and $\alpha = [r^2 + t^2 - (v_p/M)^2]/2rt$. The effective point spread function in the forward direction, which takes into account the source array configuration, is given by:

$$
h_{1\text{eff}}(u, \underline{\mathbf{t}}) = \sum_{i=1}^{N} \int_0^1 F_{S_{1A}} \left(\frac{\rho}{M} \right) P(u, \rho) \, J_0 \left(\rho \left| \underline{\mathbf{t}} + \frac{\mathbf{T}_i}{M} \right| \right) \rho \, d\rho,
$$

(3.11)

again, the integration is performed over the supported spatial frequencies ρ. We note that this equation is more computationally intensive than the corresponding incoherent source equation due to the fact that imaging on the source and detector sides are essentially treated separately in the equations.

3.2.3 Depth response to a thick fluorescent sample

Focusing of light through an interface between refractive index mismatched media gives rise to a perturbation of the distribution of the light in the region of the focus. This perturbation is primarily due to spherical aberration and the amount is dependent on the focusing depth below the interface. Assuming an object with a higher refractive

index than that of the immersion medium[3], the main effects of this aberration are [52, 58]:

(1) An increase in the axial and lateral FWHMs of the objective lens PSF.

(2) A decrease in the maximum value of the objective PSF.

(3) An axial shift in the position where this maximum occurs.

(4) The introduction of axial asymmetry into the lens PSF.

Rigorous vector theories have been presented [53, 54, 55] which describe the behaviour of the PSF very accurately. However, in all cases, the amount of computation time required is considerable. Due to the already computationally intensive nature of our model, we choose to steer clear of a rigorous theory and instead employ the usual scalar diffraction theory along with a paraxial approximation to the film thickness similar to that employed by Kimura *et al.* [56].

In terms of points (1) and (2) raised above, the paraxial approximation should suffice. For point (1), we are solely concerned with the axial FWHM broadening and this will be taken into account of by the use of optical co-ordinates with n as the film refractive index. With regard to point (2), Török *et al.* [59] have expanded the aberration function of a wavefront which is focused through an interface between two regions with refractive indices n_1 and n_2 in terms of Zernike circle polynomials [1] and presented an equation from which the circularly symmetric Zernike co-efficients can be calculated:

$$
A_{k0} = \begin{cases} n_1 \dfrac{d \sin \alpha}{2\sqrt{2}} \left[K_0 \left(\dfrac{2n_2^2}{\sin^2(\alpha n_1^2)} - 1 \right) - K_0 \left(\dfrac{2}{\sin^2 \alpha} - 1 \right) \right], & k = 0 \\[4mm] (2k+1) \dfrac{n_1 d \sin \alpha}{4} \left[K_k \left(\dfrac{2n_2^2}{\sin^2(\alpha n_1^2)} - 1 \right) - K_k \left(\dfrac{2}{\sin^2 \alpha} - 1 \right) \right], & k = 1, 2, 3, \ldots, \end{cases}
$$

$$(3.12)$$

---

[3]In our case, air.

where $k = n/2$ for $n = 0, 2, 4, \ldots$ and the function $K_k(x)$ is given by:

$$K_k(x) = -\frac{\sqrt{2}}{(2k-1)(2k+1)} \frac{1}{(x + \sqrt{x^2-1})^{k-1/2}}$$
$$\times \left(1 - \frac{2k-1}{(2k+3)(x + \sqrt{x^2-1})^2}\right). \tag{3.13}$$

Using Equation (3.12) in conjunction with our experimental film refractive index of 1.61 (see Section 3.3.1) and objective lens NA of 0.6 gives a value for the Zernike co-efficient A_{40} corresponding to primary spherical aberration as:

$$\frac{A_{40}}{f_d} = 2.0843 \times 10^{-3}, \tag{3.14}$$

where f_d is the focusing depth. In search of a tolerance condition, we can write [1] the Strehl intensity[4], I_S, to be:

$$I_S = 1 - \frac{2\pi^2}{\lambda^2} \frac{A_{n0}^2}{n+1}. \tag{3.15}$$

If, for example, we require the intensity at the diffraction focus to be 0.99 times its unaberrated value at the Gaussian focus, Equations (3.14) & (3.15) give a maximum allowable focusing depth of $\sim 11\mu$m. This suggests that, provided we use films which are thinner than $\sim 11\mu$m the perturbation of the geometrical focus will be minimal.

In order to account for the effects described in points (3) and (4) a more rigorous model would be required; for this reason our model will not account for asymmetry which will occur in actual depth responses. However, we contend that, for our relatively small film thickness of 1.3μm (see Section 3.3.1), the model outlined above should at least describe the main trends of our experiment. We define the point of zero defocus to be the centre of the fluorescent film. This choice of origin makes physical sense as it coincides with a maximum of intensity at the detector. We use optical co-ordinates, u, to represent the displacement of the optical probe within the film; the physical film

---

[4]The maximum of the aberrated PSF as a fraction of the maximum of the unaberrated PSF.

displacement z corresponding to a given probe displacement can be calculated from Equation (2.16), using the value of the film refractive index for n. For a given position of the optical probe within the film, we integrate the probe over the axial extent of the film. Mathematically, we assume the film is infinitely wide and uniformly fluorescent in the transverse direction. Thus, the function Γ expressing its shape becomes a function of defocus alone and can be expressed as:

$$\Gamma(u') = \Pi(u'),$$
(3.16)

where we define $\Pi(x)$ as

$$\Pi(x) = \begin{cases} 1, & |x| \leq \frac{L}{2} \\ 0, & \text{otherwise.} \end{cases}$$
(3.17)

For a film of thickness L expressed in axial normalised optical co-ordinates, related to the real film thickness, d, by:

$$L = \frac{8\pi n}{\lambda} d \sin^2\left(\frac{\alpha_1}{2}\right),$$
(3.18)

where $n \sin \alpha_1 = \sin \alpha$ ($\sin \alpha$ being the objective lens NA). Again, n is the refractive index of the film. It is thus possible to define a thickness-corrected theoretical depth response, $I_{\text{FILM}}(u)$:

$$I_{\text{FILM}}(u) = \int_{-L/2}^{L/2} I_{\text{PLANE}}(u + u')\, du'.$$
(3.19)

The theory described above was implemented in C on a 233MHz Linux platform. The calculations for Equation (3.6) were performed on this platform however the calculations for Equation (3.9), being more computationally intensive, were performed on a 16 node parallel computer; the code was written in C with a message passing implementation (MPI) [60].

50

MASTER

Read in data file
Set up co-ordinate arrays
Broadcast experimental conditions to all slaves

Send jobs to slaves

Wait for reply from slave

Receive result from slave
Increment count
More jobs to do?

YES NO

Send slave another job

Kill slave

Is count=total count?

YES NO

Write
output
file

SLAVE

Wait for experimental conditions from master
Allocate memory
Initialise optimisation Matrix

Wait for job from master

Calculate a single point in film-response curve
Send result to master

Request another job

More jobs to do?

NO YES

Receive kill signal

Figure 3.1: Flow chart describing the operation of the MPI-based parallel program.

3.2.4   MPI program

We chose to operate the program using a master-slave type interface. The source code is shown in full in Appendix C. At run-time the operating system allocates 16 nodes (processors) to be used in the simulation. One of these was designated a 'master' node and was an administrative node which supplied tasks to be executed by the 'slave' nodes and collected the results before terminating slave nodes when there were no more tasks to do. Each task corresponded to one point in the $I_{\mathrm{FILM}}(u)$ curve. Essentially each slave node received a copy of the standard (non-parallel) C code which it then executed for the experimental parameters supplied by the master node. The message passing implementation is essentially a library add-on to C and a modification of a gnu C-compiler which allows efficient communication of information between the master node and all the slave nodes. Both 'broadcast' (Command: MPI_Bcast) and 'dedicated line' communication (Commands: MPI_Send and MPI_Recv) are possible. A flow chart describing the operation of the program is shown in Figure 3.1.

51

After the 16 nodes have been allocated by the OS, the master node reads in the pinhole array dimensions and other experimental parameters from an input file. The master node then sets up the co-ordinate array which describes the position of each pinhole and broadcasts these (MPI_Bcast), along with some other parameters to all slave nodes. Each slave node then sets up the appropriate memory blocks and awaits further communication. Meanwhile, the master node prepares tasks for each slave and sends one task to each slave in turn (MPI_Send). The slaves receive the tasks (MPI_Recv) and get to work executing the code. As each slave finishes it notifies the master node before sending the result. The master node then checks if any tasks remain outstanding, if so the next task is sent to the idle slave node, if not the slave is terminated and the master continues to await further communication from slaves. This process continues until the master node has received results for all the tasks which required execution. At this point, all slaves have been terminated and the master node writes the output file before itself terminating.

The program execution time for the coherent source depth response was found to increase very rapidly with the number of pinholes in the array. This was partly due to the presence of the two summations in Equation (3.9) but more importantly, influenced also by the larger number of steps in the numerical integration which were required for convergence. The relationship between convergence and the number of integration points was examined and, empirically, found to be roughly linear with the total diagonal extent of the array for the $d^2\underline{t}$ and $d\rho$ integrals, and with the pinhole diameter for the dt integrals. The number of integration points dictated by this linear relationship was used in the program, nevertheless, all calculations were also performed for a greater number of integration points to ensure that the required convergence had indeed occurred.

3.3 Experiment

3.3.1 Fluorescent Samples

A number of fluorescent compounds were examined for their suitability for use in the experiment. Two compounds in particular were promising. The first was PPV, a fluorescent polymer which was placed in solution with toluene and spin coated on a glass slide to produce uniform films of bright fluorescence with a spectral peak at 510nm when excited at the 457.9nm of an air-cooled Ar^+ laser. The second was a mixture of Coumarin-540 laser dye and polystyrene in solution with toluene which was spin-coated onto standard microscope slides and gave rise to fluorescence with a spectral peak at 540nm when excited by the Ar^+ line at 457.9nm. The fluorescence from the films was characterised using various intensities of 457.9nm Ar^+ illumination so that the nature and extent of the photobleaching could be determined.

Photobleaching

Although the exact mechanisms for photobleaching are not fully understood [42], it is known that several factors have an important impact on the rate of photobleaching. One of these is the amount of oxygen available to the fluorophore. It is thought that when the fluorophores are pumped to an excited state, the availability of oxygen can cause them to undergo a photochemical reaction with the production of a new molecule which may be non-fluorescent. Thus fluorophores which are mounted in oxygen-free environments in general exhibit less photobleaching. With this in mind, we partially enclosed the fluorescent film and sample mount in a capsule which was filled with Nitrogen gas. In the case of the Coumarin films this had the effect of vastly reducing the amount of photobleaching. In the case of the PPV films, the effect was minimal with the films still exhibiting substantial photobleaching. This suggested that, in the case of PPV, a non-oxidative process was driving the photobleaching. We thus dispensed with PPV films and concentrated on optimising the fluorescence from the Coumarin films.

The fluorescence from the Coumarin films in the oxygen-free environment now had the following properties: at low intensities (< 1mW), a small initial increase for $\sim$ 1 minute in the fluorescence intensity was observed (photo-activation [42]) before a gradual photo-bleaching driven reduction in the fluorescence. This effect was reduced somewhat by lateral scanning of the fluorescent film thereby reducing the dwell time of the excitation spot on any particular part of the film. With this arrangement, the fluorescence was found to be stable to less than 5% of the initial fluorescence intensity over a period of 10 minutes: more than sufficient time to record a depth response. With the variation in fluorescence maintained within a 5% range it was now possible to proceed with the experiment.

Film thickness profiles were measured using a Zygo white-light interferometry-based profiling system to be typically $< 3\mu$m. The particular film used in the collection of all experimental data was found to have a thickness of 1.3μm and its refractive index, which was measured by examination of the Brewster angle [2], was found to be 1.61. This is consistent with quoted refractive indices for polystyrene [61].

3.3.2 Experimental setup

A schematic of the experimental setup used is shown in Figure 3.2. An Ar$^+$ laser operating at 457.9nm served as a spatially coherent light source while a Xe arc-lamp functioned as a source of spatially incoherent light. Output from the arc-lamp was coupled into a large diameter multimode fibre, the output from which was collimated and filtered by a narrow-band interference filter to 457.9nm $\pm$ 3.4nm. The removable mirror in Figure 3.2 allowed us to switch at will between coherent and incoherent illumination. During the experiment, the collimated light from the chosen source was used to illuminate an array of pinholes arranged in a square grid. Light diverging from the pinholes was collimated by a 20cm achromat lens before being focused onto the sample by an infinity-corrected Leitz 50x/0.6 NA N-Plan objective lens. The fluoresced light was yellow-green having its peak at 540nm. A percentage of the excitation light
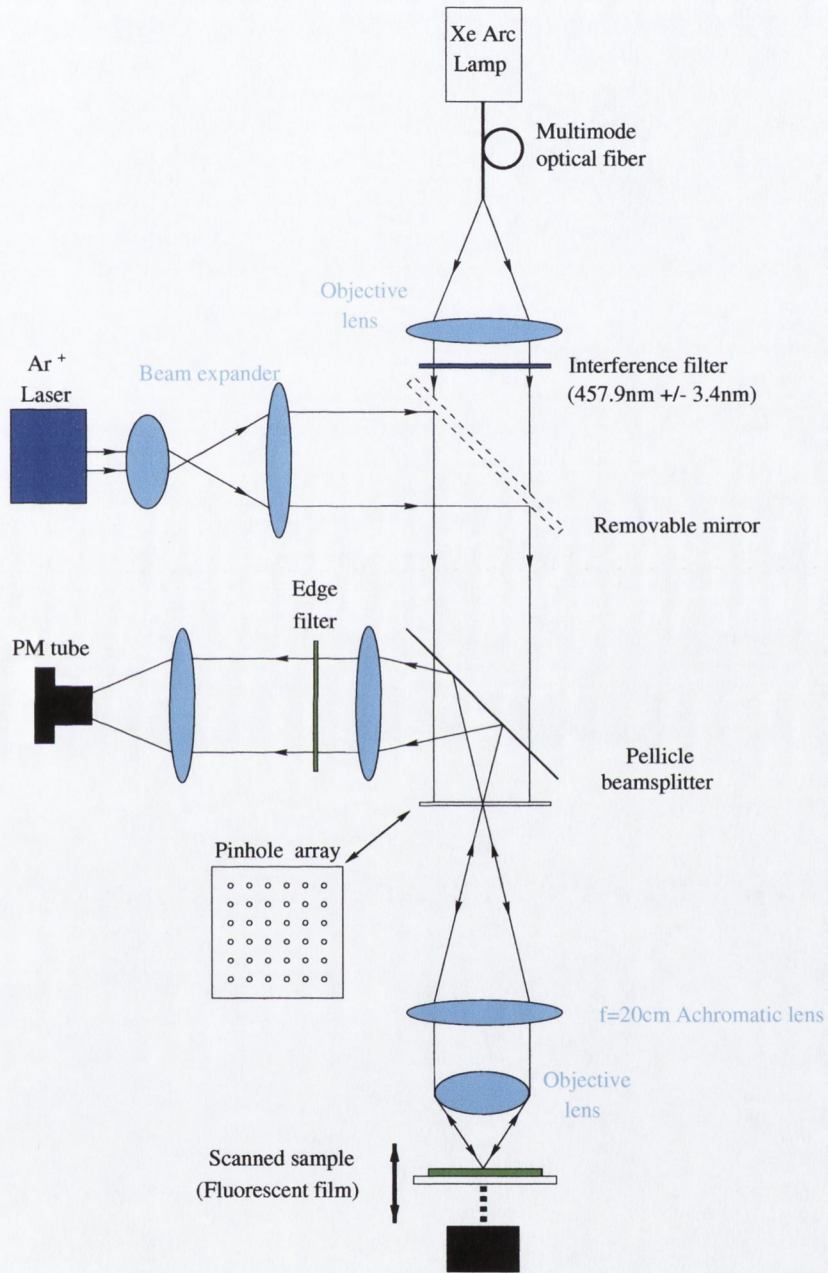
Figure 3.2: Experimental setup. Only the light emanating from one illuminated pinhole is shown for clarity.

and the fluoresced light travelled back through the objective and collimating lens before again impinging on the pinhole array. Half of the light which passed the pinhole array was directed via a pellicle beamsplitter towards an edge filter which removed the excitation light. The remaining light intensity was measured by a PM tube. By scanning the fluorescent film axially through the focal plane of the objective lens while monitoring the intensity at the PM tube, we were able to quantify the depth resolution of the system.

3.4 Results

During the experiment, it was essential that the pinhole array was Köhler illuminated [7] in order to ensure equal light intensity at all pinholes. Although this was not a problem for depth responses recorded with the laser source, we did encounter problems when using the arc-lamp due to the uneven distribution of light it produced. The use of a large diameter multimode fibre improved the situation somewhat, however it was not possible to uniformly illuminate pinhole arrays of very small lateral extent and at the same time, get enough fluorescence back from the sample. This is a particular problem in fluorescence microscopy where the fluorescence is generated at many points in the sample and propagates in many paths, a small fraction of which lead back to the pinhole array. Thus our examinations centred on two particular pinhole arrays which had the largest lateral extent available.

We first investigated the general depth imaging behaviour of said arrays using the non-thickness corrected theory before moving on to present experimental data and finally the film thickness-corrected theoretical depth responses.

3.4.1 Theoretical

Figure 3.3 shows depth response curves produced for a pinhole array consisting of pinholes of 25μm radius with a centre-to-centre spacing of 250μm. This ratio of pinhole spacing to pinhole radius (10) is in line with the guidelines as set down by McCabe
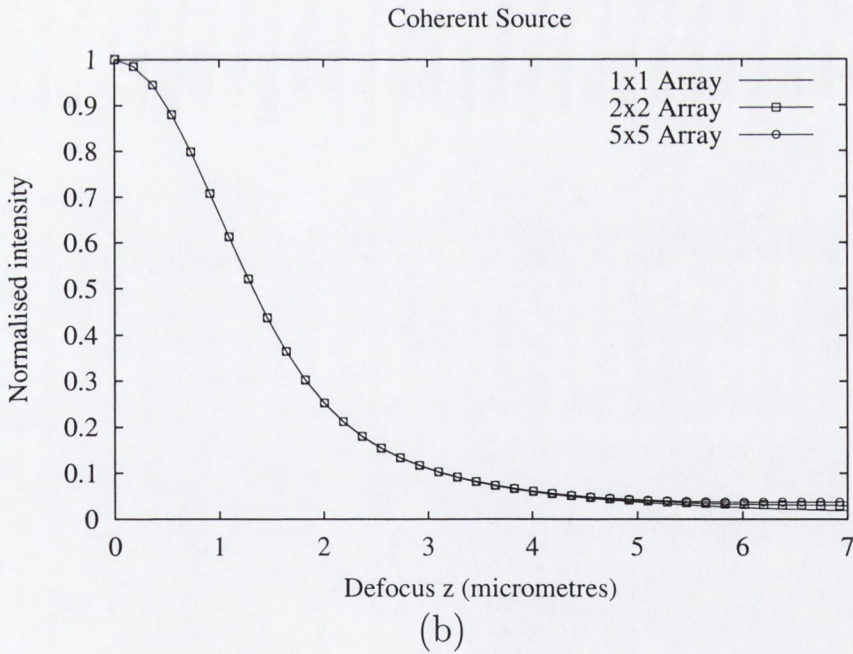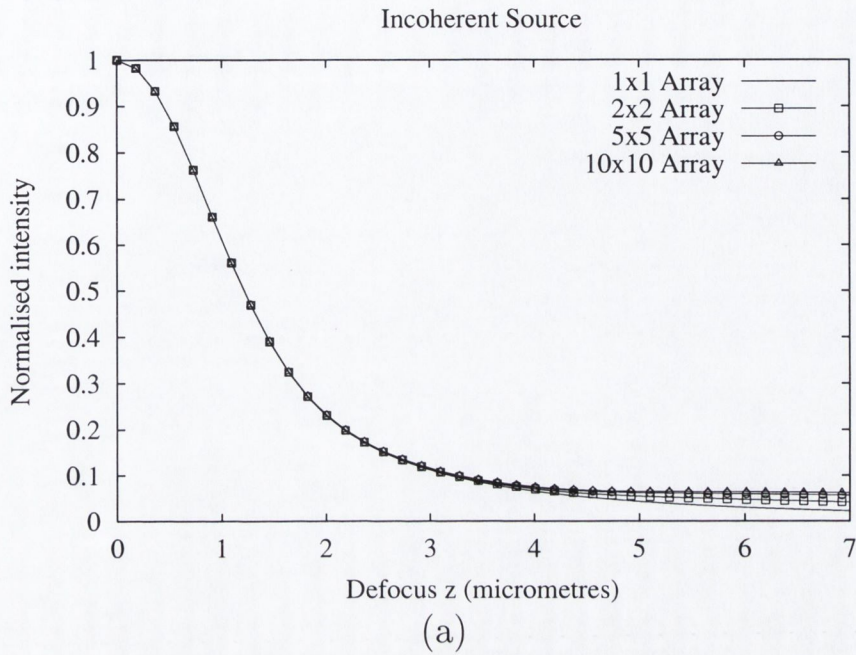
Figure 3.3: Theoretical depth responses of a F-DVM employing pinhole arrays consisting of 25μm radius pinholes with centre-to-centre spacings of 250μm. (a) Incoherent source F-DVM, depth responses are shown for 1×1, 2×2, 5×5 & 10×10 arrays; (b) Coherent source F-DVM, depth responses are shown for 1×1, 2×2 & 5×5 arrays. We note, a coherent source computation of the depth response for the 10×10 array was beyond the computation capacity of even the 16-node parallel computer due to a system run-time limit.
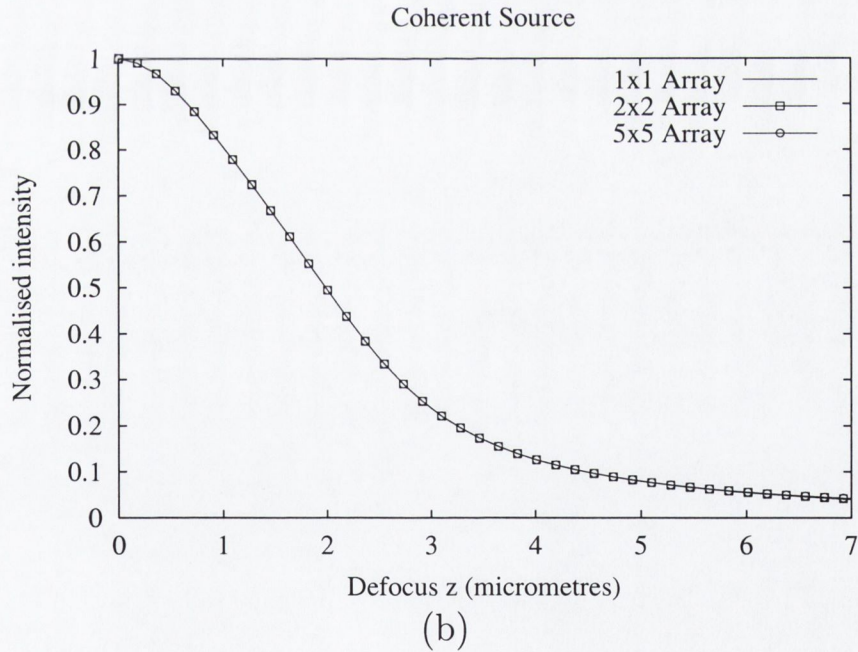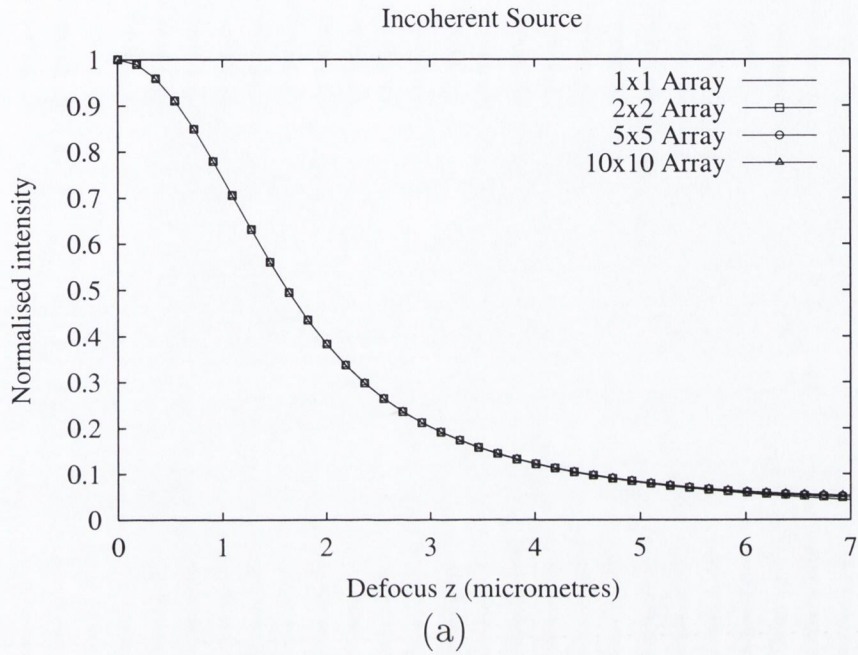
Figure 3.4: Theoretical depth responses of a F-DVM employing pinhole arrays consisting of 40μm radius pinholes with centre-to-centre spacings of 400μm. (a) Incoherent source F-DVM, depth responses are shown for 1×1, 2×2, 5×5 & 10×10 arrays; (b) Coherent source F-DVM, depth responses are shown for 1×1, 2×2 & 5×5 arrays. We note, a coherent source computation of the depth response for the 10×10 array was beyond the computation capacity of even the 16-node parallel computer due to a system run-time limit.

et al. [25] for the minimum allowable pinhole spacing to radius ratio before crosstalk effects diminish the resolution considerably. Part (*a*) of the figure shows incoherent source F-DVM depth responses, while part (*b*) shows depth responses for a coherent source F-DVM. It is clear from the figure that, in the case of this particular array, varying the number of pinholes in the array has negligible effect on the depth response. Another interesting detail to note from Figure 3.3 is the lack of any sidelobes in the case of the depth response of the coherent source F-DVM as first predicted by Fewer *et al.* [31]. We note that, although in the case of this array there is a complete absence of sidelobes, of course, sidelobes will be present for many arrays. In general, however, in F-DVMs employing coherent sources the sidelobes will be comparable to those seen in single pinhole DVMs. This is in contrast to what is observed in the depth responses of coherent source **brightfield** DVMs [30, 62, 63](see also Chapters 4 & 5) where coherent crosstalk between pinholes gives rise to considerable sidelobes in the depth response. Essentially, the incoherent nature of the generated fluorescence has the effect of countering the coherent-crosstalk-induced sidelobes which would normally be present.

A comparison of the FWHM of the depth responses of the 1×1 arrays of parts (*a*) and (*b*) reveals that the coherent source F-DVM has a slightly inferior axial resolution at 2.64μm compared to 2.43μm for the incoherent source F-DVM. We will examine this effect further in Section 3.4.3. Figure 3.4 depicts theoretical depth responses to a plane for a pinhole array consisting of pinholes of 40μm radius with a centre-to-centre spacing of 400μm: again, the ratio of pinhole spacing to pinhole radius was chosen as 10. The figure shows similar trends to that of Figure 3.3, again the effect on the depth response of varying the number of pinholes in the array is seen to be minimal, and the coherent source F-DVM shows inferior axial resolution to the incoherent source F-DVM (3.98μm compared to 3.25μm in the case of the 1×1 arrays). On comparing both figures we note that the arrays featured in Figure 3.3 exhibit superior depth resolution to those of Figure 3.4. This is simply due to the smaller pinhole diameter used in the former set of arrays.

We finally note that, in the case of the coherent source F-DVM, curves for the 10×10 array are absent due to the fact that they proved too computationally intensive to simulate. However, due to the similarity between depth responses of the 1×1, 2×2, and 5×5 arrays, we can assume that the 10×10 array will have almost identical imaging properties to the rest. This fact is useful as it allows us to simulate the depth responses of 5×5 arrays in place of 10×10 arrays whenever the computation times of the latter become too extreme.

3.4.2   Experimental

Experimental depth responses were recorded, using the experimental setup shown in Figure 3.2. Again, the two pinhole arrays examined consisted of 10×10 arrays of $25\mu m$ and $40\mu m$ radius pinholes with centre-to-centre pinhole spacings of $250\mu m$ and $400\mu m$ respectively. The experimental depth responses (see Figures $3.5(a)$ & $3.6(a)$) were found to be considerably broadened when compared to the idealised depth responses of Figures 3.3 & 3.4. We accounted for this broadening effect by employing Equation (3.19) in conjunction with Equations (3.6) & (3.9). The resulting, film-thickness corrected, theoretical depth responses are shown in parts (b) of Figures 3.5 & 3.6. We note that, in the coherent source case, as it was not possible to model the 10×10 array, the curves simulated for the 5×5 array were used instead. As discussed in the previous section, this approach is justified by the fact that, in the case of this particular array, the depth response curves were not found to vary significantly with the number of pinholes.

Looking first at Figure 3.5, we note the same trends in both parts of the figure. In both cases, the FWHM of the coherent source depth response is greater than that of the incoherent source depth response; we will examine this effect further in Section 3.4.3. Due to the unstable nature of the fluoresced light, in particular the photobleaching effect mentioned in Section 3.3.1, there is a discrepancy between the background levels of the experimental as compared to the theoretical curves. However, we see the same
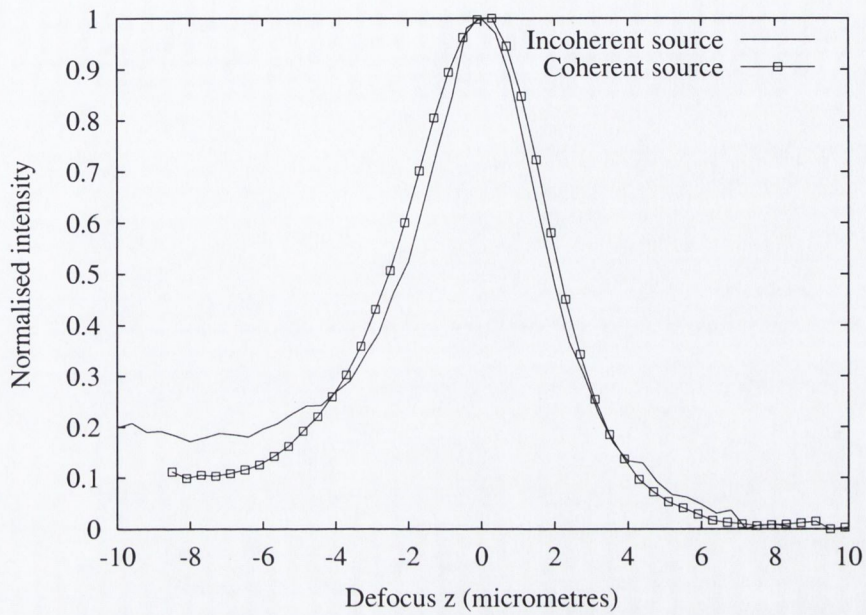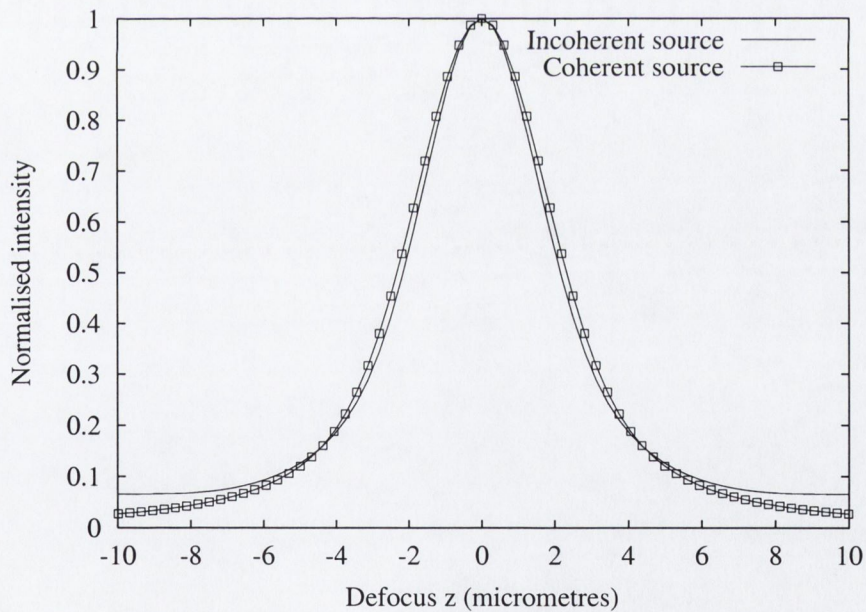
Figure 3.5: Depth response curves for a thick fluorescent film for incoherent and coherent source F-DVMs employing 10×10 pinhole arrays with pinhole radii of 25μm and centre-to-centre pinhole spacing of 250μm. (a) Experimental depth responses; (b) Thickness-corrected theoretical depth responses.
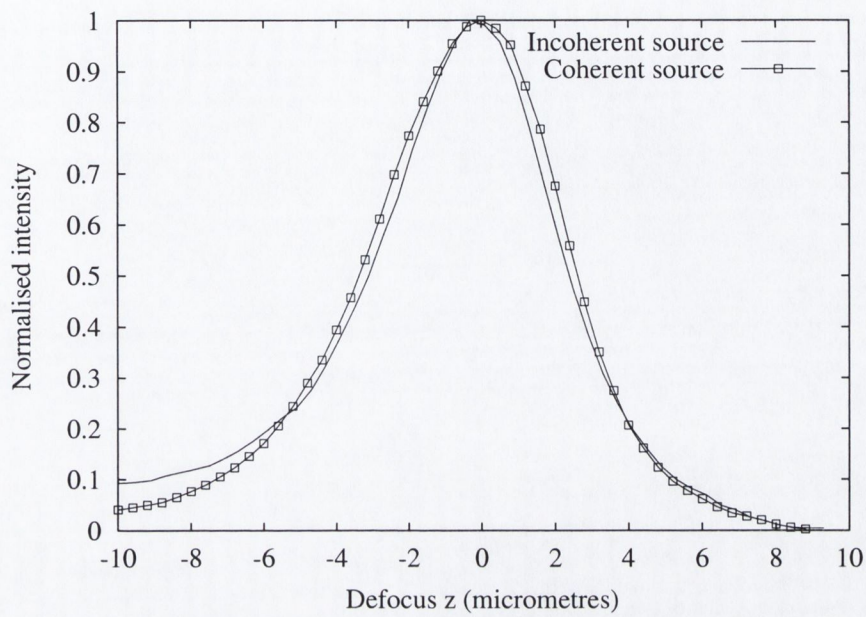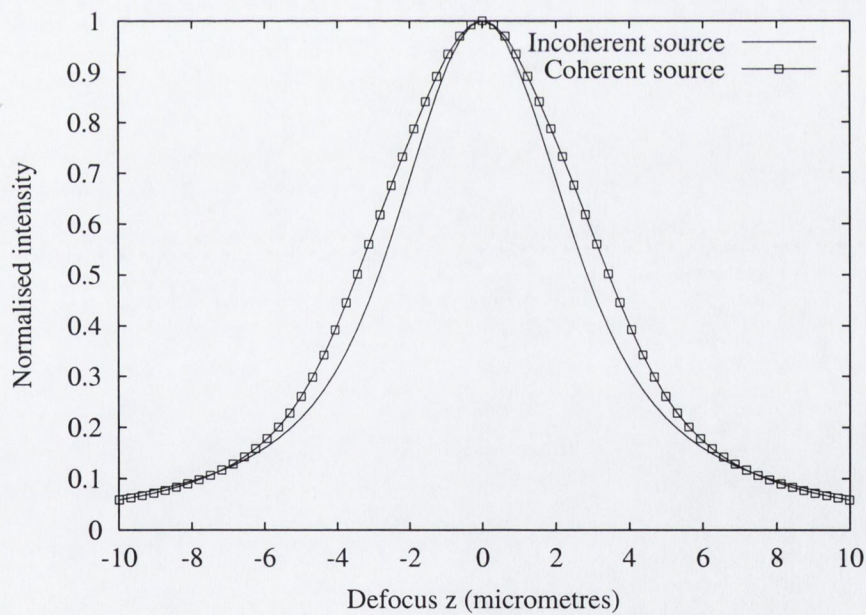
Figure 3.6: Depth response curves for a thick fluorescent film for incoherent and coherent source F-DVMs employing 10×10 pinhole arrays with pinhole radii of 40μm and centre-to-centre pinhole spacing of 400μm. (a) Experimental depth responses; (b) Thickness-corrected theoretical depth responses.

general trends which are predicted by the theory. The asymmetry present in the experimental data is not predicted by the model due to the effects discussed in Section 3.2.3.

We now move on to examine Figure 3.6. Again, on comparing parts (*a*) & (*b*) we see that the theoretical and experimental curves follow the same trends: the coherent source F-DVM exhibits inferior optical sectioning. Again, the background level is higher on one side of the experimental depth response due to photobleaching and other asymmetry is present due to aberrations induced by focusing through an interface between refractive index mismatched media. In conclusion, the paraxial approach outlined in Section 3.2.3 appears to describe the broad features of the experimental trends witnessed, with the thickness-corrected curves having similar characteristics to the experimental curves. The two most significant facts verified by the experiment are the lack of enhanced sidelobes in the coherent source depth responses and the superior depth resolution of the incoherent source F-DVM over the coherent source F-DVM, in this case. We now move on to examine this last point in more detail in order to ascertain whether this is the general behaviour.

3.4.3 Variation of optical sectioning strength with pinhole array dimensions

In order to determine whether coherent source F-DVMs, in general, exhibit inferior optical sectioning to incoherent source F-DVMs, we examined the FWHMs of theoretical depth responses for a variety of pinhole sizes for both coherent and incoherent source single pinhole F-DVMs. This approach is identical to that employed by Wilson and Hewlett [33] and will allow us to make qualitative statements about the nature of the differences between the coherent and incoherent source cases. We choose to examine the limiting case of $\beta = 1$ (equal excitation and fluorescence wavelengths). We thus present Figure 3.7. From this figure we see that the depth resolution of F-DVMs employing infinitely small pinholes ($v_p = 0$) is independent of source coherence. For
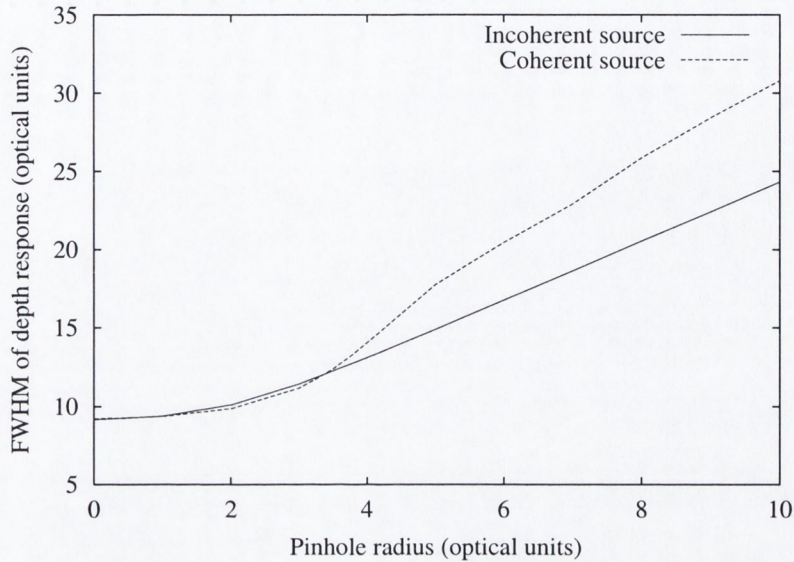
Figure 3.7: The variation in the FWHM of single pinhole F-DVMs with pinhole radius. The solid curve represents an incoherent source F-DVM and the dashed curve represents a coherent source F-DVM. There are two points at which the curves crossover. At $v_p = 0$ and $\sim v_p = 3.5$.

pinhole radii of up to $\sim v_p = 1$ optical unit ($\sim 8.4\mu m$ in our experimental setup) the depth resolution is likewise independent of source coherence. Beyond pinhole radii of 1 optical unit it can be seen that coherent source F-DVMs have **superior** resolution to incoherent source F-DVMs. The situation is reversed at $\sim v_p = 3.5$ optical units where a crossover point between the two curves occurs. For pinhole radii greater than the value at this crossover point, the depth resolution of a coherent source F-DVM can be seen to degrade significantly faster than the corresponding incoherent source F-DVM.

We note that the crossover occurs close to the point where the effective pupil function $F_{S_{1A}}\left(\frac{\omega}{M}\right) P(u, \omega)$ in Equation (3.11) first becomes negative. The figure suggests that provided $v_p/M \leq 3.5$, the depth resolution performance of single-pinhole coherent source F-DVMs will either equal or exceed the depth resolution of the corresponding incoherent source F-DVM, a fact not previously presented to our knowledge. In our experimental setup this crossover point corresponds to an actual pinhole radius of

64

21μm.
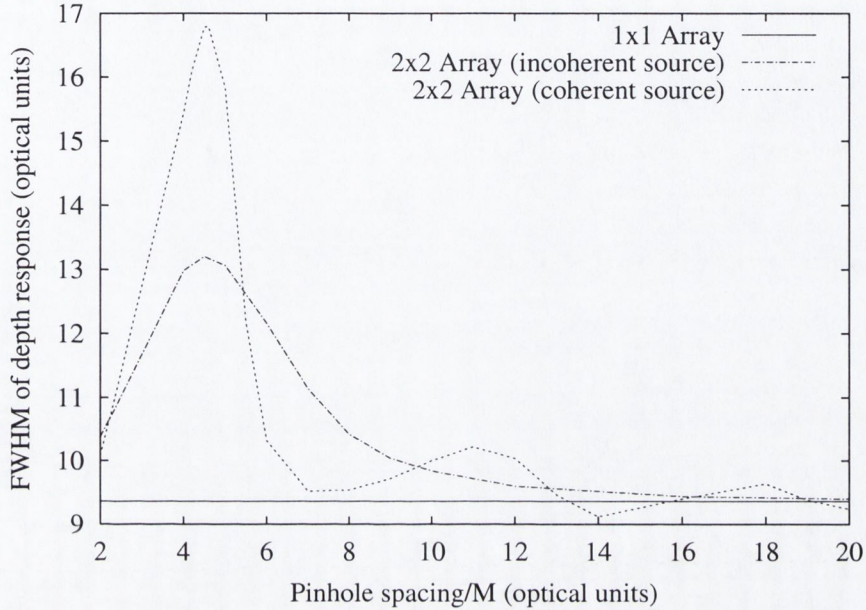
Figure 3.8: Variation of the FWHM of the depth response with pinhole spacing for 1×1 and 2×2 pinhole arrays employing pinholes of $v_p/M = 1$ optical unit.

In an attempt to extend our analysis of single pinhole systems to those employing multiple pinholes, we examine the computationally efficient case of a 2×2 array; we again fix $\beta = 1$. The FWHMs were extracted from the depth responses of 2×2 arrays of pinholes with pinhole radius (in the object plane) of $\frac{v_p}{M} = 1$ optical unit. The pinhole spacing (in the object plane) was varied from the lowest physically possible spacing of $\frac{R}{M} = 2$ optical units to $\frac{R}{M} = 20$ optical units and the behaviour was recorded for F-DVMs employing both coherent and incoherent sources. The results of this examination are shown in Figure 3.8. In the case of the incoherent source F-DVM, the behaviour of the FWHM is predictable dropping smoothly towards the single pinhole value as the pinhole spacing is increased. At a spacing of 20 optical units, the FWHM is almost indistinguishable from the FWHM of the single pinhole DVM. The coherent source F-DVM, on the other hand, shows more oscillatory behaviour with the FWHM being in places greater than and in other places less than that of the incoherent source F-DVM.

65

This is the result of interference between the field amplitudes produced by each pinhole on the sample. Such behaviour has been commented on recently by Egner and Hell [49] for an real-time confocal system employing a microlens array and operating in 2 and 3-photon fluorescence mode. The authors have stated that when the adjacent foci are close enough in the focal plane to interfere, the axial resolution, in general, will be poorer than that of the single pinhole case. Figure 3.8 shows that, at least in single photon F-DVMs, this is not the case. In fact, the axial resolution is alternately worse and better than the single pinhole case as the pinhole spacing is increased. If the depth resolution is to be optimised, such interference is an important factor to be considered when choosing an appropriate array for imaging. The difference between the FWHMs of coherent and incoherent source depth responses decreases as the pinhole spacing is increased being almost identical at a pinhole spacing of 20 times the pinhole radius or greater. This suggests that coherent source F-DVMs should perhaps employ pinhole arrays in which the pinholes are spaced twice as far apart as they would be in incoherent source F-DVMs. Of course, the high intensity nature of coherent sources would more than compensate for the decrease in the optical throughput of the array which this dictates. The effects witnessed in this figure would, in some cases, be more pronounced in the case of a pinhole array employing a greater number of pinholes. Although, in the case of the 10×10 arrays we have examined, as Figures 3.3 & 3.4 show, this is not the case. The number of pinholes having negligible effect on the depth response.

3.5   Conclusions

We have directly compared the experimental optical sectioning characteristics of coherent and incoherent source fluorescence-mode direct-view microscopes for the first time. The experimental depth response curves were found to be considerably broadened when compared with the theoretical 'depth response to a plane'. We related this effect to the finite thickness of the fluorescent films used and accounted for it by using a paraxial modification to the usual scalar diffraction theory. The modified theory was

implemented in C on a fast parallel processor network. Communication between the pool of processors was made possible by employing a message passage implementation (MPI) library add-on for C along with a modified compiler. The resulting thickness-corrected depth responses were found to follow the trends of the experimental curves. Previous theoretical work [31] had predicted that the optical sectioning strength of F-DVMs should be largely independent of source coherence. This prediction was shown to be partially incorrect. Both theoretical and experimental curves revealed inferior resolution for the coherent source F-DVM. Further theoretical analysis revealed that this inferior resolution in the coherent source case was related to two separate effects as demonstrated by Figures 3.7 & 3.8 respectively. The first is an effect due solely to the size of the pinhole: above a critical size the depth resolution of the coherent source F-DVM is inferior to that of the incoherent source F-DVM. Figures 3.3 & 3.4 showed that this pinhole-size related effect was also present in the depth responses of multiple-pinhole arrays. The second effect arises from interference between adjacent parts of the effective source PSF and becomes an issue in multiple-pinhole F-DVMs where careful choice of the pinhole spacing is required to ensure optimum performance. Our analysis suggests that in F-DVMs employing coherent sources, the ratio of pinhole spacing to pinhole radius should be set at double the usual value of 10 in order to achieve comparable depth sectioning to that of incoherent source F-DVMs. From a lateral resolution point of view, Fewer *et al.* have recommended that coherent source F-DVMs employ pinhole spacings (in the object plane) of at least 20 optical units. This two criteria specify the optimum design parameters for a coherent source F-DVM. The decrease in throughput, with respect to incoherent source F-DVMs, which they dictate is easily offset by the benefits of coherent over incoherent radiation: narrow linewidth, high directionality and uniformity, and high brightness.

In the case of the arrays we examined experimentally, the main effect causing the difference between the FWHM of the depth responses of coherent and incoherent source F-DVMs is the diameter of the pinholes rather than the spacing between them. This is evidenced by Figures 3.3 & 3.4 which show that the number of pinholes had very

little effect on the depth response in this case.

Chapter 4

Programmable array microscopy

In the previous chapter, we performed an examination of fluorescence DVMs employing both coherent and incoherent light sources. We now move on to perform an experimental study of the imaging performance of brightfield or reflection mode DVMs which are typically used in the imaging of semiconductor samples. The chapter presents an example of a novel DVM design: a programmable array microscope (PAM) which uses a pair of ferroelectric liquid crystal spatial light modulators (FLC SLMs) to achieve confocal imaging [63, 64, 65]. The system is similar to the direct-view microscope (DVM), in which scanned pinhole arrays are used to obtain real-time confocal images. The PAM, unlike typical DVMs, allows arrays to be programmed and scanned electronically rather than mechanically; thus having the advantage of a lack of moving parts, and complete control over the aperture function.

In our system, one SLM is placed in the source plane of a conventional microscope system; the other is placed in the detector plane. DVM-type aperture arrays are displayed and scanned synchronously on the SLMs and confocal imaging results. We describe some system artifacts before presenting measurements of the optical sectioning properties of a variety of aperture arrays. The system uses a coherent light source and we note some effects of the source coherence on the depth response curves. The use of aperture correlation techniques to improve the light throughput in the devices is briefly investigated.

4.1 Introduction

In Chapter 1 we introduced the direct-view or tandem-scanning microscope as a confocal microscope which offered increased rates of image acquisition over standard confocal scanning microscopes. Details were given of a system built by Xiao *et al.* [22] which relied for its operation on a Nipkow disc. Such systems have the disadvantage of relying on mechanical scanning and thus can be prone to mechanical wear and tear. Furthermore, during practical use of the instrument, it may be necessary to change the dimensions of the pinhole array employed. For example, pinholes of a certain radius might fill the entrance pupil of one objective lens while under-filling or over-filling the next. The optimal pinhole array dimensions will also vary according to the type of imaging to be performed. For example, in a DVM which is used to record auto-focus images (see Section 1.2), the background in the depth response is of secondary importance: so long as it is lower than the main peak, auto-focus images can be successfully recorded. Thus, the pinholes in the array could be spaced much closer together thus allowing the available light to be used much more efficiently. It is clear that the ideal aperture array dimensions are likely to vary widely depending on the exact nature of the imaging and the object under inspection.

A recent DVM design which is a more versatile instrument is one which relies for its operation on a spatial light modulator– essentially an electrically controlled two-dimensional modulation device. This idea was first disclosed by IBM in 1993 [66]. Such a device allows an arbitrary aperture function to be programmed into the system, hence the term programmable array microscopy(PAM). The first report of a working system was by Liang *et al.* [67] who constructed such a device around a digital micro-mirror device(DMD) [68] -type SLM. The DMD, which is not presently (Oct. 2001) available as an OEM product, consists of an array of micro-mirrors each of which is tiltable through $\pm 10°$ relative to the surface normal by the application of the appropriate voltage. Liang examined depth response curves recorded for such a system utilising a coherent light source. However, only the FWHMs of the depth responses were re-

ported; no qualitative comments were made about the structure of the depth responses themselves.

In this chapter we describe a coherent source programmable array microscope which uses a pair of ferroelectric [69] liquid crystal spatial light modulators (FLC SLMs) to achieve confocal imaging [64]. Traditionally, DVMs have employed circular apertures in the Nipkow disc whereas PAMs have thus far used square apertures. We ascertain whether this is likely to cause a loss of depth resolution. We next present experimental depth response curves which demonstrate the effects of coherent light sources on the optical sectioning of our PAM implementation. We briefly investigate an implementation of aperture correlation which is well-suited to FLC devices.

4.2   Device details

A spatial light modulator (SLM) is essentially a 2-D array of optical apertures each of which is individually addressable. Application of the appropriate voltage to a particular aperture causes it to open or close as desired. Optical wavefronts which are incident on such a device can have a desired modulation imposed across them. Various SLM technologies exist, which make use of different techniques of encoding the modulation pattern across a wavefront; two which have been used to date for PAM systems are the Texas Instruments Digital Micro-mirror Device (DMD) [67, 70], and a twisted-nematic liquid-crystal SLM [71]. We use instead the Displaytech ferroelectric liquid crystal SLM [72]. All of these SLMs are fast, high-resolution modulators. However the FLC SLM is perhaps a more versatile device, having two modes of operation, binary amplitude modulation and binary phase modulation. It also has a speed advantage over a twisted-nematic device with switching speeds of up to 5kHz as compared to $10 - 100$ Hz for a typical twisted nematic device[71].

The particular SLM we use (part of the Displaytech SLM developer kit [72]) consists of a birefringent crystal layer with two stable optic axis orientations which are 45° apart. An array of micro-mirrors behind the FLC layer makes the device reflective,

71

and controlling circuitry allows the mirrors, and hence the FLC, to be electrically addressed. By applying a voltage to a given micro-mirror, and thus across the local crystal sandwich, the local optic axis orientation can be rotated into one of two stable orientations; the device is designed so that the two stable optic axis orientations result from the application of ± 5V across the liquid crystal.

4.3 FLC SLM as a binary amplitude modulator
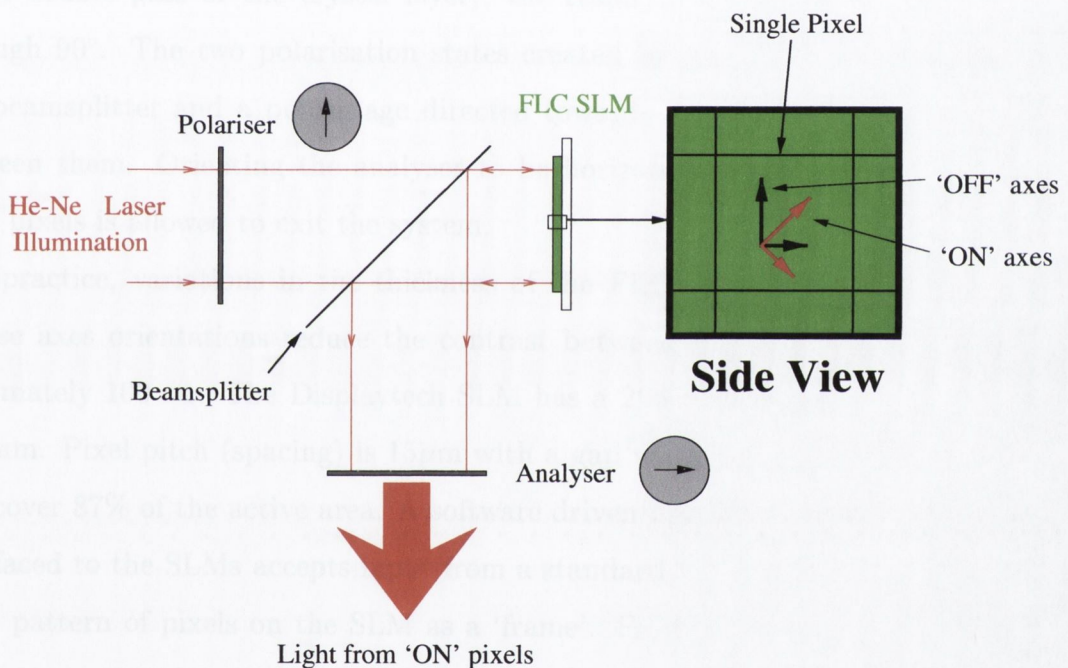
Figure 4.1: FLC SLM in binary amplitude modulation mode

Implementation of our PAM requires operation of the FLC SLMs in binary amplitude modulation mode; this is achieved using the optical setup depicted by Figure 4.1. The He-Ne laser cavity was rotated so that the output polarisation was parallel to a vertically oriented polariser. On passing the polariser, the light was allowed to propagate through a beamsplitter before impinging on the SLM. We refer to each micro-mirror on the SLM as a pixel. The two optic axis configurations of the SLM are

shown in the (single pixel) side view; the black (vertical and horizontal) axes represent the 'OFF' state of the SLM while the red axes (at 45° to the 'OFF' axes) represent the 'ON' state of the system. In each case the longer of the two axes represents the 'fast' axis and the shorter line represents the 'slow' axis. Vertically polarised light encountering a pixel which is 'OFF' has no component of polarisation along that pixel's 'slow' axis and therefore traverses the system with polarisation unchanged. Conversely, vertically polarised light encountering an 'ON' pixel has an equal component of polarisation along both the 'fast' and 'slow' axes and, because the device is a half-wave plate at 632.8nm (on a double pass of the crystal layer), the result is a rotation of the polarisation through 90°. The two polarisation states created by the SLM are reflected towards the beamsplitter and a percentage directed towards an analyser which discriminates between them. Orienting the analyser to be horizontal ensures that only light from 'ON' pixels is allowed to exit the system.

In practice, variations in the thickness of the FLC layer across the SLM and the precise axes orientations reduce the contrast between 'ON' and 'OFF' pixels to approximately 100 : 1. The Displaytech SLM has a 256×256 pixel active area, of side 3.84mm. Pixel pitch (spacing) is 15μm with a gap width of 1μm, and thus pixel mirrors cover 87% of the active area. A software driven hardware module ('SLiM driver') interfaced to the SLMs accepts input from a standard PC parallel port. We refer to a given pattern of pixels on the SLM as a 'frame'. Frames are loaded into the module memory as monochrome 256×256 bitmaps; 128 such frames can be stored in memory at any one time. The hardware module supplies several synchronising signals which direct the timing of image acquisition. Frames can be updated on the SLM at rates ranging from 2Hz to 2.5kHz.

4.4 Experimental setup

Figure 4.2 shows a diagram of the experimental setup. A plane wave He-Ne laser source at 632.8nm illuminates the first SLM. The modulated wavefront is reflected
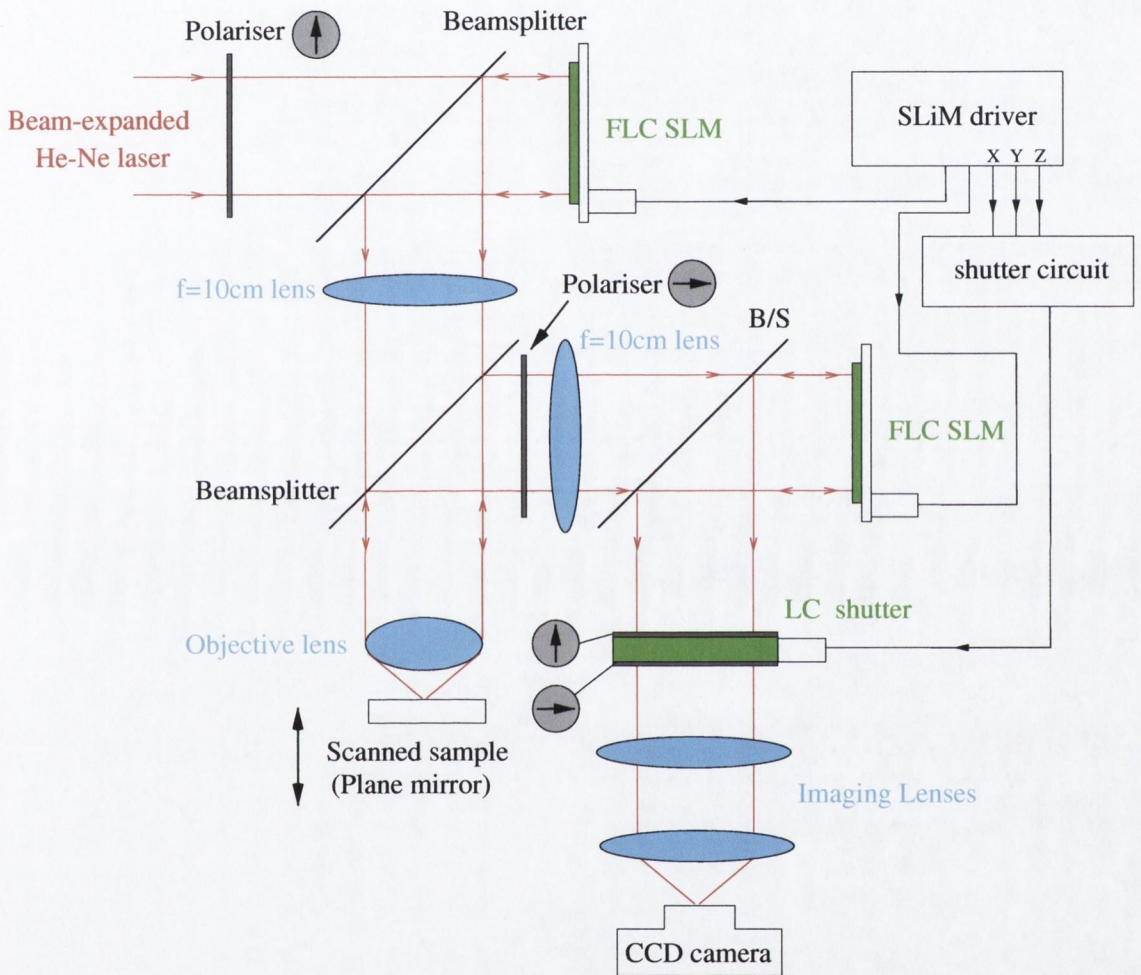
Figure 4.2: A programmable array microscope system employing FLC SLMs. The outputs from the SLiM driver module X, Y, & Z are 'Inverse Frame', 'Image Valid', & 'SLM Select'.

back towards a beam-splitter where it is directed via a collimating 10cm focal length lens to an infinite tube-length objective lens:– a 10cm lens was chosen as it allowed us to keep the system relatively compact and maintain an acceptable field of view on the sample. Light reflected from the area of the sample illuminated by the objective lens was directed via a second beam-splitter and focused by a second 10cm lens onto the second SLM. The wavefront again experiences a modulation before being reflected towards the CCD camera via the imaging lenses. The polarisers serve to block light which has been reflected from SLM pixels which are switched off. The nature of the FLC devices used requires that the time averaged electric field across any area of the liquid crystal be zero. This means that after a given frame is displayed for a time on the SLM, the inverse frame must be displayed and for an equal length of time:— so-called 'charge balancing'. It is necessary therefore to sample the display cycle of the SLM in order to exclude the inverse frames, as well as the period needed for the frames on both SLMs to be updated. This fact places limits on the maximum scan speed we can attain with a 2 SLM system of 625Hz.

For sampling purposes we use a liquid crystal (LC) shuttering system which is driven open when normal frames are present on both SLMs and driven closed when inverse frames, or intermediate frames in the loading sequence, are present. The LC shutter is based on FLC technology [69, 73]; the device is essentially a layer of FLC placed between two crossed polarisers. When in the 'open' state a wavelength-dependent rotation of $\sim 90°$ is applied to incident light with the result that it is allowed to traverse the crossed polarisers. The device can be optimised for a particular wavelength by careful orientation of the polarisers. The shutter opens on application of $+5V$ across the FLC layer, and closes when $-5V$ is applied across the FLC layer. A simple logic circuit (Figure 4.3) was built to supply the correct signal to the shutter. The circuit outputs $+5V$ (open shutter) when **all** of the following conditions are satisfied:

- The 'Inverse Frame' output is low. This ensures that we are dealing with normal rather than inverse frames.
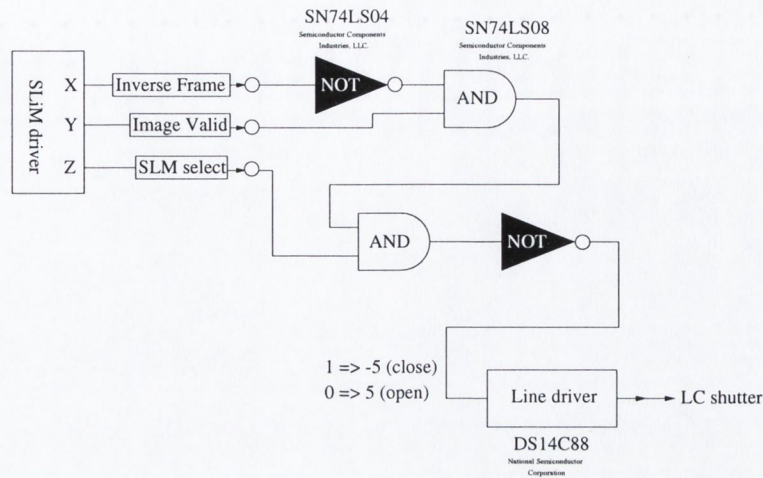
Figure 4.3: LC shutter driving circuit. The line driver produces $-5V$ for every CMOS high ($5V$) received, and $+5V$ for every CMOS low ($0V$) received.

- The 'Image Valid' output is high. This simply ensures the whole of the current frame has been successfully displayed.

- The 'SLM Select' output (high when SLM 2 was last written to) is high. Because we choose to write each frame to SLM 1, followed by SLM 2: when SLM select is high, both SLMs are displaying the current frame.

When **any** of the above conditions is not satisfied, $-5V$(close shutter) is sent to the LC shutter.

After sampling of the wavefront, the imaging lenses (Figure 4.2) serve to form an appropriately scaled image on the CCD camera. By displaying appropriate aperture arrays in synchronism on both SLMs, the device behaves similarly to a direct-view microscope; the aperture arrays can be scanned to image an area on a sample confocally. The fact that SLMs generally consist of an array of square pixels necessitates the use of square apertures in the aperture array and the arrangement of apertures in a square grid allows uncomplicated scanning. Whilst scanning such an aperture pattern across the surface of both SLMs, depth responses are recorded by stepping a plane mirror along the optic axis through the focal plane of the objective lens and noting the light

76

intensity at the CCD camera at each axial position.

4.5 Theory: optical sectioning strength predicted by scalar diffraction theory

Before proceeding with the details of the experimental data, it is necessary to introduce some equations which describe the optical sectioning behaviour of the system. First we present an expression describing the depth response of a DVM-like system employing arrays of **circular** apertures [30], before moving on to show how we have adapted the equation to account for the use of **square** apertures.

4.5.1 Circular apertures

In order to arrive at an expression for the depth response of a coherent source Bright-field DVM employing circular apertures, we follow the method of Hewlett *et al.* [30] and start with the instrument's optical transfer function $C(u, \underline{\mathbf{m}}; \underline{\mathbf{p}})$(Equation (2.51)). As stated in Chapter 2 (Section 2.7), the planar response of the instrument is described by $C(u, 0; 0)$. We specify a finite array of N source/detector apertures each of amplitude/intensity sensitivity $S_{1A}(\underline{\mathbf{t}}_1)$ centred at points $\underline{\mathbf{T}}_1, \underline{\mathbf{T}}_2, ..., \underline{\mathbf{T}}_N$ such that the source array S_A can be written as:

$$S_A(\underline{\mathbf{t}}_1) = \sum_{i=1}^{N} S_{1_A}(\underline{\mathbf{t}}_1 - \underline{\mathbf{T}}_i). \tag{4.1}$$

As usual, we represent the detector array by $\overline{S}$ where the over-line indicates the fact that the light is travelling in an opposing direction to that of the excitation light and so the co-ordinate system is inverted. We note that when we refer to the detector array we drop the additional subscript 'A' to remind ourselves that the detector apertures respond to intensity rather than amplitude. By further specifying the source/detector

Fourier transforms via Equation (3.3), we can write the depth response as:

$$
I_{\text{PLANE}}(u) = \sum_{i=1}^{N} \sum_{k=1}^{N} \sum_{l=1}^{N} \int\!\!\int F_{\overline{S}_1}\left(\frac{\boldsymbol{\epsilon} - \boldsymbol{\epsilon}'}{M}\right) F_{S_{1A}}\left(\frac{\boldsymbol{\epsilon}}{M}\right) F^*_{S_{1A}}\left(\frac{\boldsymbol{\epsilon}'}{M}\right)
$$
$$
\times \exp\left(\frac{-j}{M}\boldsymbol{\epsilon}.(\mathbf{T}_i - \mathbf{T}_l)\right) \exp\left(\frac{j}{M}\boldsymbol{\epsilon}'.(\mathbf{T}_k - \mathbf{T}_l)\right)
$$
$$
\times P_1(u, \boldsymbol{\epsilon}) P^*_1(u, \boldsymbol{\epsilon}') P_2(u, \boldsymbol{\epsilon}) P^*_2(u, \boldsymbol{\epsilon}') d^2\boldsymbol{\epsilon} d^2\boldsymbol{\epsilon}'. \tag{4.2}
$$

In the case of circular apertures (pinholes) of radius v_p, $F_{S_{1A}}(\boldsymbol{\epsilon})$ (the Fourier transform of the individual source pinhole) is given by:

$$
F_{S_{1A}}(\boldsymbol{\epsilon}) = \frac{2J_1(v_p|\boldsymbol{\epsilon}|)}{v_p|\boldsymbol{\epsilon}|}. \tag{4.3}
$$

By expressing $F_{\overline{S}_1}$ via Equation (B.2) and, assuming identical objective and collector lenses we move to a polar form of Equation (4.2). After performing the innermost angular integration using Equation (A.13) we arrive at the expression presented by Hewlett *et al.* [30]:

$$
I_{\text{PLANE}}(u) = \sum_{k=1}^{N} \int_0^{2\pi} \int_0^{v_p} \left| \sum_{i=1}^{N} \int_0^1 P(2u, \rho) F_{S_1}\left(\frac{\rho}{M}\right) \right.
$$
$$
\left. \times J_0\left(\frac{\rho}{M}|\mathbf{T}_i - \mathbf{T}_k - \mathbf{t}|\right) \rho d\rho \right|^2 r dr d\theta. \tag{4.4}
$$

With $\rho = |\boldsymbol{\epsilon}|$ and $\mathbf{t} = (r\cos\theta, r\sin\theta)$.

4.5.2   Square apertures

In the case of our present experiment we are dealing with a PAM utilising square apertures. As shown in Appendix B.1, if we again assume identical lenses we have (from Equation (4.2)), for a square $n \times n$ array of square apertures, of side t_p, and

centre-to-centre spacing R:

$$I_{\text{PLANE}}(u) = \int_{-\frac{t_p}{2}}^{\frac{t_p}{2}} \int_{-\frac{t_p}{2}}^{\frac{t_p}{2}} \left| \int_0^{2\pi} \int_0^1 F_{S_{1A}} \left(\frac{\rho \cos \phi}{M}, \frac{\rho \sin \phi}{M} \right) P(2u, \rho) \right.$$

$$\times \frac{\sin^2 \left(\frac{nR\rho \cos \phi}{2M} \right) \sin^2 \left(\frac{nR\rho \sin \phi}{2M} \right)}{\sin^2 \left(\frac{R\rho \cos \phi}{2M} \right) \sin^2 \left(\frac{R\rho \sin \phi}{2M} \right)}$$

$$\left. \times \exp \left(\frac{j\rho}{M} (t \cos \phi + w \sin \phi) \right) \rho d\rho d\phi \right|^2 dt dw. \qquad (4.5)$$

In this case, $F_{S_{1A}}$ is given by [2]:

$$F_{S_{1A}}(a, b) = \frac{\sin(a t_p/2)}{a t_p/2} \frac{\sin(b t_p/2)}{b t_p/2}. \qquad (4.6)$$

Equation (4.5) describes the depth resolving power of our instrument and will be used to generate depth response curves which can be compared to those collected experimentally. Comparison of Equations (4.4) & (4.5) reveals that simulations involving DVMs employing square apertures are likely to be considerably more time-consuming than those for DVMs employing circular aperture arrays. This arises from the fact that spatial frequency response of the pinholes is no longer circularly symmetric and thus we cannot analytically integrate over ϕ in the innermost integration of Equation (4.5).

4.6   Comparison of square and circular apertures

Before proceeding with the experiment we digress for a moment to examine whether resolution is likely to be lost by the use of square (over the usual circular) apertures. We choose to examine the optical sectioning properties of area-matched square and circular apertures: a square aperture of width t_p is compared to a circular aperture of radius $v_p = \frac{t_p}{\sqrt{\pi}}$. Furthermore, we choose to fix the aperture spacing for both array types; this makes physical sense as it ensures an equal level of light throughput (an important order of merit) for both. Depth responses of some representative arrays are shown in Figure 4.4. Initially 2×2 arrays of various aperture sizes and spacings were
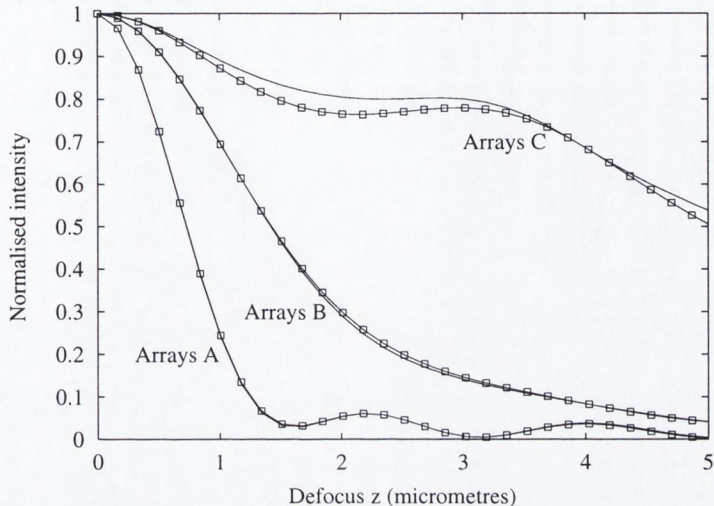
Figure 4.4: Comparison of the optical sectioning properties of arrays of square and circular apertures. The curves with boxes overlayed represent data for square apertures while the solid lines represent data for circular apertures. Array groups A, B, and C are described in the text.

examined because of their computational simplicity. We have introduced the notation $\overline{v}_p$ and $\overline{t}_p$ to denote the aperture radius (circular aperture) and aperture width (square aperture) expressed in real co-ordinates. Similarly $\overline{R}$ is defined as the aperture spacing in real co-ordinates.

- Array group A: $\overline{t}_p = 15\mu$m ; $\overline{v}_p = 8.46\mu$m and $\overline{R} = 120\mu$m.

- Array group B: $\overline{t}_p = 30\mu$m ; $\overline{v}_p = 16.92\mu$m and $\overline{R} = 60\mu$m.

- Array group C: $\overline{t}_p = 60\mu$m ; $\overline{v}_p = 33.85\mu$m and $\overline{R} = 30\mu$m.

We note from Figure 4.4 that, in the case of array groups A and B the aperture geometry has very little influence on the depth response. In the case of array group C however, there is a significant difference between the depth responses of the circular aperture and square aperture arrays; the circular aperture depth response exhibiting a higher background. We note that, of the three array groups, group C is the array with the most closely spaced apertures. The figure suggests that pinhole geometry has minimal

80

effect on the depth response unless closely spaced apertures are employed. Figures 4.5 and 4.6 appear to support this. Both figures depict theoretical depth responses for 5×5 aperture arrays employing both square ($t_p = 15\mu$m) and circular (8.46μm) apertures. Apertures in Figure 4.5 are spaced 45μm apart, while those of Figure 4.6 are spaced 120μm apart. Figure 4.6, which represents the more widely spaced apertures shows depth responses which are practically indistinguishable. On the other hand, in Figure 4.5 the more closely spaced apertures give rise to different depth responses for the square and circular apertures with sidelobes being less pronounced for square apertures. This is in contrast to the behaviour of incoherent source systems as reported by Fewer *et al.* [40], in which aperture geometry appears to have no influence on the depth response. Without performing an exhaustive study, we may contend that when closely spaced arrays are used, the sidelobes resulting from coherent crosstalk between square apertures are less significant than those resulting from circular apertures. As the aperture spacing is increased, the effect becomes less pronounced and aperture geometry becomes unimportant. This study suggests that the computationally more efficient equations describing the depth response of coherent source DVMs employing circular apertures could be used to describe the general trends of depth sectioning in DVMs employing square apertures. Also, it appears the use of square apertures in coherent source PAMs is not a disadvantage and indeed in some cases, may be advantageous.

4.7 Scanning aperture arrays

Before going any further it is useful to define the parameters which describe the dimensions of each aperture array. Figure 4.7 shows the aperture array configuration used, this particular example shows an array which requires four scan steps to fill the area of the SLM which was used. The 4 scan steps are repeated continuously so that quasi real-time confocal imaging is possible. The aperture array is defined by the following parameters: The individual aperture width/height t_p, the aperture separation R, the
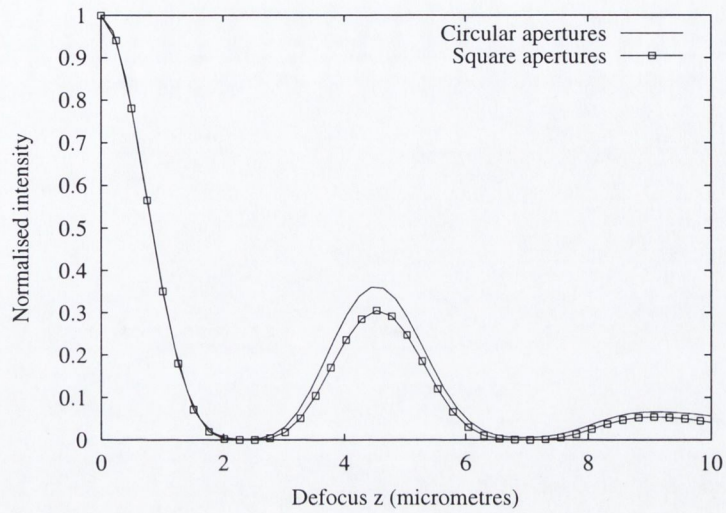
Figure 4.5: Comparison of the optical sectioning properties of 5 × 5 arrays of square and circular apertures. Solid line: depth responses of a square aperture array employing circular apertures of radius 8.46μm and spacing 45μm. Solid line with □s overlayed: depth response of a square aperture array employing square apertures of width 15μm and spacing 45μm
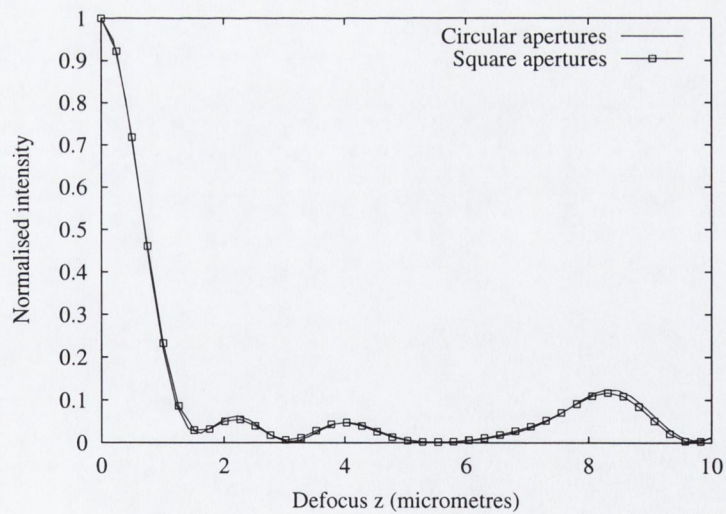
Figure 4.6: Comparison of the optical sectioning properties of 5 × 5 arrays of square and circular apertures. Solid line: depth response of a square aperture array employing circular apertures of radius 8.46μm and spacing 120μm. Solid line with □s overlayed: depth response of a square aperture array employing square apertures of width 15μm and spacing 120μm
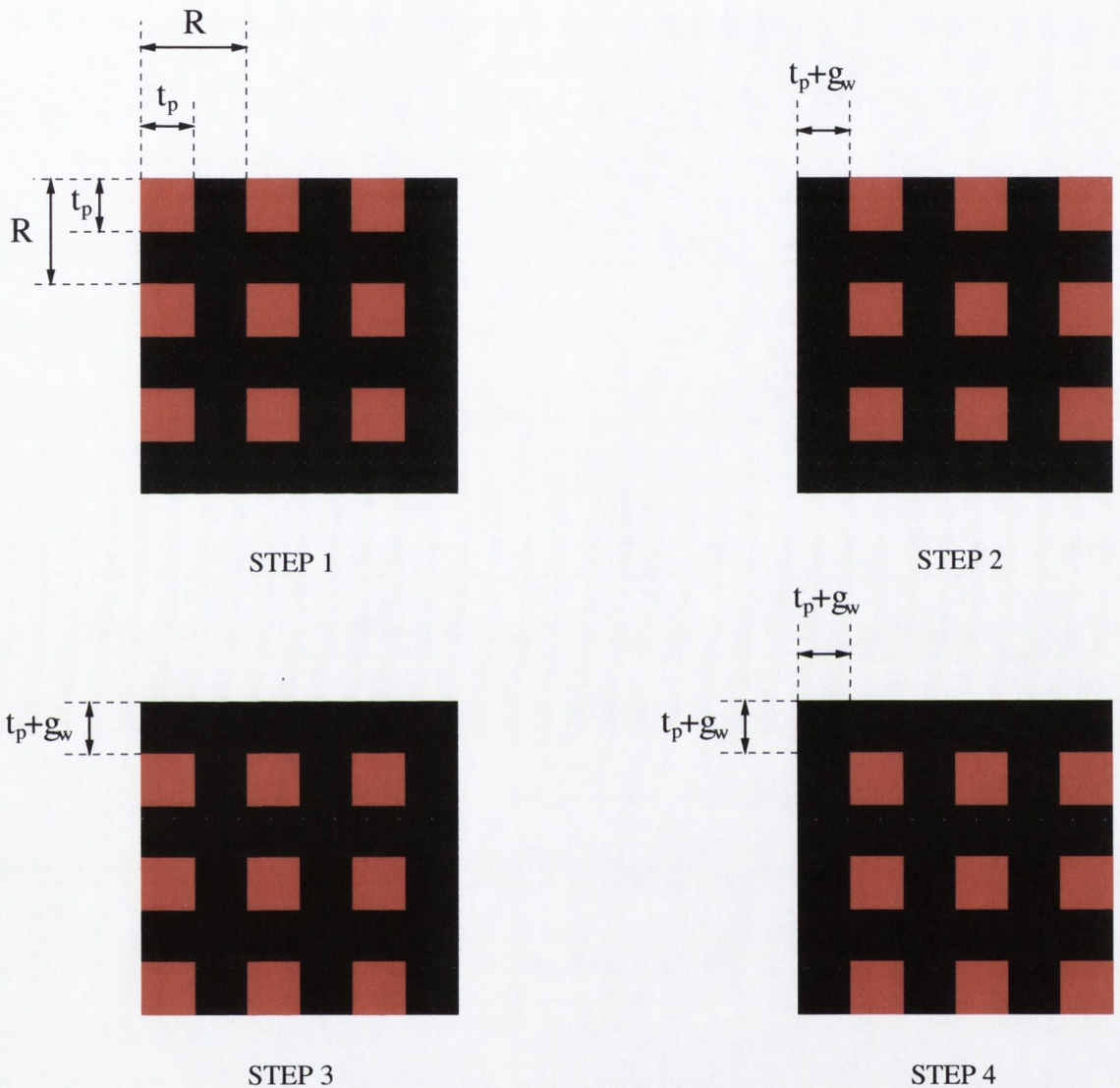
Figure 4.7: The complete scan cycle for a typical aperture array. The total scanned area on a complete scan cycle is indicated by the black bounding box. The individual aperture height/width is denoted t_p, while the aperture separation is denoted R. The scan step-size is $t_p + g_w$ where g_w is the gap width between pixels; in this case the the total number of scan steps (N_s) required to fill the used SLM area is 4, while the mark-space ratio ($m_s = \frac{R}{(t_p + g_w)}$) is 2.

scan step size, which in the case of arrays we examined was always equal to $t_p + g_w$ (where $g_w = 1\mu m$ is the gap width between pixels) thus ensuring that there was no overlap between successive scans. The total number of scan steps required to scan the whole SLM area is defined as N_s and we define the mark-space ratio as $m_s = \frac{R}{t_p}$.

4.8 System artifacts

Before continuing with the experiment we first introduce some important system artifacts which became evident, and describe their likely effects on our results.

4.8.1 Finite pixel contrast ratio

The fact that SLM pixels exhibit a finite contrast ratio may have some implications for recorded images. In what follows, we examine some possible implications.

If we consider the SLMs to be in perfect focus on the sample and consider any pixel within their active area, then during a complete scan cycle, the pixel will be switched 'ON' exactly once and 'OFF' exactly $(N_s - 1)$ times. Conversely, if we consider the SLMs to be completely defocused on the sample: we imagine light which has originated from apertures which were 'ON' is so defocused that it is comparable in intensity to light which has originated from 'OFF' pixels. In this case, any pixel can be considered to be 'OFF' exactly N_s times. In symbols, if the intensity due to an 'ON' pixel is written I_{ON} (I_{OFF} for 'OFF' pixels), then the in-focus intensity I_F can be written:

$$I_F \propto (N_s - 1)I_{OFF} + I_{ON}, \qquad (4.7)$$

while the out-of-focus or background intensity I_{NF} can be written:

$$I_{NF} \propto (N_s)I_{OFF}. \qquad (4.8)$$

From these two equations, we see that, in general for a system with a finite contrast

ratio, for good quality confocal behaviour we require N_s to be small as possible. Because N_s is related to the mark-space ratio of the array via $N_s = m_s^2$, this places a limit on the aperture spacing we can safely use without compromising confocality. In reality, this is not likely to be a practical issue with our particular SLM where the maximum number of frames which can be displayed by the SLM is the limiting factor. For, SLMs with slow modulation rates and low contrast ratio it could however become a limiting factor.

4.8.2   Inverse frame leakage

With the system carefully aligned, depth responses were recorded for various aperture arrays. The curves taken indicated the presence of a higher than expected background in all of the depth responses. This enhanced background effect could not be fully explained by the finite contrast ratio of the SLM pixels and its cause proved to be quite elusive but was eventually traced to the inefficient operation of the LC shutter. In order to demonstrate the limitations of the shuttering system, the CCD camera was replaced by a PM tube, the signal from which was displayed on a digital oscilloscope. Comparison of the PM tube signal with various reference signals revealed the problem to be leakage of inverse frames through the shutter. The effect is illustrated by Figure 4.8.

In the figure, we compare two signals: the first is the Image Valid output coming from the 'SLiM driver' module, which, as described previously, is high whenever the current frame has been successfully displayed on the current SLM. The space between each successive 'high' represents the time taken to transfer the current frame from the hardware module to the SLM. The sequence in which the frames are loaded onto the SLMs is superimposed on the trace. From left to right: (with shutter closed) the inverse of the current frame is loaded onto SLM 1, the inverse of the current frame is loaded onto SLM 2, the proper frame is loaded onto SLM 1, the proper frame is loaded onto SLM 2, the shutter opens, the shutter closes and the cycle continues . . . .
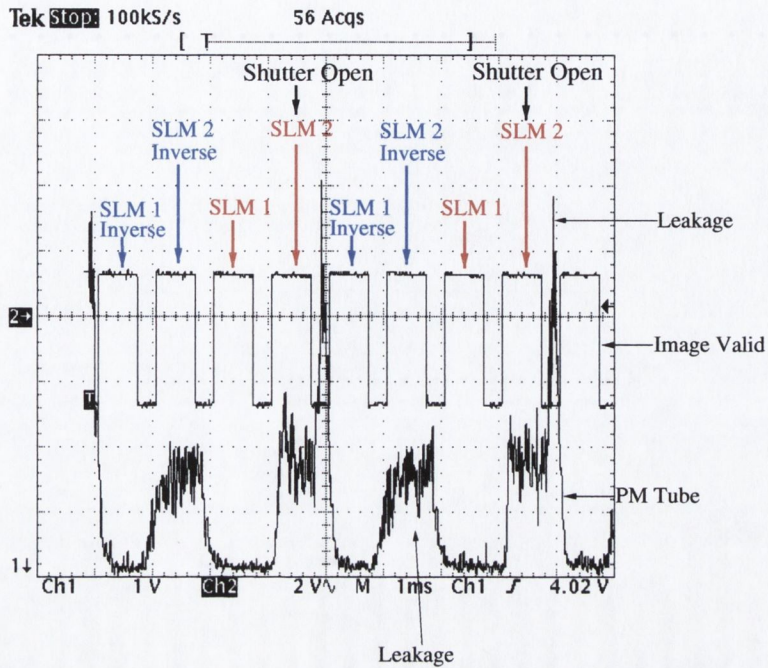
Figure 4.8: Image Valid signal and signal from PM tube as recorded on a digital oscilloscope.

In the case of a confocal-type frame, as shown in Figure 4.9, the proper frame is a frame in which very few of the SLM pixels are switched 'ON' whereas the inverse frame contains many SLM pixels which are 'ON'. Therefore the light coming from an inverse frame carries considerably more intensity, in general, than the light coming from a proper frame. This means it is desirable that all light from inverse frames is successfully excluded. Looking again at the figure, the signal from the PM tube reveals the presence of unwanted light. In an ideal system, light should only fall on the PM tube at the instant the shutter opens and should cease at the instant the shutter closes. Figure 4.8 shows the arrival at the PM tube of a considerable amount of light when inverse frames were present on both SLMs. We corrected for this effect by using a mechanical chopper in conjunction with the LC shutter and the combination of the two was found to exclude this problematic light completely.

The LC shutter also has the disadvantage of having a large capacitance which must be fully charged/discharged before the shutter opens/closes; the process was found

86
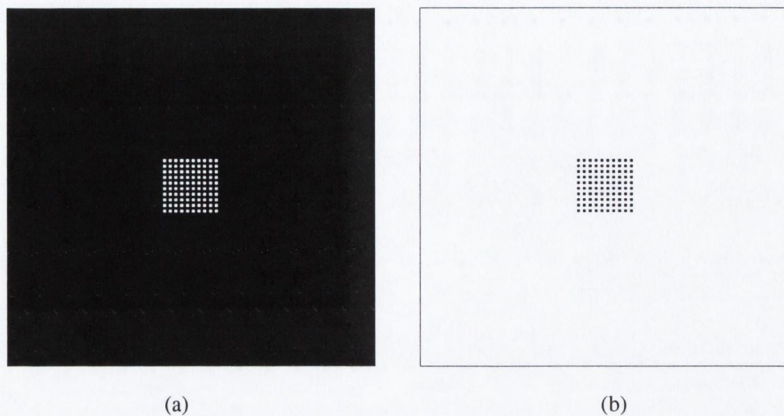
Figure 4.9: (a) Typical confocal aperture array. (b) Typical confocal 'inverse frame'.

to require $\sim 60\mu$sec. The effect of this can be seen in Figure 4.8: (the shutter open signal occurs every fourth time image valid goes high) witness the time lag between the shutter open and the increase in light intensity at the PM tube. The same time-lag can be seen when the shutter close signal arrives; because of this delay there is a large spike present in the PM tube signal. This spike was due to the overlap of the inverse frame from SLM 1 on the proper frame of SLM 2; the height of the spike was sensitive to defocus and was found to account for the slanted background and other effects which we witnessed in all our experimental data.

An example of the slanted background we encountered is depicted by Figure 4.10. Part (a) of the figure shows depth responses for two aperture arrays which cover equal areas of the SLMs. The 20×20 array (Array A) exhibits a lower background level than that of the 10×10 array (Array B); this is despite the fact that it contains apertures more closely spaced together $(\overline{R} = 60\mu$m) than the 10×10 array $(\overline{R} = 120\mu$m), and obviously a larger number of apertures between which 'background increasing' crosstalk can occur. The cause of the effect was found to be leakage of the inverse frame through the LC shutter as described above. In the case of the 10×10 array, the inverse frame contains more 'ON' pixels than that of the 20×20 array, and so a higher background is present in the depth response. In the case of Figure 4.10 (b), we see two arrays with
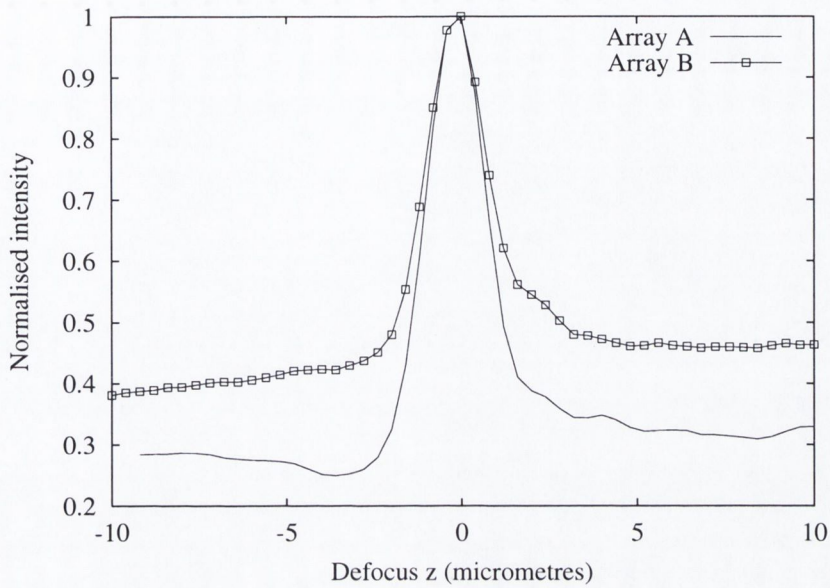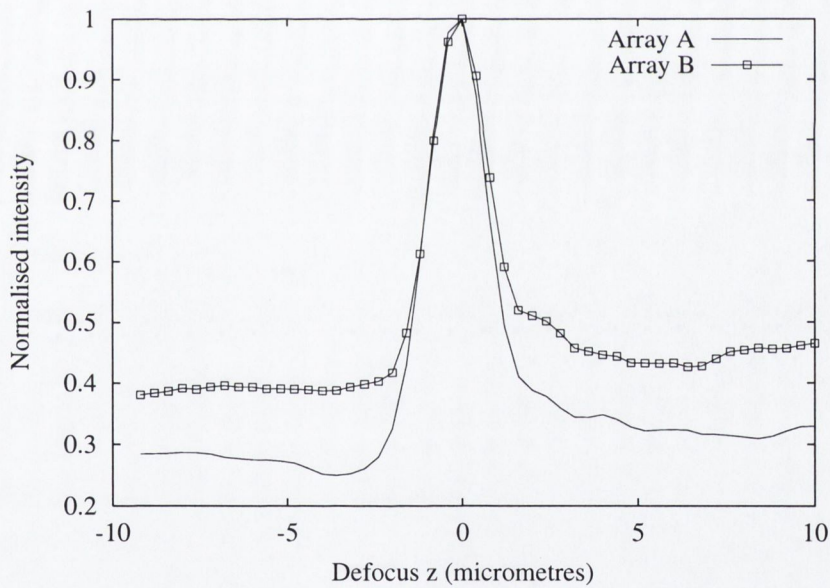
Figure 4.10: Enhanced depth response backgrounds encountered. (a) Array A represents the depth response of a 20×20 array with aperture width $\bar{t}_p = 14\mu$m and mark-space ratio $\overline{R} = 60\mu$m; Array B represents the depth response of a 10×10 array with aperture width $\bar{t}_p = 14\mu$m and mark-space ratio $\overline{R} = 120\mu$m. (b) Array A represents the depth response of a 20×20 array with aperture width $\bar{t}_p = 14\mu$m and mark-space ratio $\overline{R} = 60\mu$m; Array B represents the depth response of a 10×10 array with aperture width $\bar{t}_p = 14\mu$m and mark-space ratio $\overline{R} = 60\mu$m.

the same mark-space ratio exhibiting different backgrounds. The effect again appears counter-intuitive, with the array containing a greater number of apertures (Array A) having the smaller background. The effect is due to fact that the 20×20 array (Array A) contains more 'ON' pixels than the 10×10 array (Array B), so that its inverse contains less 'ON' pixels than that of the 10×10 array. In an efficient system, the LC shutter should be replaced by a more efficient shuttering device such as an acousto-optic modulator.

4.9   Experimental results

We give an overview of some of the experimental investigations which have been performed to evaluate the optical sectioning in confocal microscopes. We then move on to show more examples of recorded depth responses, in all cases we choose to subtract the background levels from the depth responses so that they can be more easily compared.

4.9.1   Precedence

Over the years, numerous experiments have been performed in order to verify the predictions of scalar diffraction theory with regard to brightfield confocal microscopy. For example, Wilson and Carlini [57] recorded depth responses for single pinhole confocal microscopes employing a wide range of detector pinhole radii. Their results suggested that the difference between experimental and theoretical depth responses increased as the detector pinhole radius was increased. The reason for the difference was ascribed to high angle effects and shading of the lens pupil across its width due to Fresnel losses. The authors suggest that the pupil shading would decrease the effective NA of the objective lens; by observing the point in experimental curves where the first zero occurs and, noting the fact that $u = 2\pi$ at this point, they were able to arrive at a figure for the effective NA of the objective lens (via Equation (2.16)) which gave better agreement between experiment and theory. The disparity still existed at larger detector pinhole radii; this was proposed to be perhaps a result of spherical aberration

which was suggested to be more significant at higher detector pinhole radii. This latter assertion was verified in a follow-up paper a short time later [74].

In terms of direct-view microscope-like systems, Xiao *et al.* [22] performed experimental depth response measurements in a DVM employing a spinning Nipkow-disc microscope and recorded a depth response which was broadened by $\sim 40\%$ relative to that expected. However, the use of an approximate expression, neglecting multi-aperture effects and finite aperture size means we cannot draw strict conclusions from this. Some years later, Fewer *et al.* [40] verified a theory for an incoherent source DVM employing a finite number of apertures of finite size: agreement was excellent for small apertures sizes. The divergence from theory at large aperture radii was accounted for in a similar way to that of Wilson *et al.* [57]. Drawing on the work of Matthews *et al.* [75] who experimentally measured the transmission of an objective lens across its width and showed it to drop off substantially with distance from the centre of the lens. Matthews' result was integrated into the equations and partially accounted for discrepancies between theory and experiment at large aperture sizes.

The same year, Liang *et al.* [67] performed the first depth response measurements in a coherent source PAM system. Using a simple expression for the theoretical depth resolution (which neglected multi-aperture effects and finite aperture size) good agreement was demonstrated between theory and experiment with the experimental FWHM sometimes being less than that predicted by theory. Due to an effective tilt across the DMD source/detector array relative to the laser source used, the system cannot be directly compared to our present one. Finally, in 1998 Fewer *et al.* [62] performed a study of coherent source brightfield DVMs. The conclusions were that the depth responses recorded were highly sensitive to the alignment of the aperture array. The recorded sidelobes were $\sim 58\%$ smaller than those predicted by the theory, the difference being attributed to a combination of lens aberrations, pupil shading and the fact that the theory assumes a relative phase difference of zero between every pinhole in the array.

4.9.2 Experimental depth responses

In general, our recorded depth responses differed considerably from those predicted by theory: in large part, we put this difference down to the influence of inverse frame leakage. Nevertheless, we compare experimental and theoretical depth responses and make some general comments about the system.

Non-repeatability

The actual depth responses themselves were found to be highly dependent on the alignment of the system which is not surprising considering its coherent nature. As a particular example of this behaviour, Figure 4.11 (a) shows two experimental depth response curves, recorded after complete re-alignment of the system on two separate occasions, for 10×10 arrays of square apertures with $\bar{t}_p = 14\mu$m (single SLM pixel)and an aperture spacing $\overline{R} = 30\mu$m. Part (b) of the figure depicts the theoretically predicted depth response for this array. The experimental data sets are labelled as 'Run 1' and 'Run 2'. Comparison of Run 2 in Figure 4.11 (a) with the theoretical data shows that this set of data has a FWHM similar to what is theoretically predicted. The sidelobes occur where they are expected to but their relative heights are different. It appears every second sidelobe has been suppressed, we also see a marked asymmetry in the experimental depth response with sidelobes to the left of the main peak being greater than those to the right. Run 1 of Figure 4.11 (a), by comparison, shows a broadened FWHM which appears to result from the total suppression of every second sidelobe. Because of the defocus dependent inverse frame leakage mentioned earlier it is difficult to make definite statements about the sidelobe suppression and how exactly it occurs: it may well be that the sidelobes are perturbed by precisely this effect.

Aberration effects

In addition to inverse frame leakage there are a number of other possible reasons for the difference between theory and experiment. Firstly the theory assumes a perfect plane
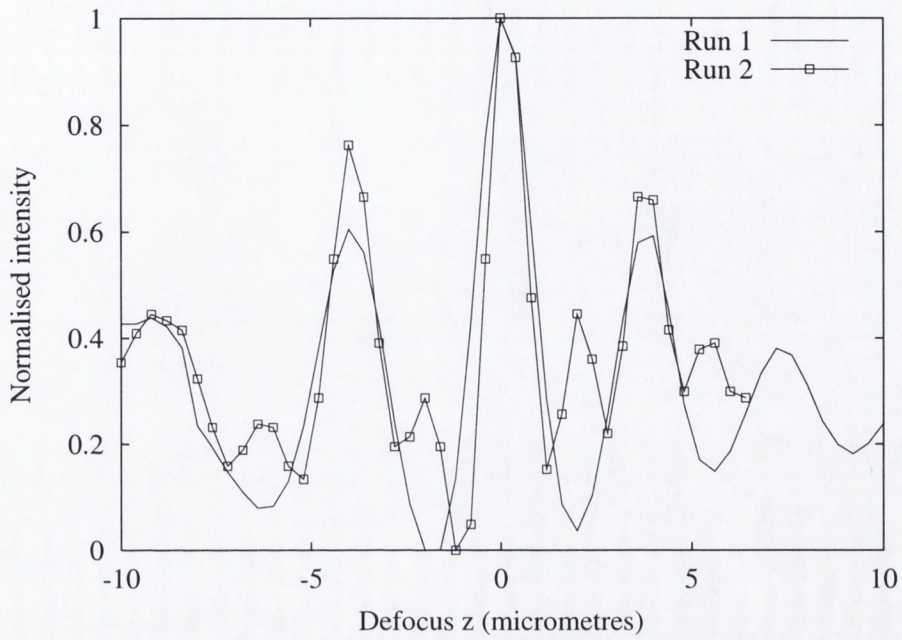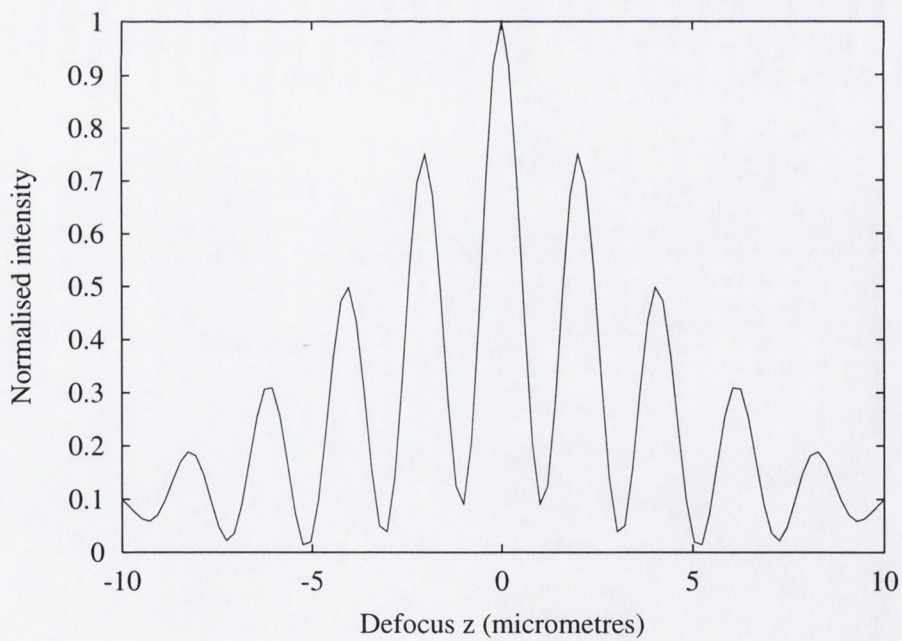
Figure 4.11: Depth responses of 10×10 arrays of square apertures with $\bar{t}_p = 14\mu$m and $\overline{R} = 30\mu$m. (a) Two experimental depth responses recorded on separate occasions; (b) Theoretical depth response.
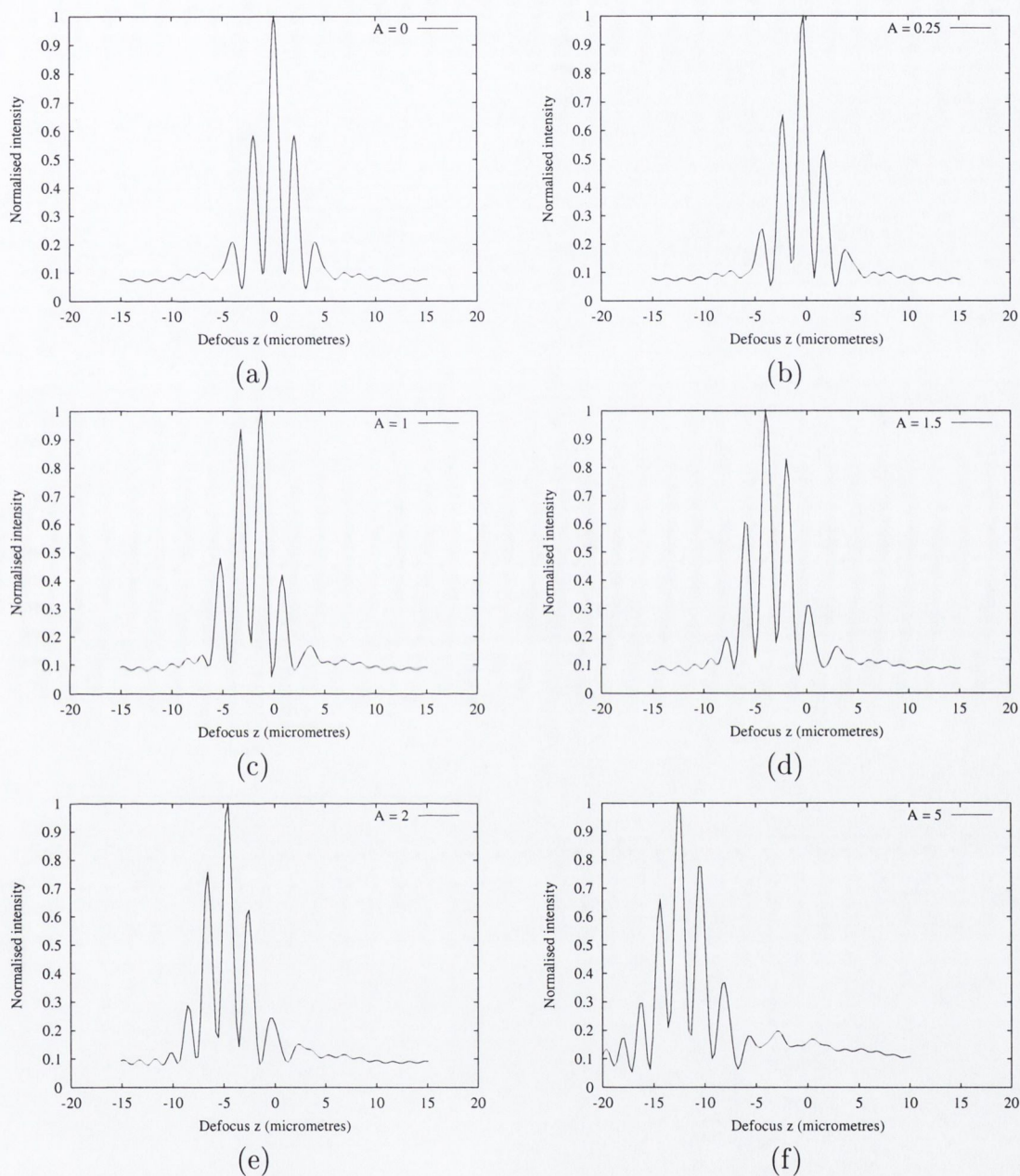
Figure 4.12: Theoretical depth responses of a 5×5 array of square apertures with $\bar{t}_p = 14\mu$m and $m_s = 2$ showing the effect of various amounts of spherical aberration (represented by A). Note the asymmetric sidelobes when spherical aberration is present. Between parts (c) & (d) of the figure, the roles of the main maximum and the first sidelobe are reversed.

wave source and perfect SLM alignment so that the relative phase difference between any pair of source/detector apertures is zero. In practice this could not be the case especially when two separate SLMs are used. We also remind ourselves that our theory was a scalar one which neglected the light polarisation and the manner in which it is perturbed at the interface between air and each optical element. Finally, we suspect the presence of considerable spherical aberration in our system with two main sources of this.

Firstly, any difference between the optical properties of the two 10cm lenses (such as small differences in their focal lengths) would cause the objective lens to be operating at the incorrect tube length with respect to one or both of them with the aberrations that brings (primarily spherical aberration [43](P. 113)). Secondly, the placement of polarisers and a number of beamsplitters in the light path further introduces refraction-induced spherical aberration, see for example Corle and Kino [7].

In an attempt to model the effects of spherical aberration on the system, we follow Wilson *et al.* [74] and define an aberrated Pupil function, which includes the influence of spherical aberration as:

$$
P(u, \rho) = \begin{cases} \exp(-j\left[\frac{1}{2}u\rho^2 + 2\pi A\rho^4\right]), & |\rho| \leq 1 \\ 0, & \text{otherwise.} \end{cases} \tag{4.9}
$$

With the co-efficient A representing the amount of spherical aberration present in the system. Using a 5×5 array of circular apertures of $\bar{v}_p = 7.5\mu m$ and $m_s = 2$ as an illustrative example, we modelled depth responses for various levels of spherical aberration. The results are shown in Figure 4.12. The general effect of increasing the amount of spherical aberration is seen to be a shift in the position of the main peak towards negative defocus (for positive values of A). The depth responses are also seen to become asymmetrical. Between $A = 1$ and $A = 1.5$ (parts (c) & (d) of the figure) the first sidelobe and main peak change roles. Throughout, the FWHMs of the depth responses do not appear to change significantly and the sidelobes remain prominent.

94

Comparison of the data in Figure 4.12 with our experimental data tends to suggest that, although spherical aberration was present in our system (witness the asymmetry), the amount was relatively small and can not explain the sidelobe depression and FWHM broadening we have seen.

Another effect which could affect experimental depth responses considerably is pupil shading or apodization. Pupil shading can be thought of in a rather approximate way as causing a reduction in the effective NA of the objective lens. We thus modelled our experimental situation for a variety of values of effective NA. The results suggested that pupil shading cannot account for the behaviour we have witnessed. We thus contend that it is most likely that the departure we have seen from expected behaviour is largely due to the effect of inverse frame leakage. We may be able to gain more insight into this process by examination of aperture arrays of various dimensions. We first examine the effect of the number of apertures on the experimental depth response.

Influence of the number of apertures, N

Further insight into the behaviour of the system can be achieved by observing how the optical sectioning changes as larger number of apertures are used. Our investigations from Chapter 5 will show that, in general, increasing the number of apertures should simply increase the heights of the sidelobes without, in general, perturbing the point where they occur. We thus present Figure 4.13: this figure contains data taken on the same occasions as Runs 1 & 2 from Figure 4.11; with the number of apertures increased to 30×30. Part (a) of the figure shows 10×10 & 30×30 data from Run 1 while part (b) contains corresponding data from Run 2. Looking first at part (b) of the figure, the data broadly follows the behaviour we expect. The behaviour is particularly good to the right of the main peak: sidelobes remain in the same position but are increased in height in the case of the 30×30 array due to the larger number of apertures partaking in the coherent crosstalk. The sidelobes have begun to approach the level of the main peak which is the behaviour we might expect for such a relatively large number of apertures. The FWHM of the curve also remains similar to that of the 10×10 array.
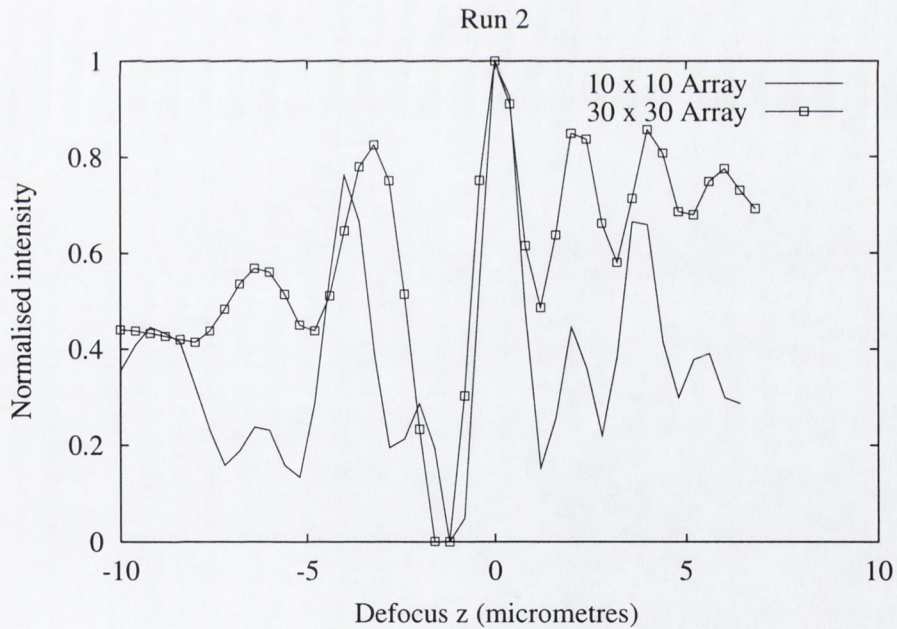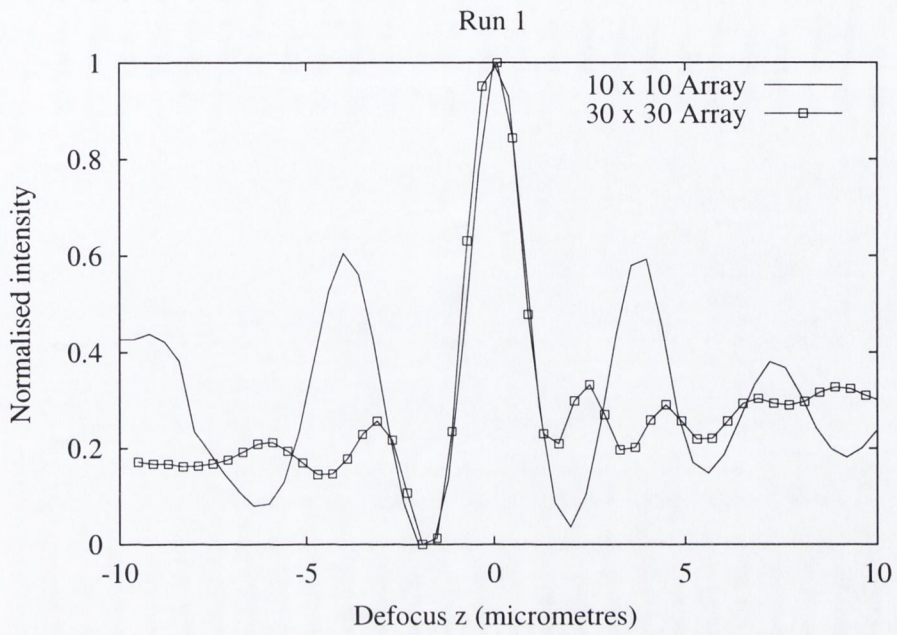
Figure 4.13: Experimental depth responses of 10×10 and 30×30 arrays of square apertures with $\bar{t}_p = 14\mu$m and $\overline{R} = 30\mu$m. (a) Both curves recorded with identical set-up; data designated as Run 1. (b) Both curves recorded with identical set-up; data designated as Run 2.

To the left of the main peak, the behaviour is slightly more unpredictable. In the case of part (a) of the figure, the data does not follow the expected behaviour: the position of all sidelobes has changed between the 10×10 and 30×30 arrays and their relative heights do not approach the levels of the main peak as we might have expected. In fact the sidelobes appear to have reverted to the correct axial positions. This behaviour would support our contention that inverse frame leakage is the major factor affecting the character of the experimental depth responses: the 30×30 array has a much less significant inverse frame than the 10×10 array and thus the sidelobes are allowed to retain the proper positions. On comparison of parts (a) & (b) of the figure it is evident that slight mis-alignments or aberrations in the system, along with the inverse frame leakage, can cause the general trends of behaviour of the system to change considerably.

Influence of the aperture spacing, R

We now introduce some more recorded depth responses. Figure 4.14 shows both experimental and theoretical depth responses for 10×10 arrays of apertures with $\bar{t}_p = 14 \mu m$ and $\overline{R} = 30 \mu m$, $45 \mu m$, & $60 \mu m$. Again, we see discrepancies between theory and experiment: the sidelobes do not follow the predicted behaviour. In the case of the $\overline{R} = 45 \mu m$ array, we again see the apparent depression of every second sidelobe, while in the case of the $\overline{R} = 60 \mu m$ the sidelobes appear much reduced to those predicted with the main sidelobe from the theoretical prediction being totally absent. Examination of the FWHMs of parts (a) indicates the presence of some additional behaviour which is perhaps unexpected. The FWHM of the most closely spaced array exceeds that of both other arrays, while the FWHM of the $\overline{R} = 60 \mu m$ array is less than that of the $\overline{R} = 45 \mu m$ array. This behaviour was also predicted by theory and is indicative of the complex nature of coherent source DVM optical sectioning. Further examples of recorded depth responses are shown in Figure 4.15. The depth responses were recorded for 10×10 arrays of apertures of width $14 \mu m$ with aperture spacings of $90 \mu m$, & $120 \mu m$. In the case of these arrays no sidelobes were present in the depth responses, which appear to
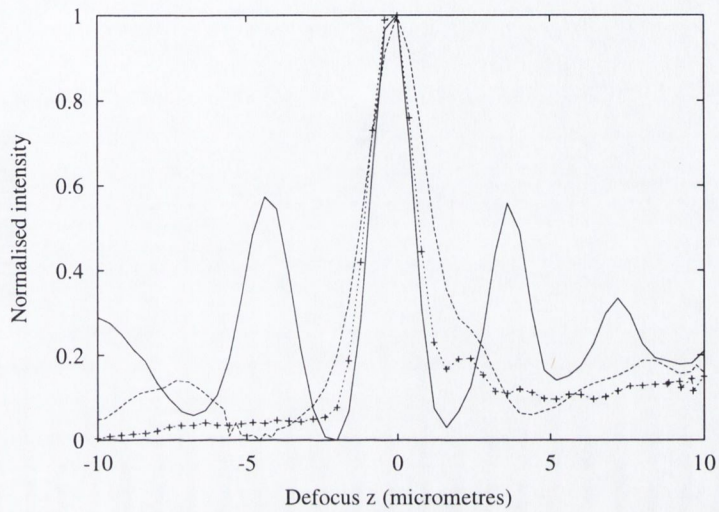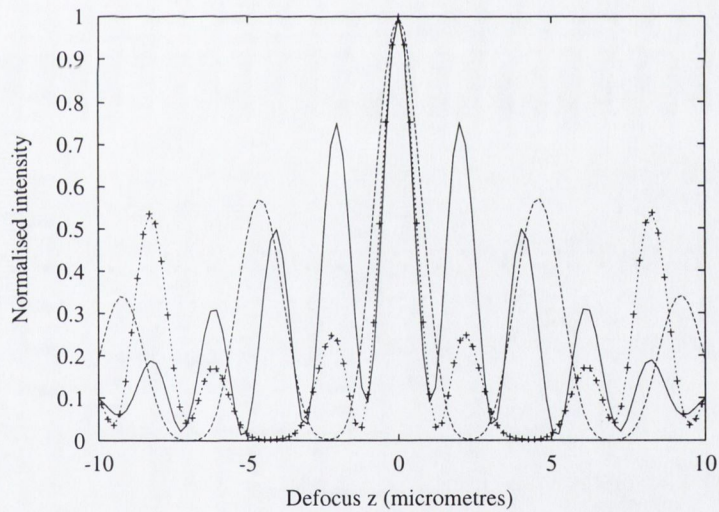
Figure 4.14: Depth responses for 10×10 arrays of square apertures with $\bar{t}_p = 14\mu$m and $\overline{R} = 30\mu$m (solid line), 45μm (dashed line), & 60μm (dashed line with '+'s overlayed). (a) Experimental; (b)Theoretical.

represent reasonable optical sectioning. The lack of sidelobes in the depth responses of the more widely spaced arrays again tends to support our contention that the inverse frame leakage is the dominant factor affected the sidelobes. Again, because the inverse frame has a more significant role in the case of widely spaced arrays.
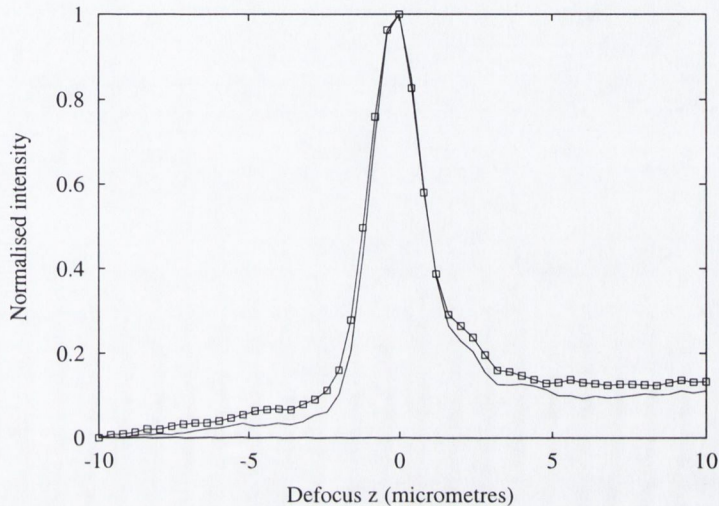
Figure 4.15: Experimental depth responses for 10×10 arrays of square apertures with $\bar{t}_p = 14\mu$m and $\overline{R} = 90\mu$m (solid line), & 120μm (solid line with '□'s overlayed).

4.10 Recorded images

Despite the problems with the system, it was possible to take good quality confocal images. For example, Figure 4.16 shows images of a semiconductor laser sample taken with a 30×30 array of apertures of side 14μm with spacing of 60μm. Parts (a) and (b) of the figure represent confocal images taken 1.6μm apart; part (c) represents the conventional microscope image. The confocal images show the sample to consist of two parallel trenches etched in a piece of bulk semiconductor, with an un-etched space between them. The field of view is $72 \times 72\mu$m.
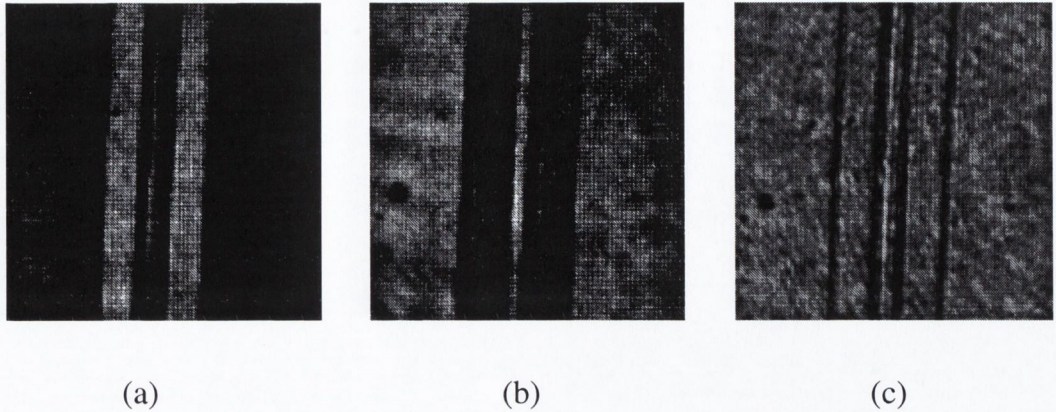
Figure 4.16: Images of a semiconductor laser: (a) Confocal image taken with a 30×30 array of apertures of side 14μm with spacing of 60μm. (b) As (a) but taken at different axial position. (c) Conventional image.

4.11 Aperture correlation

In a DVM, the choice of the dimensions of the aperture array is crucial. The size of the individual apertures determines the absolute resolution available and the number of apertures in the array can affect the sidelobe level in the depth response as well as its FWHM [25]. The spacing between apertures affects the amount of crosstalk between apertures; again this can result in increased side-lobes and broader FWHMs. Ideally we wish to employ an aperture array which emulates the single pinhole confocal microscope as closely as possible. Small, well spaced apertures give good performance while having the disadvantage of low light throughput. Aperture correlation, as first described by Wilson and co-workers [28, 29] provides an improvement on this.

Essentially, each aperture in the array is modulated in a pseudo-random fashion so that, in a time-averaged sense, neighbouring apertures are uncorrelated and the cross-talk between them reduced. This means that apertures can be placed much closer together without suffering the negative drawbacks of high cross-talk; a high light throughput is maintained without compromising the imaging. The scheme requires that the transmittances of the apertures should vary randomly between values of -1 and 1; because, optically, transmittances of -1 are not realisable, the transmittance is

100

instead modulated between 0 and 1. This means that images taken, instead of being wholly confocal, are the sum of a confocal and a conventional image [28]; a conventional image being one which is taken when all pixels on the SLMs are switched on. In effect, a DC offset is added to the depth response. Thus, in order to obtain a pure confocal image, subtraction of a pure conventional image from the aperture correlated image must be performed.

4.11.1   Implementation

As shown by Wilson *et al.* [28], if we define the time (t) sequence of aperture openings and closings of aperture i, j as $b_{i,j}(t)$, and if the following two conditions are satisfied:

$$< b_i(t)b_j(t) >= \begin{cases} 1 & i = j \\ 0.5 & i \neq j \end{cases} \tag{4.10}$$

and:

$$< b_i(t) >= 0.5 \tag{4.11}$$

with the notation $<>$ taken to mean a time average. Then, in the limit as the apertures are adjacent to each other with no dead space between them, captured images represent the sum between a confocal image and a conventional image. Examples of sequences which fulfil these conditions are given as an infinite sequence of random 0s and 1s, or finite-length complementary Golay codes [76] with an added offset.

Golay codes can be related to Hadamard matrices [77, 78]: the Hadamard matrix of order $K = 2^m$ can be generated by starting with the Kernel matrix:

$$\mathbf{H}(1) = \begin{bmatrix} +1 & +1 \\ +1 & -1 \end{bmatrix} \tag{4.12}$$

and applying the recursion relation:

$$\mathbf{H}(m+1) = \begin{bmatrix} \mathbf{H}(m) & \mathbf{H}(m) \\ \mathbf{H}(m) & -\mathbf{H}(m) \end{bmatrix} \quad (4.13)$$

For example, $\mathbf{H}(2)$ can be written:

$$\mathbf{H}(2) = \begin{bmatrix} +1 & +1 & +1 & +1 \\ +1 & -1 & +1 & -1 \\ +1 & +1 & -1 & -1 \\ +1 & -1 & -1 & +1 \end{bmatrix} \quad (4.14)$$

The primary Golay code is retrieved by taking the first two elements on row 1 of the matrix followed by the next two elements of the second row *etc.* In the case of $\mathbf{H}(2)$, the primary Golay code is $\{+1, +1, +1, -1\}$. 4 further Golay sequences can be extracted from the Hadamard matrix simply by multiplying the primary code by every row of the matrix (one of these is identical to the primary code). In general, we have K unique codes per Hadamard matrix of order $m = \log_2 K$.

The aperture correlation scheme is implemented by extracting the Golay codes of required length and transforming them from codes containing $+1$s and -1s to codes containing $+1$s and 0s simply be adding $+1$ and dividing by 2. Thus each $+1$ in the above continues to represent $+1$ while each -1 now represents 0. The codes now satisfy the condition described by Equation (4.10), in order to satisfy the condition described by Equation (4.11) we follow Juškaitis *et al.* [29] and concatenate each code onto its complement; the thus formed codes are now of length $2K$. We choose a block of pixels or 'super-pixel' on the SLM within which the apertures are to be uncorrelated. Each pixel within the super-pixel is programmed with one of the set of K Golay codes, because each code is of length $2K$, as described above, each pixel must be modulated $2K$ times. Thus the super-pixel may contain at most K pixels and we require the display of $2K$ frames in sequence onto the SLMs. In order to increase the field of view

of the system the super-pixel can be tiled across the SLM; within each tiled super-pixel every pixel has the desired correlation properties with respect to every other pixel but between super-pixels we can expect crosstalk to occur. Thus, for minimal crosstalk we require the super-pixels and thus the code lengths, K, to be as large as possible. This in turn dictates that the number of frames needed in the sequence $(2K)$ may become very large which means we are effectively limited by the modulation speed of the devices used. As a practical example of the implementation, Figure 4.17 shows Golay codes of length 4 being applied to the problem. In this example, Golay codes

Starting with the 4 Golay codes retrieved from H(2)
$$\{1,1,1,0\},\{1,0,1,1\},\{1,1,0,1\},\{1,0,0,0\}$$
Each is concatenated with its complement to form:
$$b_1=1,1,1,0;0,0,0,1$$
$$b_2=1,0,1,1;0,1,0,0$$
$$b_3=1,1,0,1;0,0,1,0$$
$$b_4=1,0,0,0;0,1,1,1$$
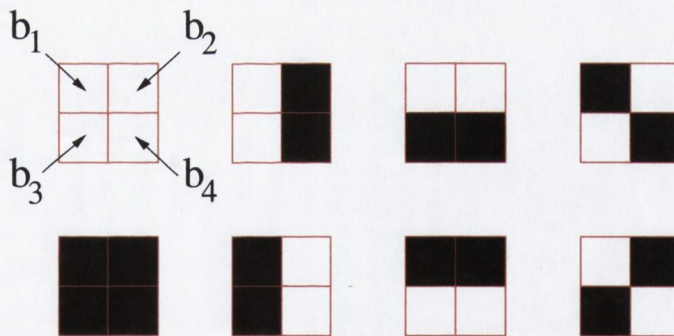
Switching sequence for a 2x2 pixel area on the SLM
For time averaging, CCD camera is synchronised to this cycle.

Figure 4.17: Sample implementation of aperture correlation scheme using Golay codes of length 4.

of length 4 are extracted from **H**(2) and concatenated onto their complements. The

resulting sequence lengths are 8, implying that a series of 8 frames must be continuously applied to the SLMs. By synchronising the CCD camera to this cycle or a multiple of it, we can ensure the desired time-averaging. In this case the super-pixels cover 2×2 SLM pixels and can be tiled across the SLM in order to increase the field of view. It is interesting to note from the figure that every frame within the sequence also contains its complement or 'inverse frame'. Thus, FLC SLM devices are well suited to this implementation; because the order in which the frames are displayed is irrelevant from a time average point of view, each frame and its inverse can be displayed in turn. The imaging rate of the system can be improved by a factor of two compared to our previously described system employing normal scanned confocal arrays.

4.11.2   Depth response behaviour

Depth responses were recorded using the aperture correlated implementation. The behaviour witnessed followed the expected trends with crosstalk occurring between the tiles on the SLM in an analogous way to crosstalk in normal scanned arrays. As a particular example, in Figure 4.18 depth responses (with backgrounds intact) of an aperture correlated array of 10×10 tiles; each tile consisting of 2×2 SLM pixels is compared with a normal 10×10 array of single pixel apertures each with an aperture spacing of $\overline{R} = 30\mu m$. Evidently, crosstalk occurs in the same manner between tiles in the aperture correlated array as between adjacent apertures in the normal array. The sidelobes occur at the same defocus positions in both cases, with the depth response of the aperture correlated array exhibiting a higher background level as expected.

4.11.3   Recorded images

A sample of some images recorded using the aperture correlation scheme are shown in Figure 4.19. Parts (a) and (b) depict partially confocal images taken at different axial positions while part (c) depicts the conventional image. Note the evidence of optical sectioning in parts (a) and (b): in part (a) the almost-vertical parallel trenches
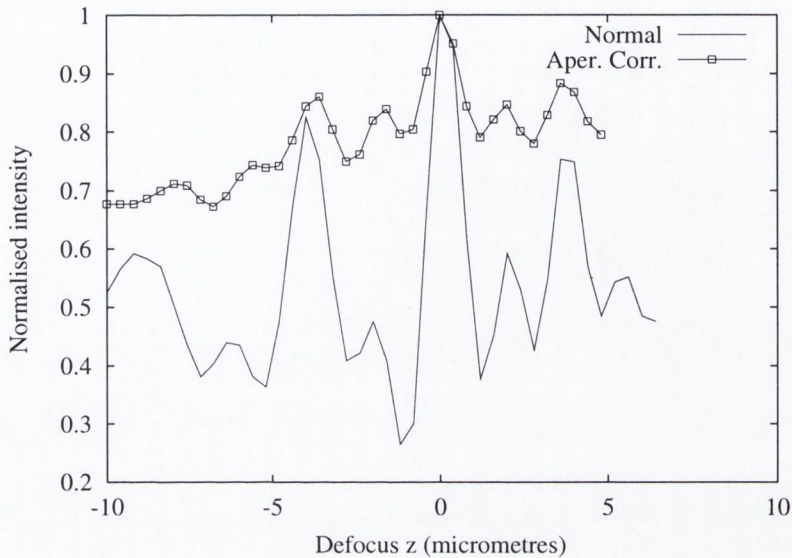
Figure 4.18: Comparison of the depth responses of equally dimensioned aperture correlated and standard confocal arrays. Note the fact that sidelobes occur at the same places in both cases.

appear brighter than the rest of the image indicating that these features are in focus. We note that not all the out-of-focus light is rejected from the image but appears as a reduced intensity background. This could in principle be rejected by subtraction of an appropriately scaled conventional image. Part (b) of the figure shows the bulk of the sample to be in focus, with the etched trenches being diminished in intensity. As with Figure 4.16, the two confocal images were taken 1.6μm apart. The images in Figure 4.19 show a much improved brightness from the purely confocal ones of Figure 4.16 due to the fact that, on average the throughput of both SLMs is much higher in the aperture correlation set-up.

4.12   Conclusions

We have performed an experimental study of optical sectioning in coherent source direct-view microscopy using a PAM employing 2 ferroelectric liquid crystal spatial
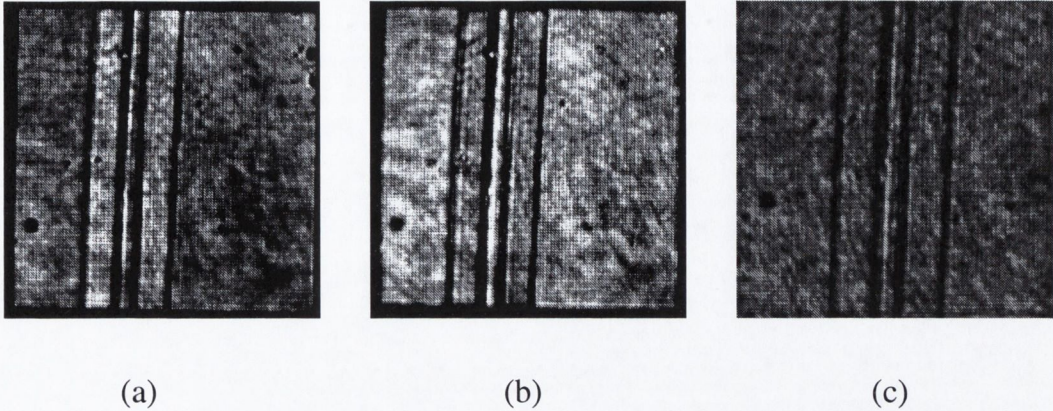
Figure 4.19: Images of a semiconductor laser: (a) Partially confocal image taken with an aperture correlated array consisting of 10×10 tiled super-pixels. Each super-pixel consisted of and 8×8 block of SLM pixels. (b) As (a) but taken at different axial position. (c) Conventional image.

light modulators. Before preceeding with the experiment we presented equations describing the depth responses of a coherent source brightfield DVM employing a finite number of square apertures of finite size. Comparison of DVMs employing square vs. circular apertures was first performed with both aperture types appearing to have similar imaging properties provided the aperture spacing was sufficiently large. At small aperture spacing the use of square apertures gave rise to sidelobes in the depth response which were smaller than those of equivalent circular aperture DVMs. This behaviour is in contrast to that of an incoherent source brightfield DVM as described by Fewer *et al.* [40] where the aperture geometry was found to have no significant effect on the depth response. These findings suggest that the computational less intensive equations describing optical sectioning in DVMs employing circular apertures could be used to model the behaviour of practical DVMs employing square apertures which are typically spaced at 10 times their radius.

We next moved on to introduce the experimental set-up along with some system artifacts which came to light. The most prominent of these was a leakage of the inverse frame through the shuttering system due to its inefficient operation. The effect

106

of the inverse frame leakage was seen to be a perturbation of the sidelobes of the depth response along with the superposition of a heightened and sloping background level. The depth responses themselves were found to be extremely sensitive to the alignment of the system, with the sidelobes and FWHM of the depth response in particular being easily disturbed. An examination of the effect of the number of apertures on the depth response was found to follow the predicted trends (see Chapter 5) but was again highly alignment dependent. The effect of aperture spacing on the depth response was also examined: the sidelobe behaviour was unpredictable but the FWHM varied as predicted. The effect appeared to be counter-intuitive and is discussed further in Chapter 5. Recorded images showed good-quality confocal behaviour.

Finally, an aperture correlation scheme was implemented using Golay code sequences and shown to be particularly well-suited to the FLC devices used. Super-pixels within which SLM pixels were uncorrelated were tiled across the width of the SLM, as expected crosstalk was seen to occur between adjacent tiles which was analogous to crosstalk in similarly dimensioned confocal arrays. Recorded images showed clear confocal behaviour with the expected superposition of out-of-focus or background light.

Chapter 5

Source coherence in brightfield direct-view microscopy

Laser sources offer a possible solution to the problem of low light throughput in direct-view microscopes (DVMs). However, coherent source DVMs have been shown to suffer from problems such as increased sidelobes in the depth response due to coherent crosstalk between neighbouring pinholes. We have seen such behaviour in Chapter 4 along with some exotic effects of source coherence. We theoretically explore these effects in more detail.

We examine how source coherence affects the depth responses of DVMs employing various pinhole spacings/numbers of pinholes. We will show that, as witnessed in Chapter 4, closely spaced pinholes can result in decreased FWHMs of the depth response curve. We explain this as an effect of destructive interference when crosstalk between neighbouring pinholes occurs. Using pinholes arranged in a square grid as an example, we move on to show that the use of pinhole arrays which consist of regularly arranged pinholes can accentuate the problematic sidelobes of the depth response. We show that by arranging pinholes in a rectangular grid rather than square grid, the optical sectioning strength can be improved significantly. Finally, by examination of the depth responses corresponding to the infinite pinhole array limit, we make some general statements about source coherence and the characteristics of arrays which are likely to perform well.

5.1   Introduction

The tandem-scanning [20] or direct-view microscope has found applications in areas such as the bright-field and florescence imaging of biological samples [23] and 3-D surface topology measurements of semiconductor samples [22]. Typically such microscopes are used in conjunction with incoherent light sources such as arc lamps. However, because of the low light throughput (typically 4%) [25] of the 'Nipkow disc' pinhole arrays used, and the fact that such arc lamps must be spectrally filtered for many applications, light levels in the image plane can be extremely low. Laser sources would offer an improvement on throughput levels due to their monochromatic and high intensity nature, however the behaviour of DVMs using such sources has not been thoroughly investigated. Hewlett *et al.* [30] have examined the general behaviour of coherent source DVMs and concluded that their imaging characteristics are likely to be inferior to incoherent source DVMs due to the presence of large sidelobes in the depth responses.

Fewer *et al.* [62] attempt to explain such sidelobes in terms of a ray optics model with some success, showing that the sidelobes are a result of coherent crosstalk between neighbouring pinholes in the array. Furthermore, it is shown that the axial position of the sidelobe coincides with a large number of cases of constructive interference resulting from this crosstalk. We take this analysis further by examining cases of destructive as well as constructive interference. We start at first by examining 1-D arrays and note some interesting results which we explain in terms of the ray optics model. We then examine 2-D arrays in detail and, finally, we show how, from an optical sectioning point of view, rectangular arrays can outperform square arrays of similar dimensions in a practical imaging system.

Finally, we introduce some equations which will be invaluable in the study of coherent source brightfield direct-view microscopy. For ease of computation we choose to concentrate on DVMs which employ arrays of circular apertures (pinholes) throughout.

5.2 DVM optical sectioning strength

Equations describing the depth response of a coherent source brightfield DVM employing arrays of pinholes have been presented in Chapter 4. We now present the corresponding equations describing the depth response of an incoherent source brightfield DVM [33]. The theory used [32, 30] is a scalar one which is based on the Fresnel approximation to the Kirchoff diffraction integral and, as such, is paraxial in nature. The theory, being scalar, treats one component of the polarisation and assumes the polarisation remains unperturbed as the light propagates through the optical system.

In an analogous way to that described in Appendix B.1, the depth response of an incoherent source DVM operating in brightfield mode can be derived via its optical transfer function (Equation (2.41)) as:

$$I_{\text{PLANE}}(u) = \sum_{i=1}^{N} \sum_{k=1}^{N} \int_0^2 \left| F_{S_1}\left(\frac{\rho}{M}\right) \right|^2 g(2u, \rho) J_0\left(\frac{\rho}{M} |\mathbf{T}_i - \mathbf{T}_k|\right) \rho d\rho. \qquad (5.1)$$

With F_{S_1} given by Equation (4.3) and g given by Equation (2.48).

5.2.1 Infinite array limit

In order to examine the general imaging trends of different DVM configurations in a computationally efficient way, it is useful to examine the depth response corresponding to a DVM employing an infinite array of pinholes. Such equations represent a worst case scenario for the imaging, as the resolution tends to decrease as the number of pinholes increases.

Incoherent source DVM

Following McCabe *et al.* [25] we assume a square/rectangular geometrical arrangement of pinholes and write the pinhole vector $T_i = (kR_x, lR_y)$ where R_x, R_y are the centre-to-centre pinhole spacings in the x and y-directions respectively, and k, l are integers. To derive the infinite array limit we take the $\lim_{N \to \infty}$ of Equation (5.1), which, for identical

circular lenses, gives:

$$\lim_{N \to \infty} I_{\text{PLANE}}(u) = \sum_k \sum_l \left| F_{S_1} \left(\frac{2\pi k}{R_x}, \frac{2\pi l}{R_y} \right) \right|^2 g \left(2u, \frac{M 2\pi k}{R_x}, \frac{M 2\pi l}{R_y} \right), \tag{5.2}$$

where cut-off of the convolution function g [25, 41] (see also Equation (2.48)) gives the following requirement for k, l:

$$\left(\frac{k}{R_x} \right)^2 + \left(\frac{l}{R_y} \right)^2 \leq \left(\frac{1}{M\pi} \right)^2. \tag{5.3}$$

Equation (5.2) is identical to that presented by McCabe *et al.* [25] and reduces to that derived by Wilson *et al.* [33]. The equation gives valuable insight into the general imaging behaviour of incoherent source DVMs; *i.e.* if pinhole arrays of a given pinhole spacing/pinhole size perform well in the infinite array scenario, they can be expected to perform well in a finite array scenario.

Coherent source DVM

In Chapter 4 we presented an equation describing the depth response of a coherent source brightfield DVM (Equation (4.4)). By taking the $\lim_{N \to \infty}$ of Equation (4.4) we have derived, for the first time an expression describing the depth response of a coherent source DVM employing an infinite pinhole array. The derivation is presented in Appendix A.3 and gives the following expression:

$$\lim_{N \to \infty} I_{\text{PLANE}}(u) = \int_0^{2\pi} \int_0^{v_p} \left| \sum_k \sum_l F_{S_1} \left(\frac{2\pi k}{R_x}, \frac{2\pi l}{R_y} \right) P \left(2u, \frac{M 2\pi k}{R_x}, \frac{M 2\pi l}{R_y} \right) \right.$$
$$\left. \exp \left(2\pi j r \left[\frac{k}{R_x} \cos\theta + \frac{l}{R_y} \sin\theta \right] \right) \right|^2 r \, dr \, d\theta, \tag{5.4}$$

where cut-off of the pupil function P gives the following requirement for k, l:

$$\left(\frac{k}{R_x} \right)^2 + \left(\frac{l}{R_y} \right)^2 \leq \left(\frac{1}{2M\pi} \right)^2. \tag{5.5}$$

Equation (5.4) gives valuable insight into the general imaging behaviour of coherent source DVMs. In its present form, Equation (5.4) is a computationally efficient expression which will accurately describe the depth responses of ideal coherent source DVMs employing a large number of pinholes. This calculation would previously have been difficult to perform because the computation time of Equation (4.4) scales with the square of the number of pinholes. Further, we will show how a simple expression which predicts the axial location of the most prominent sidelobes of the depth response can be derived from this equation. A similar equation can be derived which predicts the location of minima in the depth response. Finally, applying these two equations to rectangular arrays predicts which are likely to exhibit superior resolution.

5.2.2 Ray optics model

Following the approach of Fewer *et al.* [62], we attempt to understand the sidelobes resulting from coherent crosstalk in the coherent source DVM in terms of a simple ray optics model. We examine 1-D arrays for simplicity and show how this idea can easily be extended to 2-D arrays. Figure 5.1 shows a series of pinholes of spacing a arranged in a line in the focal plane of an objective lens. We have identified two varieties of crosstalk depicted by the parts (a) and (b) in the figure. Following the approach of Fewer *et al.*, we can describe the path length differences, Δl, between the two light rays in part (a) of the figure as:

$$\Delta l = 2\sqrt{\frac{a^2}{2} + z^2} - 2z,$$ (5.6)

and in part (b) of the figure as:

$$\Delta l = 2\sqrt{\frac{b^2}{2} + z^2} - 2\sqrt{\frac{a^2}{2} + z^2}.$$ (5.7)

For constructive and destructive interference we equate both the above to $m\lambda$, where for constructive interference $m = 0, 1, 2, 3, \ldots$ and for destructive interference $m` =$
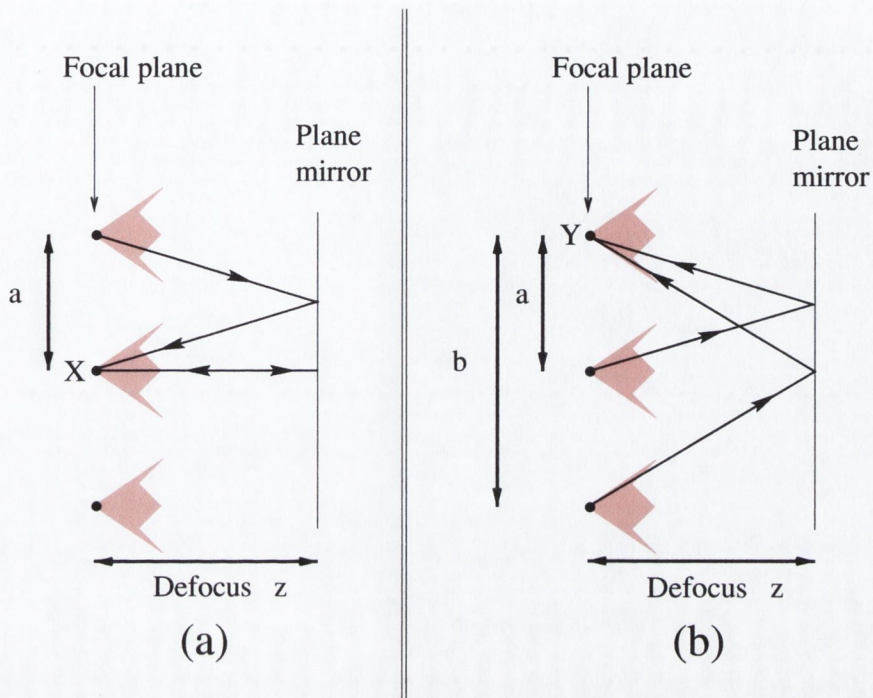
Figure 5.1: The image of a 1×3 pinhole array in the focal plane of an objective lens. Crosstalk occurs between pinholes when the mirror is sufficiently displaced from the focal plane. Two types of interference are shown: (a) interference at X, (b) interference at Y.

$1/2, 3/2, 5/2, \ldots$. We solve both equations for z to arrive at

$$z = \frac{a^2}{4m\lambda} - \frac{m\lambda}{4},$$

(5.8)

and (taking the positive root):

$$z = \sqrt{\frac{m^2\lambda^2}{16} + \frac{1}{4m^2\lambda^2}\left((a^2 + b^2)^2 - a^2b^2\right)} - \frac{a^2 + b^2}{8},$$

(5.9)

respectively. Furthermore, for a 1-D array of N pinholes we can write the number of occurrences, W, of each case above as:

$$W = 2(N - p).$$

(5.10)

113

In the case of Figure 5.1 (a), $p = 1$ and in the case of Figure 5.1, (b) $p = 2$. Equations (5.8), (5.9), & (5.10) above will be used to explain the prominent sidelobes and other effects seen in the depth responses of coherent source DVMs.

5.3   Square arrays

We have chosen to examine the depth responses of a DVM with the same experimental parameters to those of the PAM described in Chapter 4. Thus the DVM utilises a monochromatic source at 632.8nm in conjunction with a 25×/0.6 NA infinity-corrected objective lens. We examine DVMs employing pinhole arrays comprised of various numbers of pinholes (N) and pinhole separations (R). Again, the notation $\overline{R}$ and $\overline{v_p}$ will be used to denote real coordinates. The pinhole radius $\overline{v_p}$ will be fixed at 7.5μm throughout. At first, we will probe 1-D pinhole arrays, we than apply the ray optics model to explain some of the effects observed.

5.3.1   1-D arrays

In order to increase our understanding of the basic processes at work in coherent source DVMs, we first examined 1-D arrays. Figure 5.2 shows an illustrative example of the results obtained. The graph depicts the depth responses of both coherent (shown in Figure 5.2 (a)) and incoherent (Figure 5.2 (b)) DVMs employing 1×1, 1×2 & 1×5 pinhole arrays with pinhole diameters of 15μm and pinhole spacings of 30μm. In part (a) of the figure (coherent source case), the incidences of constructive and destructive interference, as calculated from the ray optics model of Section 5.2.2 have been superimposed on the depth responses. We first discuss the nature of the depth responses themselves before showing how the ray optics model accounts for the observed behaviour.

A marked difference can be seen between parts (a) and (b) of Figure 5.2. In the case of the coherent source DVM employing 1×2 and 1×5 arrays, an enhanced sidelobe can be seen at $\sim 2\mu$m. Also, another more interesting effect is observed: the full-
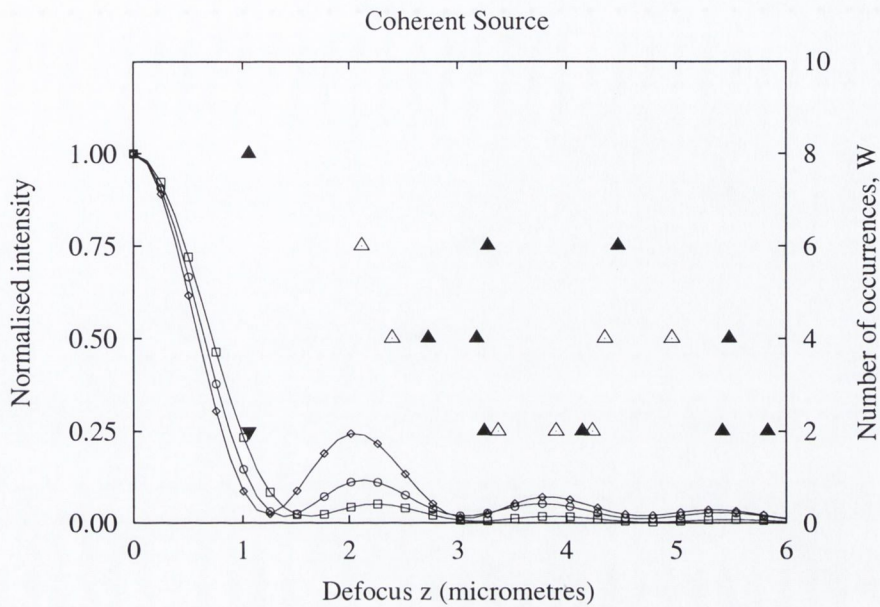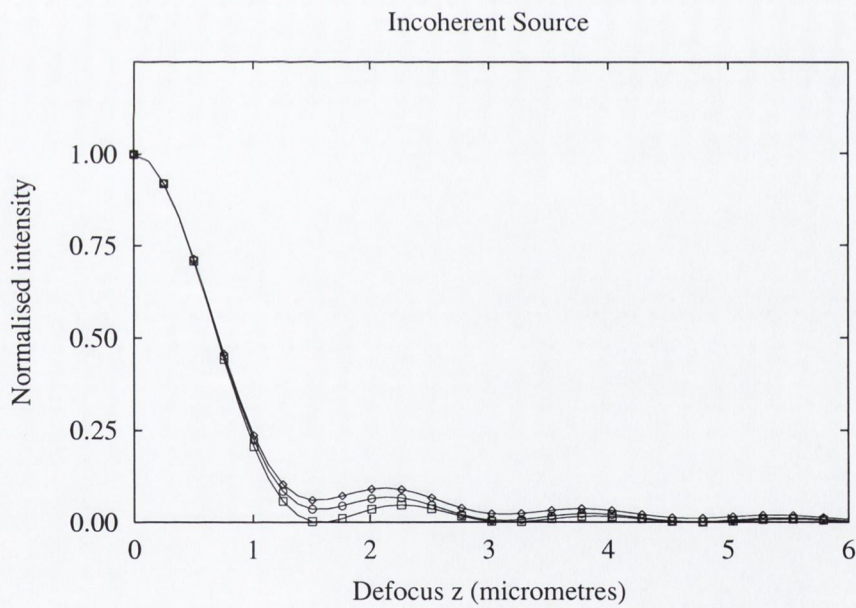
Figure 5.2: Depth responses for DVMs employing $1 \times 1(\square)$, $1 \times 2(\circ)$, and $1 \times 5(\diamond)$ arrays of pinholes. (a) Coherent source; (b) Incoherent source. Overlayed on part (a) of the figure, are predicted cases of constructive and destructive interference resulting from crosstalk in the cases of the 1×2 and 1×5 arrays. The axial position of occurrence of each instance of interference is plotted against its weight of occurrence (the vertical axis to the right). The legend for these is as follows: cases of destructive interference for 1×2 array ▼; cases of destructive interference for 1×5 array ▲; cases of constructive interference for 1×5 array △.

115

width at half maximum (FWHM) of the curves (a figure of merit which represents the depth resolution of the DVM) can be seen to decrease with increasing numbers of pinholes (N). By comparison, the incoherent source DVM shows neither of these effects. Instead, the background level in the depth response can be seen to increase slightly with the number of pinholes; this effect can be understood as the recapture of light which would be lost to a single pinhole DVM. The strength of the effect increases with the number of pinholes because the recapture process becomes more efficient. Although the explicit FWHM decrease seen in the coherent source case is absent, in fact, a depth resolution enhancement can be achieved as described by Hanley *et al.* [51] who took the approach of subtracting this heightened background level before calculation of the FWHM, giving an artifically decreased value for the FWHM. In practice, the post processing of the image required to achieve background subtraction is likely to reduce contrast in the image and decrease the rate of image acquisition. By comparison, the FWHM decrease we have seen in coherent source DVMs is an intrinsic property of the imaging.

Liang *et al.* [67] appear to have seen experimental evidence of this coherent source effect. However due to the use of an approximated formula (which neglected factors such as finite pinhole size) to determine the axial resolution, no strict conclusions can be drawn. In Chapter 4, we have seen examples of this kind of behaviour. Figure 4.14 showed the experimental depth responses of arrays of square apertures each of diameter $14\mu m$ and centre-to-centre spacings ($\overline{R}$) of 30μm, 45μm, & 60μm. Part (a) of the figure showed that the FWHM of the depth response of the $\overline{R} = 30\mu$m array is less than that of the $\overline{R} = 60\mu$m array. This behaviour is also predicted by the theoretical depth response (part (b) of the same figure) and appears to be experimental evidence of the effect described above. In an attempt to understand both the effects seen in Figure 5.2 (a) we next applied the ray-optics model described in Section 5.2.2.

Calculated incidences of both constructive and destructive interference for the coherent source DVM, along with their weights of occurrence, are shown in Figure 5.2 overlayed on the depth responses of the corresponding arrays. The legend is shown in

the figure caption. In the case of the 1×2 array, the figure shows that crosstalk between adjacent pinholes results in one case (which occurs two times) of fully destructive interference (at a defocus of $1.06 \mu m$) and no cases of fully constructive interference. This particular case of destructive interference results from crosstalk of the type featured in Figure 5.1 (a) between the two pinholes in the array. This effect manifests itself in the depth response as a shift in the point where the first minimum in the depth response occurs; the result is a decrease in the FWHM of the depth response. In the case of the 1×5 array, Figure 5.2(a) shows a large number of incidences of both constructive and destructive interference, the most prominent of these again occurs at a defocus of $1.06 \mu m$. It can again be postulated that this case of destructive interference causes a decrease in the FWHM of the depth response. Due to the higher weight of occurrence, the effect is stronger than that of the 1×2 array.

Another effect seen in Figure 5.2 (a) is an enhanced sidelobe which occurs at $\sim 2 \mu m$. This sidelobe coincides with two cases of constructive interference (weights 6 & 4). At higher values of defocus, many competing cases of constructive/destructive interference can be seen. This enhanced resolution is an effect which, to our knowledge, has not previously been reported and represents an improvement in the FWHM of the depth response of $\sim 10\%$ for the 1×2 array and $\sim 12\%$ for the 1×5. This suggests that the use of a scanned subgroup of pinholes could be used to achieve improved depth resolution in surface topology or profiling measurements of specularly reflecting samples such as semiconductor devices.

In addition to the investigation performed above, depth response curves were simulated for a wide range of pinhole array dimensions. For conciseness we do not show the results here. The general trends observed suggested that the decreased FWHM effect was only present when pinholes in the array were placed closely together. We now move on to explore 2-D arrays of pinholes arranged in a square geometry.
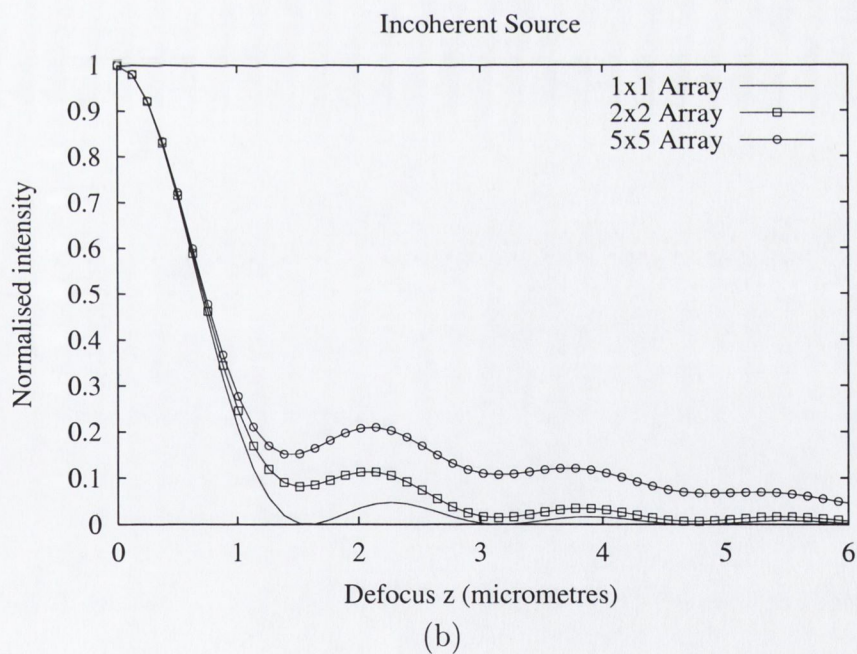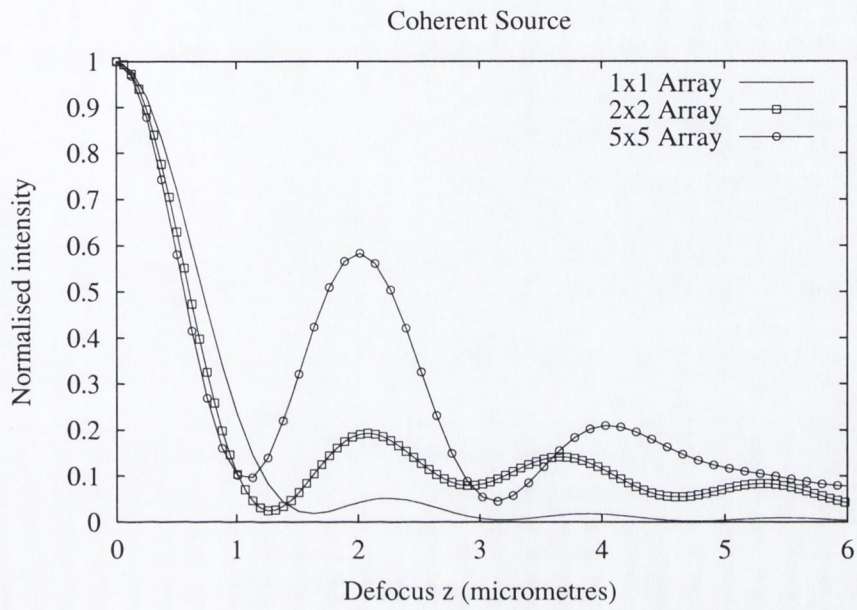
Figure 5.3: Theoretical depth responses for DVMs employing 1×1, 2×2 & 5×5 pinhole arrays with pinhole diameters of 15μm and pinhole spacings of 30μm. (a) coherent source; (b) incoherent source.

5.3.2   2-D arrays

Two-dimensional pinhole arrays are more commonly used in DVMs as they allow faster image acquisition rates than 1-D arrays, we now demonstrate the broad behaviour of 2-D pinhole arrays for DVMs employing coherent light sources. We first examine the 2-D counterparts of the arrays of Figure 5.2; depth responses for said arrays are shown in Figure 5.3. Similar effects to those of Figure 5.2 are observed: again we note a decrease in FWHM and dramatically enhanced sidelobe levels. Due to the symmetry of the square pinhole array (equal spacing in x and y-directions) the weight of occurrence of each interference incidence is increased by a factor of n (for an array of $n \times n = N$ pinholes); this explains the heightened sidelobes of 2-D compared to 1-D arrays.

We note that there exist other orders of interference, for example between pinholes which are diagonally separated but, from a symmetry point of view these will be less significant than those described above. Again in the case of the incoherent source DVM (Figure 5.3 (b)), the background level of the depth response is seen to increase with the number of pinholes in the array. This can again be understood as an effect of the recapture of light by the process of crosstalk, because the phenomenon is not a coherent process, no highly localised peaks or troughs are encountered. The effect is stronger for 2-D over 1-D arrays due to the fact that more pinholes take part in the recapture process.

Sidelobe variation with the total number of pinholes, N

We have seen that the height of sidelobes in the depth responses of coherent source DVMs increases with the number of pinholes in the array, we now explore this in more detail. We choose $\overline{v_p} = 7.5\mu m$ and $\overline{R} = 60\mu m$. The number of pinholes is varied up to the infinite array limit and the depth response behaviour studied.

Figure 5.4 shows the depth responses of both coherent and incoherent source DVMs employing pinhole arrays with 1×1, 2×2, 5×5, 10×10 and infinite pinhole arrays. For ease of viewing each set of data in the figure has been vertically offset from the

previous set, the scaling remains the same throughout so that the curves can be directly compared. In addition, we have plotted a series of dashed lines which represent the zero reference for each of the offset curves. In the case of the incoherent source DVM (part (b) of the figure), the background level of the depth response is seen to increase with the number of pinholes, again the data have been vertically offset for ease of viewing.

As demonstrated by Wilson *et al.* [33], in the case of the infinite pinhole array incoherent source DVM, in the limit as defocus u approaches infinity, the normalised background level in the depth response converges to a value, B say, between 0 and 1 which depends on the pinhole array dimensions. If the pinholes are spaced very closely together B is likely to be close to 1, *i.e.* very poor contrast between in-focus and out-of-focus regions. Whereas, when the pinholes are spaced very far apart B is likely to be close to 0 *i.e.* excellent contrast between in-focus and out-of-focus regions.

In the case of the the coherent source DVM (Figure 5.4 (a)) no such convergence occurs. From Equation (5.4), it can be seen that the value of $I_{\text{PLANE}}(u)$ oscillates as u grows. In order to pinpoint the exact behaviour, we expand the pupil function of Equation (5.4) to give:

$$P\left(2u, \frac{M2\pi k}{R_x}, \frac{M2\pi l}{R_y}\right) = \exp\left(\frac{-j4\pi^2 u M^2}{R^2}(k^2 + l^2)\right). \tag{5.11}$$

We note from Equation (5.11) that the in-focus case of $u = 0$ is, in the case of a square array with apertures spaced by R, identical to the cases specified by the following:

$$|u|(k^2 + l^2) = \left(\frac{R^2}{2\pi M^2}\right) q \qquad \forall \text{ integers } k, l; \tag{5.12}$$

(due to the fact the pupil function, P, is periodic with period 2π), where q is an integer and k & l are specified by Equation (5.5). If k & l, thus specified, are both equal to zero then the condition described by Eq. (5.12) is satisfied for all u. Thus, $I(u) = 1$ for all values of defocus in this case. If k & l are non-zero, then Eq. (5.5) becomes
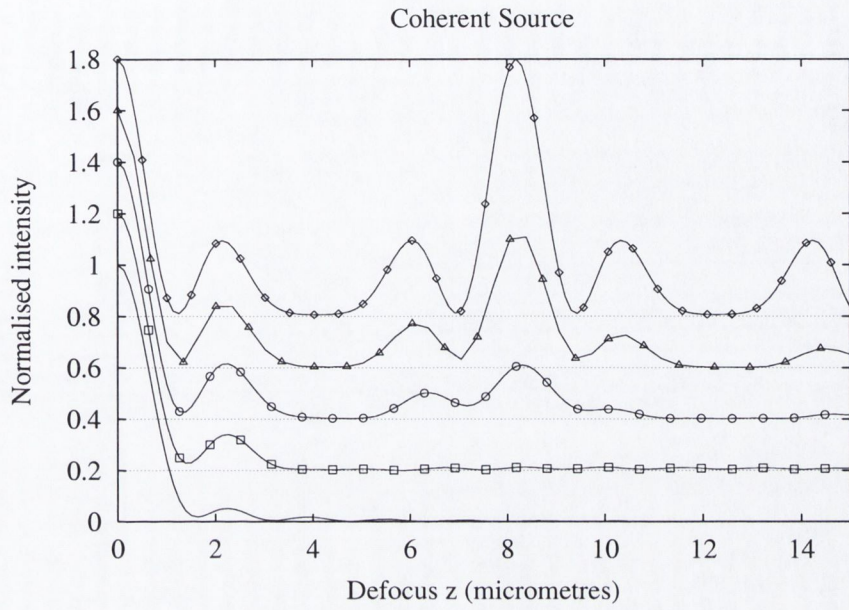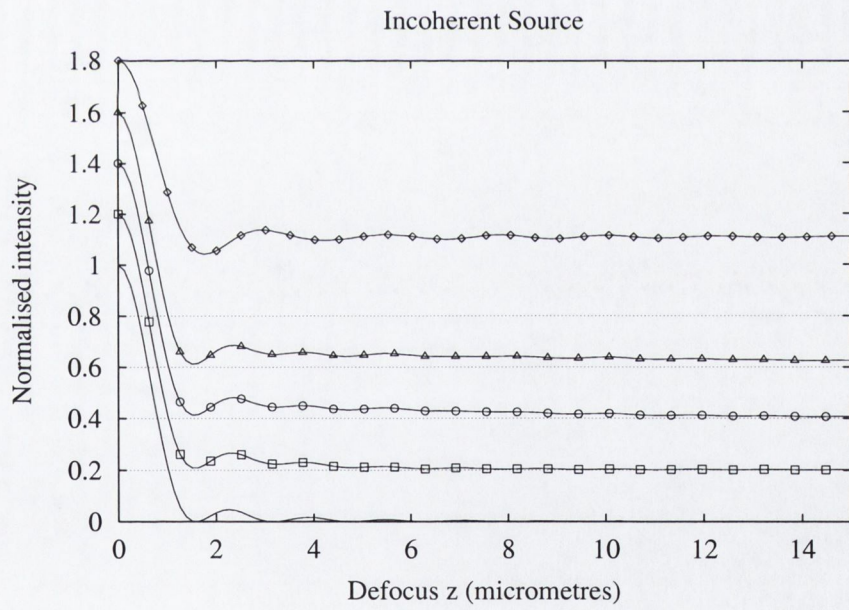
Figure 5.4: Theoretical depth responses for DVMs employing 1×1 (solid line), 2×2 ($\square$), 5×5 ($\circ$), 10×10 ($\triangle$) & infinite ($\diamond$) pinhole arrays with pinhole diameters of 15μm and pinhole spacings of 60μm. The depth responses have been vertically offset from each other so that each curve can be clearly distinguished. The series of dashed lines represents the zero reference for each of the offset curves. (a) Coherent source; (b) Incoherent source.

121

equivalent to:

$$|u| = \left(\frac{R^2}{2\pi M^2} \right) q \qquad (5.13)$$

or, in terms of real co-ordinates:

$$|z| = \left(\frac{\overline{R}^2 n \cos^2\left(\frac{\alpha}{2}\right)}{\lambda M^2} \right) q \qquad (5.14)$$

where $\overline{R}$ is the pinhole spacing in real co-ordinates. So, in the case of a coherent source DVM employing an infinite pinhole array, it is possible for the out-of-focus intensity to equal the in-focus intensity for certain values of defocus.

The effect described by the preceeding equations is related to a self-imaging effect first reported by Talbot [79] whereby coherent illumination diffracted from a periodic structure reforms into an image of the original structure at certain specific distances from it. The planes where such self-imaging occurs are known as Talbot planes. Recent work [49] in multifocal multiphoton (fluorescence) microscopy has commented on the significance of Talbot planes, and fractional Talbot planes to confocal microscopy. Sidelobes occurring in the depth responses of such are related to the Talbot planes. However, due to the incoherent nature of the generated fluorescence in such systems, the Talbot planes have a lesser effect. Evidently, in the case of a coherent source brightfield DVM, due to the coherent nature of the (reflected) light and the infinite extent of the pinhole array, the Talbot self-imaging effect can cause sidelobes which are as significant as the mean peak in the depth response. Furthermore, other (lesser) sidelobes appearing in the depth response can be related to the fractional Talbot planes which are spaced at rational multiples of the Talbot planes.

It is convenient at this point to introduce some terminology, we ascribe the label 'principal' sidelobes to those represented by Equation (5.14). In practical DVMs, as evidenced by Figure 5.4 (a), the use of finite arrays ensures that the level of the principal sidelobes will not equal the in-focus intensity. However the principal sidelobes are the

most problematic artifact of coherent source imaging.

Another look at Figure 5.4 shows that, in the case of the infinite array, the depth response is close to zero at certain points. These points in the depth response appear to occur at the midpoints between successive maxima, *i.e* at axial positions given by:

$$|u| = \left(\frac{R^2}{4\pi M^2} \right) r, \tag{5.15}$$

with $r = \pm 1, \pm 3, \pm 5, \ldots$. Substitution of Equation (5.15) into the pupil function of Equation (5.4) reveals the effect, the pupil function is now given by:

$$P = \exp(-jr\pi[k^2 + l^2]). \tag{5.16}$$

If the term $k^2 + l^2$ is even the pupil function becomes 1, while if $k^2 + l^2$ is odd the pupil function becomes -1. It can be shown (see Appendix B) that for square arrays, as k and l run through the range specified by the cut-off of Equation (5.5), the term $k^2 + l^2$ will be even exactly once more than it is odd. Thus the pupil function in Equation (5.16) is alternatively positive and negative as $k^2 + l^2$ is even and odd respectively. For this reason the sum of Equation (5.4) tends to average to zero and a minimum in the depth response is the result. Effectively the 'odd' spatial frequencies suffer a π phase change while the 'even' spatial frequencies do not and this effect can be related to the inverse self-images which appear equally spaced between the Talbot planes.

The effects described above exist also for 1-D periodic arrays of pinholes, this fact suggests that the use of a rectangular array of appropriate dimensions could cause suppression of some of the maxima in the depth response. For example, if the depth response maxima resulting from periodically spaced pinholes in the x-direction were matched to the depth response minima resulting from periodically spaced pinholes in the y-direction. We will discuss this further in Section 5.4. Before doing so, it is instructive to probe the general behaviour of square arrays.

Since the sidelobe level of the depth response is the main factor which determines a

given pinhole array's usefulness from an imaging point of view, we now explore how sidelobe level varies with both the number of pinholes (N) and the centre-to-centre spacing of pinholes. Once again, the pinhole diameters were fixed at 15μm. Figure
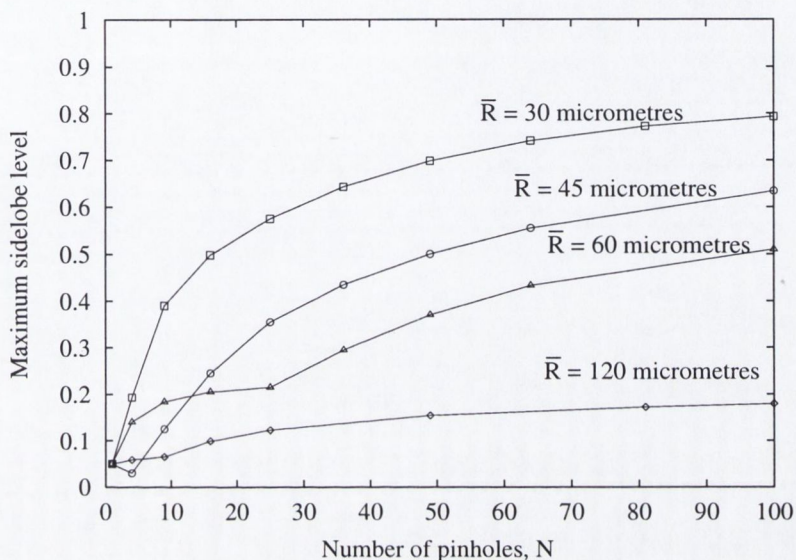
Figure 5.5: Variation of the maximum sidelobe level in the depth responses of several square pinhole arrays (expressed as a fraction of the in-focus intensity) as a function of the total number of pinholes, N, for pinholes spacings, $\overline{R}$, of 30μm,45μm,60μm & 120μm.

5.5 shows the variation of the level of the maximum sidelobe in the depth response (expressed as a fraction of the in-focus intensity) with the number of pinholes, N, in the array. Each curve in the figure represents the variation of maximum sidelobe level with N for a different value of pinhole spacing R. It can be seen that as N increases the level of the maximum sidelobe increases; this effect is simply due to the fact that the sidelobe is a result of coherent crosstalk between pinholes. The more pinholes in the array, the greater the number of occurrences of each incidence of constructive interference. Also, it is evident from this figure that, with N fixed, as R is increased the maximum sidelobe level decreases. This is a result of the fact that the defocus point where crosstalk first occurs will be larger in the case of widely spaced arrays and so the light intensity available to the sidelobe will be less.

Distinct kinks can be seen in some of the curves due to an effect which can be seen, for example, by examining the curves representing the 5×5 and 10×10 arrays of Figure 5.4 (a). Between these two curves, the maximum sidelobe in the depth response jumps from being the 1st sidelobe (at $\sim 2\mu$m) to the 3rd sidelobe (at $\sim 8\mu$m). For any curve in Figure 5.5 (a), a number of these jumps in the dominant sidelobe will occur until the principal sidelobe becomes dominant. As N increases beyond this point, the normalised maximum sidelobe level smoothly approaches 1. Thus, in practical coherent source DVMs there will be a trade-off between the number of pinholes and the pinhole spacing in order to ensure that the principal sidelobes do not become dominant.

Sidelobe variation with pinhole spacing, R

In this section we further investigate the variation of the maximum sidelobe level in the depth response with the pinhole separation R. We fix the pinhole diameter at 15μm and the number of pinholes at 5×5; the centre-to-centre pinhole spacing is varied between between 15μm and 240μm. The resulting depth responses are plotted in Figure 5.6. The case of infinitely spaced pinholes has also been plotted, this case is identical to the single pinhole depth response and thus we have used the single pinhole depth response in its place. It is apparent from the figure that, from an optical sectioning point of view, the imaging in a coherent source DVM will be significantly worse than that of an incoherent source DVM. Even for spacings up to 120μm, prominent sidelobes are seen in the depth response of the coherent source DVM. This is in stark contrast to the incoherent source case where the depth response of the 120μm spaced array is almost identical to that of the infinitely spaced array.

The general behaviour of sidelobes in the depth response, in the coherent source case, is demonstrated by Figure 5.7. Two curves are plotted, corresponding to $N = 4$ (2×2 array) and $N = 25$ (5×5 array); in both cases $\overline{R}$ was varied between 15μm and 240μm. In the case of the $N = 4$ curve, the maximum sidelobe level settles down to the single pinhole level of $\sim 5\%$ of the in-focus intensity at spacings as little as 90μm. At a pinhole spacing of 45μm a curious effect can be observed, the maximum sidelobe level
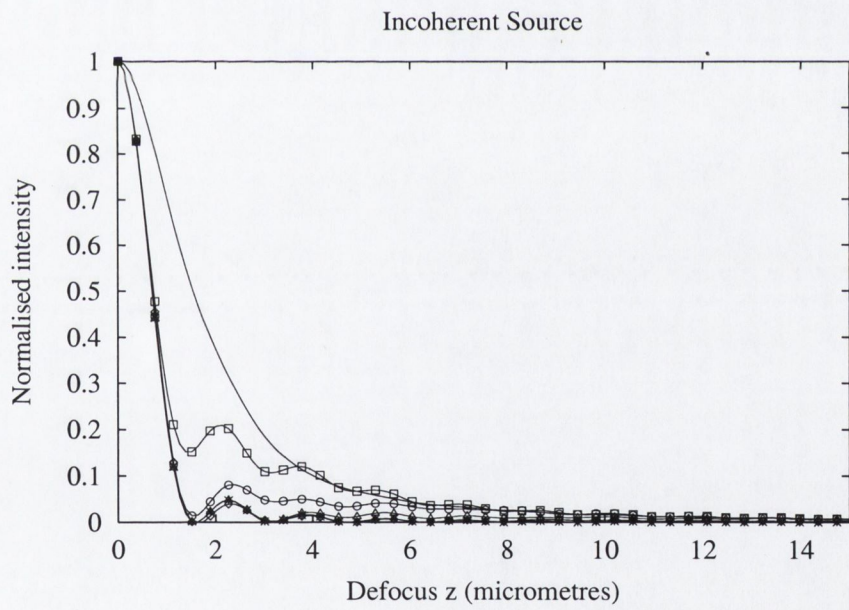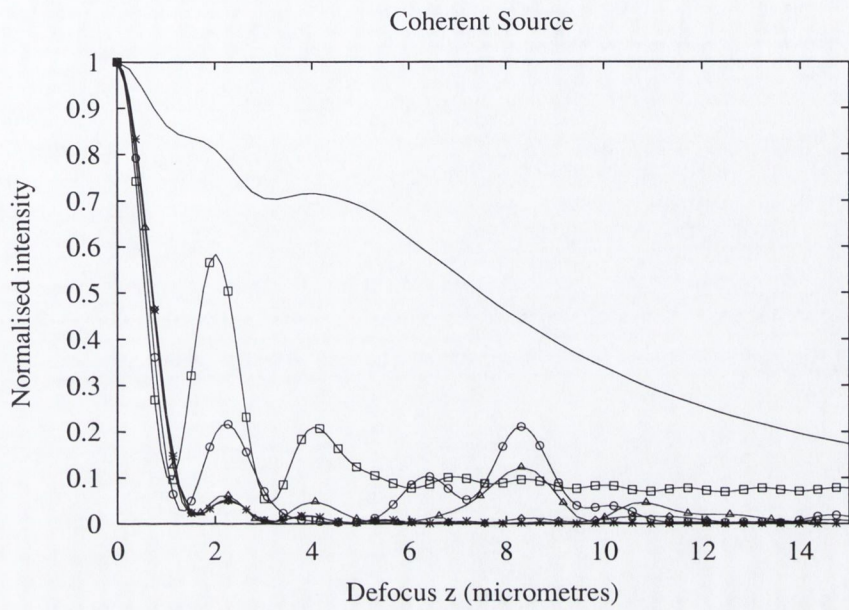
Figure 5.6: Theoretical depth responses for DVMs employing 5×5 square pinhole arrays with pinhole diameters of 15μm and centre-to-centre pinhole spacings of 15μm (solid line), 30μm ('□'s overlayed), 60μm ('○'s overlayed), 120μm ('△'s overlayed), 240μm ('◇'s overlayed), & infinitely spaced array ('*'s overlayed). (a) coherent source; (b) incoherent source.

drops below that of the single pinhole DVM (5% of the in-focus intensity), it should be stressed however that this was at the expense of FWHM of the depth response. Nevertheless, this suppression of the sidelobes could offer a slight decrease in the level of background light in cases where the depth resolution is not a primary concern. For example, when dealing with samples with surface profiles which vary on a scale much greater than the depth resolution. In the case of the $N = 25$ curve the decrease in maximum sidelobe level is much more gradual; pinhole spacings of 240μm are needed before it approaches the single pinhole level. This suggests that in practical coherent source DVMs, pinhole spacings of upwards of 16 times the pinhole diameter may be needed for quality imaging.

Figure 5.7: Variation of the maximum sidelobe level in the depth response (expressed as a fraction of the in-focus intensity) as a function of the pinhole spacing, $\overline{R}$. The pinhole diameter was 15μm.

We conclude that both the number of pinholes in an array and their spacing are important factors which dramatically effect image quality in coherent source DVMs. Ideally, the number of pinholes should be kept as small as possible and the pinhole spacing as large as possible. Both of these constraints limit the field of view of the

DVM while the second constraint will also limit the light throughput of the instrument. We now attempt to relax these constraints by considering the use of 2-D arrays where pinholes are arranged in a rectangular geometry (different spacings in x and y directions).

5.4   Rectangular arrays

We have shown that the large sidelobes present in the depth responses of coherent source DVMs employing square pinhole arrays are due mainly to the symmetry inherent in the square array. We now show that, by breaking this symmetry, rectangular arrays offer an improvement over square arrays. As a particular example of this we compared depth responses of two square arrays with $\overline{R} = 30\mu$m and $\overline{R} = 45\mu$m with a rectangular array with pinhole spacings of 30μm (in the x-direction) and 45μm (in the y-direction). Figure 5.8 (a) shows the improvement possible. In the depth response of the rectangular array, mixing can be seen between the peaks of both the square arrays. The peak at $\sim 2\mu$m in the depth response of the $\overline{R} = 30\mu$m square array is seen (vastly reduced) in the depth response of the rectangular array. Likewise the prominent peak at $\sim 4.2\mu$m in the depth response of the $\overline{R} = 45\mu$m square array can also be seen in the depth response of the rectangular array. So, the depth response of the rectangular array has a maximum sidelobe level less than either of the square arrays while it has a FWHM close to that of the smaller square array; the rectangular array, while having higher optical throughput (smaller mean pinhole spacing) than the 45μm spaced square array, shows better imaging properties. Figure 5.8 (b) shows that this effect does not occur in incoherent source DVMs.

Figure 5.9 (a) again reinforces the improvement possible, the rectangular array (mean pinhole spacing 37.5μm) exhibits smaller sidelobes than the square array (mean pinhole spacing 45μm) for arrays with numbers of pinholes greater than 10. Figure 5.9 (b) shows once again that rectangular arrays outperform square arrays in terms of maximum depth response sidelobe level.
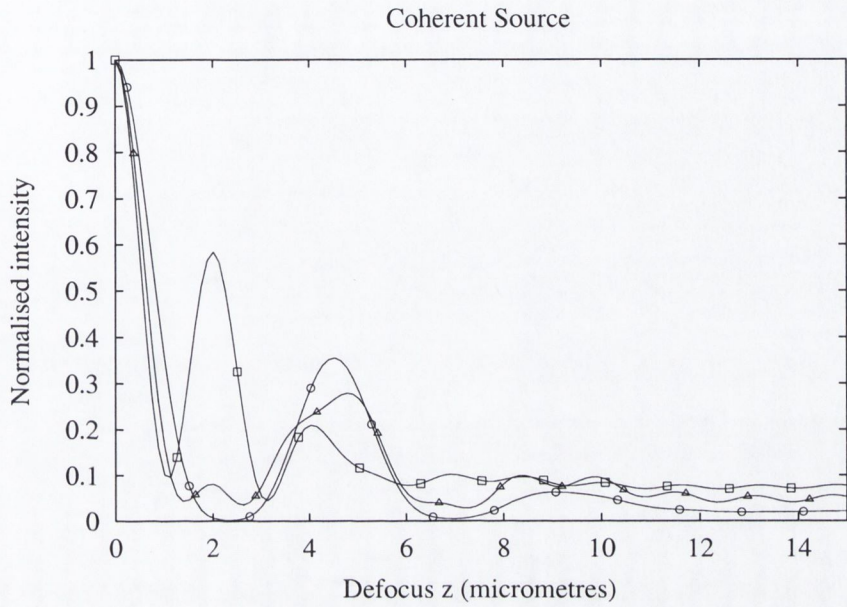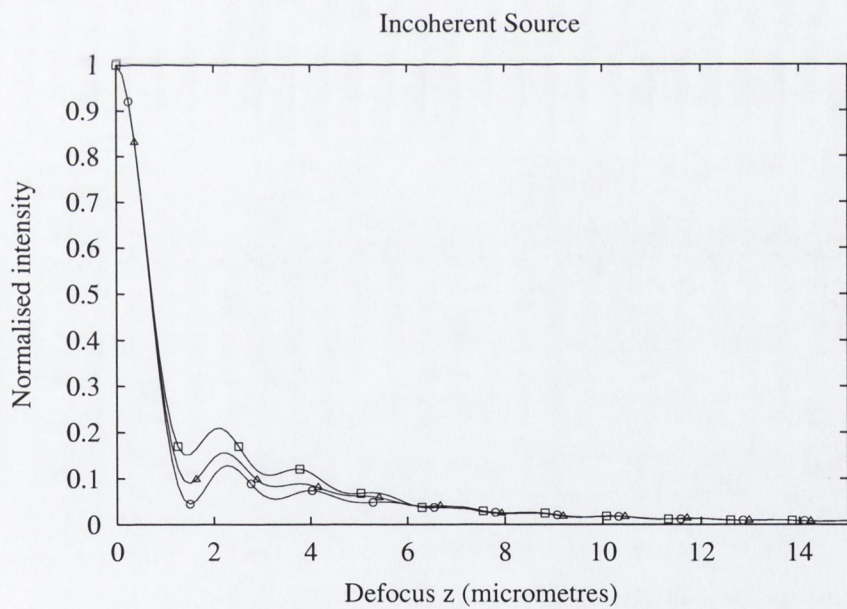
Figure 5.8: Theoretical depth responses for DVMs employing 5×5 pinhole arrays with pinhole diameters of 15μm and pinhole spacings of 30μm square ($\square$), 45μm square ($\circ$) and 30μm $\times$ 45μm rectangular ($\triangle$). (a) Coherent source; (b) Incoherent source.
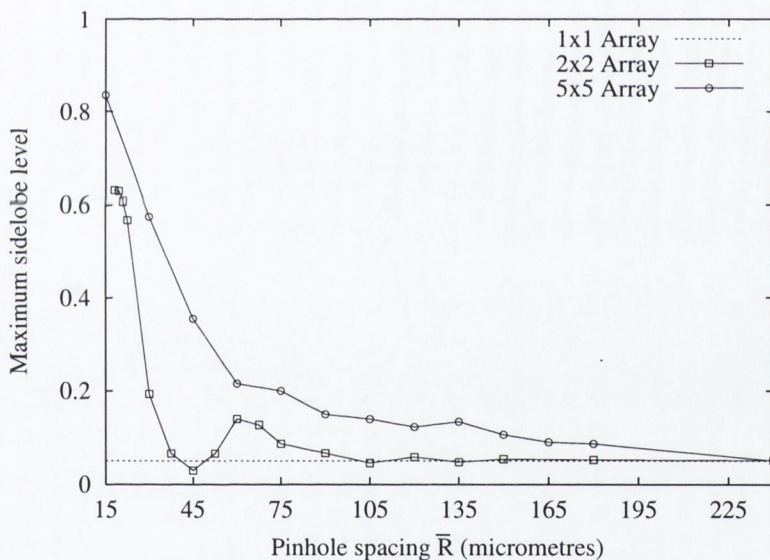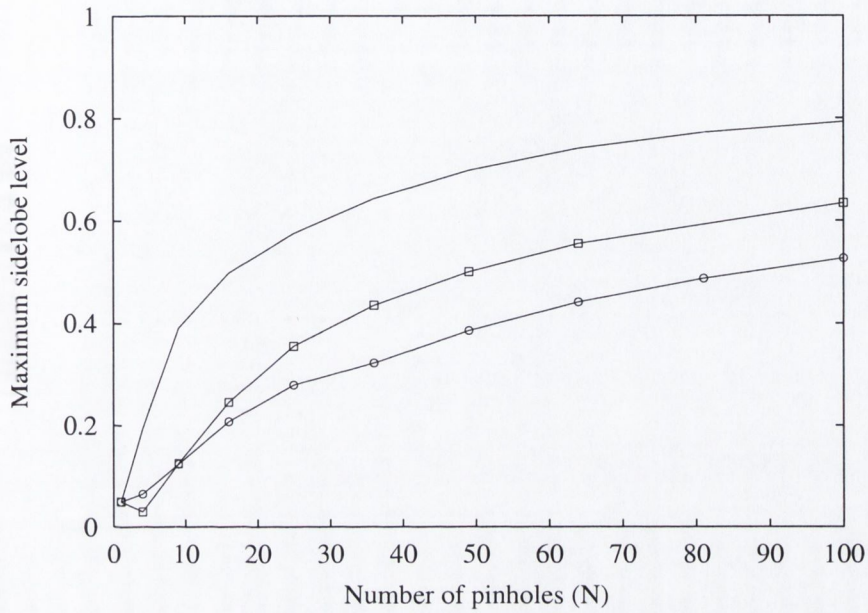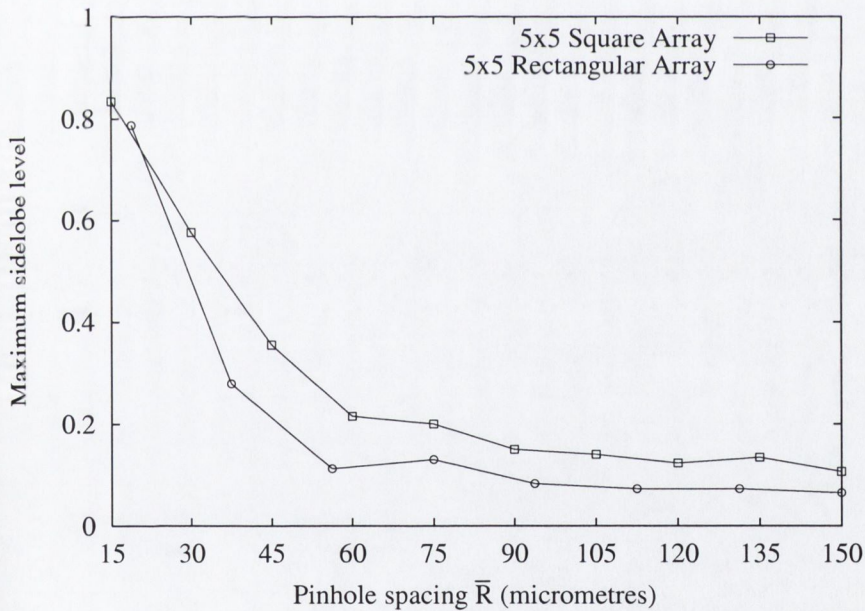
Figure 5.9: Variation of the maximum sidelobe level in the depth response (expressed as a fraction of the in-focus intensity) as a function of: (a) The number of pinholes, N, for pinholes spacings, $\overline{R}$, of 30μm square, 45μm square($\square$) & 30μm × 45μm rectangular($\circ$); (b) The pinhole spacing, $\overline{R}$, for 5×5 square and rectangular arrays.

5.4.1 Infinite rectangular arrays
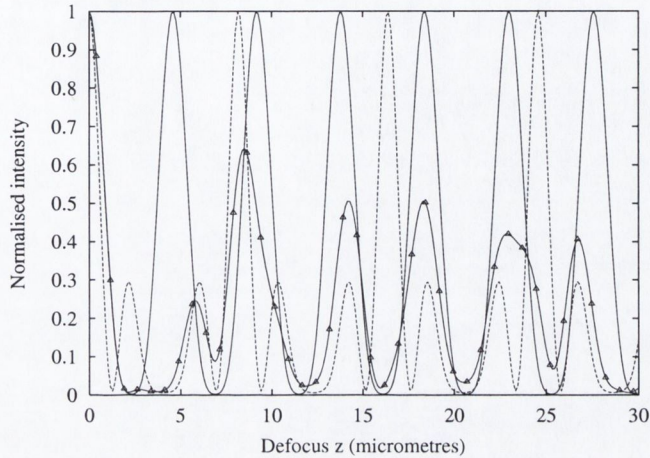
Figure 5.10: Theoretical depth responses for coherent source DVMs employing infinite pinhole arrays. The pinhole diameter is 15μm. The solid curve represents the depth response of a square array with centre-to-centre pinhole spacing of 45μm; the dashed curve is the depth response of a square array with centre-to-centre pinhole spacing of 60μm; and the curve with $\triangle$s overlayed is the depth response of a rectangular array with centre-to-centre pinhole spacings of 45μm (x-direction) and 60μm (y-direction).

Certain insights into the behaviour of coherent source DVMs using rectangular pinhole arrays can be gained by employing Equation (5.4). Computations involving this equation are highly efficient to perform (in contrast to finite array calculations via Equation (4.4)) and give striking demonstrations of the benefits of rectangular arrays. The equation could also be easily adapted to account for other pinhole array configurations such as hexagonal or spiral geometries. In Figure 5.10 we have applied the equation to the case of an infinite pinhole array consisting of 15μm pinholes. The three curves in the figure represent depth responses for a square array with pinhole spacing of 45μm (solid curve), a square array with pinhole spacing of 60μm (dashed curve), and a rectangular array with pinhole spacing of 45μm in the x-direction and 60μm in the y-direction (solid curve with $\triangle$s overlayed). In the case of the rectangular array, sidelobes have been suppressed to a large extent. Examination of Equation (5.14) predicts that, in rectangular arrays with pinholes spaced by R_x in the x-direction and R_y

131

in the y-direction, principal sidelobes will be present only when:

$$\left(\frac{R_x}{R_y}\right)^2 = \frac{q_2}{q_1} \ , \tag{5.17}$$

for some values of the integers q_1 and q_2. Thus, principal sidelobes will only occur when $(R_x/R_y)^2$ is rational and will occur at integer multiples of:

$$u = \left(\frac{R_x^2}{2\pi M^2}\right) q_1 \ \text{ or equivalently } \ u = \left(\frac{R_y^2}{2\pi M^2}\right) q_2, \tag{5.18}$$

where q_1 and q_2 are given by Equation (5.17). If R_x and R_y are specifically chosen such that $(R_x/R_y)^2$ is irrational then principal sidelobes will never occur. Unfortunately, because most spatial light modulators consist of an array of pixels, it will often not be possible to choose R_x and R_y such that $(R_x/R_y)^2$ is irrational. However, by choosing them appropriately the principal sidelobes can be made to occur at defocus positions very far from the focal plane so that they are effectively eliminated.

5.5   Practical arrays

We now discuss the minimal condition for pinhole spacing so that we can maximise light throughput while minimising negative imaging defects. We use the mark-space ratio, m_s (ratio of pinhole spacing to pinhole diameter), for this purpose.

5.5.1   Incoherent source DVMs

Two negative effects which can result from the use of inappropriate pinhole arrays in incoherent source DVMs are an increased FWHM of the depth response and an increase in the background level of the depth response. In the early days of direct-view [22] or tandem-scanning microscopes, mark-space ratios of at least 10 were used in order to eliminate these effects. More recently, McCabe et al. [25] showed that, in most practical arrays, mark-space ratios as low as 5 could be used before the onset of
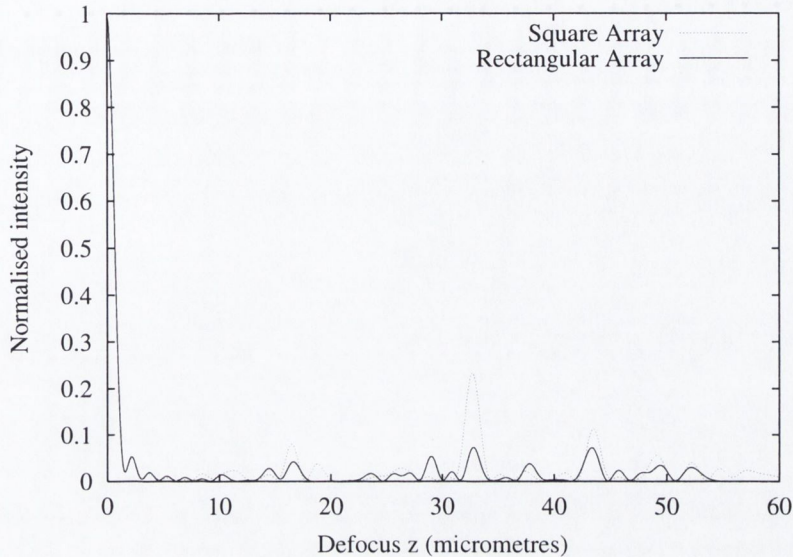
Figure 5.11: Theoretical depth responses for coherent source DVMs employing infinite pinhole arrays. The dashed curve represents the depth response of a square array with centre-to-centre pinhole spacing of 240μm; the solid curve is the depth response of a rectangular array with centre-to-centre pinhole spacings of 240μm (x-direction) and 225μm (y-direction).

significant degradation of the FWHM of the depth response.

The issue of background levels in DVMs has been addressed by Wilson [33] *et al.*: the background level in the depth response of an infinite array DVM was predicted by taking the limit as $u \rightarrow \infty$ of Equation (5.2). This serves as an upper bound for the background we could expect to see in a finite sized pinhole array. It appears from Wilson's calculations that, even for small pinholes ($v_p = 1$ optical units), centre-to-centre pinhole spacings of over 30 optical units are needed in order to reduce the background level in the depth response until it is equal to that of a single pinhole DVM. In practice however, the infinite array background level tends to be much higher than the background levels reached by most finite arrays. As a particular example of this, Figure 5.4 (*b*) shows that even for arrays consisting of up to 10×10 pinholes, the background level in the depth response is well off the infinite array limit. We conclude that, for most practical arrays, the figures advised by McCabe *et al.* [25] are likely to

represent a reasonable lower limit for m_s.

5.5.2 Coherent source DVMs

As we have seen, the main negative effect of coherent source DVMs from an optical sectioning point of view are enhanced sidelobes in the depth response. The FWHM, in general, lies close to the single pinhole limit although in certain cases it can vary by a small amount. In order to reduce the prominence of the sidelobes in the depth response we can take two approaches: either we minimise the number of pinholes in the array or we maximise the spacing between the pinholes. It is difficult to arrive at a generally applicable figure of merit for the mark-space ratio of the array: the optimum array is likely to depend strongly on the type of sample to be imaged and the particular properties of imaging required. However, as an illustrative example of an array which would perform well in many situations, Figure 5.11 shows the depth response of a rectangular pinhole array employing an infinite number of pinholes with pinhole diameters of 15μm and centre-to-centre pinhole spacing of 225μm in the x-direction and 240μm in the y-direction. The figure shows negligible sidelobes in the depth response. By comparison the square array featured in the figure, which actually has a higher mean pinhole spacing than the rectangular one, shows higher sidelobes than the rectangular array: further demonstration of the possible benefits of rectangular arrays.

5.6 Conclusions

We have examined the optical sectioning behaviour of a coherent source DVM in detail. It was shown that it is possible to decrease the FWHM of the depth response below that of the single pinhole limit by using the appropriate closely spaced pinhole array. By examining 1-D arrays and using a simple ray optics model, we showed that this effect was linked to the phenomenon of destructive interference which can result when reflected light cones from neighbouring pinholes overlap. This is an important effect which we believe has not previously been reported and suggests that the use of a

scanned small group of pinholes could be useful in the imaging of the surface topography of, for example, semiconductor devices. We witnessed a decrease in the FWHM of $\sim 10\%$ by employing a pinhole array consisting of 1×2 pinholes. If the group of pinholes covers a sufficiently small area of the sample ($\sim 1.2\mu$m) in the case of the previously mentioned array in our setup then the tilt of the sample would have little effect on the depth response and it would appear as predicted by theory.

We next examined 2-D arrays and witnessed similar effects taking place; we also noticed vastly enhanced sidelobe strengths in the depth response. This was traced to the inherent symmetry of the square array. Further, this fact suggested that pinhole arrays consisting of irregularly spaced pinholes could outperform the symmetrically spaced arrays which are now commonly in use. This discovery is particularly important in light of the development of the programmable array microscope (PAM) [67, 51, 64, 63] which is essentially a DVM which comprises a programmable pinhole array. We showed that, in coherent source DVMs employing square arrays of pinholes the sidelobe level of the depth response has no upper limit, in contrast to what is the case in incoherent source DVMs. We presented, for the first time, an equation which describes the depth response of a coherent source DVM which employs an infinite array of pinholes. This is a computationally efficient equation which also gives insight into the behaviour of finite array DVMs, and which can predict, for example, the axial range which can be safely used in **any** coherent source DVM without encountering the most troublesome principal sidelobes.

As a particular example of the benefits obtainable with irregularly spaced arrays, rectangular and square arrays were compared: rectangular arrays were found to outperform square arrays in the finite array case. In the infinite array case of rectangular pinhole arrays, we showed that a suppression of the principal sidelobes is achieved by prudent choice of pinhole spacing.

A direct comparison of incoherent and coherent source DVMs showed that the use of coherent sources, from an optical sectioning point of view, is likely to significantly degrade imaging unless the inter-pinhole spacing is increased significantly. We found

that $m_s \geq 15$ were likely to be required to ensure no significant degradation of imaging. This is in contrast to a corresponding figure of $m_s \geq 5$ quoted by McCabe *et al.* [25] for incoherent source DVMs. In practice, factors such as sample tilt, sample surface relief, scattering of light by optical surfaces *etc.* ensures that features in a recorded image cannot always be directly correlated with the depth response. In reality, the depth responses we have presented are likely to represent a worst case scenario for the imaging and the limits we have imposed would be needlessly stringent however they do represent a useful guideline. The availability of high power laser sources will, to a large degree, offset the lower throughput of the pinhole array which is required.

Chapter 6

Variable focal length microlenses in confocal microscopy

Thus far, our investigations have centred on confocal imaging systems which are very similar in nature or behaviour to DVMs. We now divert course slightly to focus on an instrument which has many properties of the DVM but is inherently different in nature: the real-time confocal endoscope.

An array of microlenses with focal lengths that can be electrically varied can control the coupling of light into a single mode fibre using an applied voltage. We have examined this technology with a view to the design of a confocal microlens array/image-fibre endoscope. Coupling of light to the fibre was controlled by electrically driven variation of the focal length of the microlenses. We have examined the conditions which give maximum coupling to the fibre.

6.1 Introduction

Since the 1980s there has been an upsurge of interest in microlenses as the benefits of photonics over electronics have become realised. Applications for microlenses include [80]: image transfer, for example, in fax machines and photocopiers; coupling of light into the cores of optical fibres; switching applications in optical array interconnection;

and collimation of light from laser diodes. Most microlens manufacturers have settled for lithographic, ion exchange, or diamond point turning methods to form the lenses. All methods are capable of producing diffraction limited lenses although often over a restrictive range of diameters and focal lengths. The lenses can be further improved by using techniques such as ion-etching to form, for example, an aberration-corrected aspheric lens. The microlenses are often arranged in arrays, with arrays of specified size and spacing being custom-supplied by many manufacturers. The current most popular method of manufacturing microlenses is the photoresist 'melt and reflow' method [80] (see also Section 6.6). This process is both simple and low cost and the quality of microlenses produced is excellent. Recently, a novel form of high quality variable focal length microlens has become available [81] (see also Section 6.6). This chapter describes the application of such technology to a confocal endoscope.

6.2   Application of microlenses to confocal systems

Microlenses arrays are well-suited to and have found application in confocal imaging systems. The advantages offered by microlenses has been exploited, so far, in two main areas. The first is the application of microlens arrays to improving the field of view in surface profiling brightfield confocal microscopes. For example Tiziani *et al.* [82, 83] have exploited microlens array technology with a view to circumventing the usual trade-off in direct-view microscopes between the field of view and the lateral and axial resolution. Low magnification, low NA objective lenses allow the imaging of a large field of view on a sample whereas high magnification, high NA objectives offer much superior resolution but at the cost of an extremely limited field of view. In applications which require the imaging of fields of view which may be cm^2 microlens arrays can offer an improvement on this. The field of view is essentially determined by the number of microlenses in the array while the resolution is determined by the NA of each individual microlens within the array. Using microlenses with NAs of 0.26, Tiziani*et al.* [82] performed high resolution surface topography measurements over a

138

wide area of a sample.

Another advantage of microlens arrays which has been exploited successfully in direct-view microscopes centres on their ability to increase the light throughput of a Nipkow disc. A wavefront is prefocused by a microlens array to a 2-D array of focal spots which match the pitch and diameter of pinholes in a Nipkow disc. For example, (as discussed in Chapter 3) Tanaami *et al.* [44] have reported a system which offers an improvement in the light throughput of the disc from a typical value of $\sim 4\%$ [25] to $\sim 60\%$.

In multiphoton microscopy, microlenses have also been exploited to good effect. Such multiphoton systems are generally operated with pulsed lasers of extremely high peak power. In order to avoid the damage in the sample which would result from such intense illumination, traditionally a fraction of the total power output of the laser was used for imaging, the rest being discarded. Recently however, parallel-mode multiphoton systems [49, 45] have been reported which reduce wastage of light by employing an array of foci, so-called 'multifocal multiphoton' operation. As a means of generating the multiple focal points on the sample, microlens arrays are ideal having high optical throughput, unlike Nipkow discs, and high uniformity. Further, the multiphoton process in itself provides depth-discrimination: the need for a Nipkow disc pinhole array is removed. In the implementation of Egner *et al.* [49] the microlenses are arranged on a disc in Archimedean spirals so that rotating the disc images the field of view in real-time. Light passes the microlens array only on the illumination side, being sent directly towards a CCD camera on the detection side. Such systems have recently employed time-multiplexing whereby adjacent foci are time-delayed with respect to each other over durations longer than the pulse width so that crosstalk between foci is eliminated. An array of glass plates of appropriate thickness in front of the microlenses provides the necessary time delay.

In addition to the above, microlens arrays also show promising potential for use in the design of confocal endoscopes.

6.3 Application of microlens arrays to endoscopy

Confocal endoscopes generally employ a coherent optical fibre bundle to achieve remote confocal imaging. The fibre bundle is described as coherent in that individual fibres within the bundle are carefully arranged so that their end-points reside at the same co-ordinates on both ends of the bundle. This type of fibre bundle is often called an image fibre bundle because it is suitable for transferring optical images from place-to-place; image fibre bundles are very commonly used in medical endoscopy. Endoscopy, by its nature generally requires real-time imaging because the distal end of the endoscope is free to move around the object field.

A number of confocal endoscopes employing image fibre bundles have been implemented in recent years. For example, Gmitro and Aziz [84] have implemented a fluorescence imaging system in which a single focused spot is scanned across the proximal end of an image fibre bundle addressing each individual fibre in sequence. Light emerging from the distal end is collected by an objective and focused onto the object under inspection. Fluoresced light is collected by the fibre bundle and emerges at the proximal end to be directed towards a detector. The positioning of a pinhole of appropriate size in front of the detector ensures that only light from the individual fibre which had currently been addressed is detected. An optically sectioning image is the result. A similar system was described by Juškaitis *et al.* [85]. Rather than addressing fibres in the fibre bundle individually, they were addressed in parallel. This was achieved by the use of a Nipkow disc at the proximal end of the fibre bundle. Optically sectioned images were shown to result. More recently Sabharwal *et al.* [86] have described a confocal endoscope in which a slit was imaged onto the proximal end of an image fibre bundle. Light which traversed the fibre bundle, was reflected at a sample, coupled back into the fibre bundle and directed via a conjugate detector slit towards a detector. The slit was scanned by a flat mirror mounted on a galvanometer to give quasi real-time imaging which was confocal in the direction perpendicular to the slit.

We propose a system [87] which for the first time relies on the use of variable-focal-

length microlenses to selectively switch individual fibres within a fibre bundle and thus achieve confocality.

6.4 Variable-focus length microlens technology

As we will show, variable-focal length microlenses are a technology which open up many new avenues of research for confocal microscopy and endoscopy. Many variable-focal-length lens technologies have been disclosed which rely on many different (generally) electrical driven processes. Some, rely on changing the shape of the lens [88] (as in the human eye), for example adaptive spectacles have been marketed [89] which consist of a cell of stretchable plastic membrane which encloses a volume of liquid. The wearer pumps sufficient additional liquid into the cell so that the shape of the lens changes to correct for impairments in vision.

Other lenses rely on the use of electrically variable refractive index media; either in completely solid electro-optic materials (*e.g* $LiTaO_3$ [90]) or in liquid crystal materials [91]. Liquid crystal lenses offer greater NAs than solid electro-optic lenses however their response times can be slow depending on the square of the thickness [92] of the liquid crystal cell. This problem drove workers to investigate the operation of very small lenses in very thin liquid crystal cells, see for example Nose *et al.* [93] who used patterned electrodes to achieve a graded index liquid crystal microlens.

Another recent approach to the manufacture of variable-focal-length microlenses is the use of a physical microlens array in conjunction with a thin liquid crystal cell [88], microlens NAs of up to 0.15 are possible and switching speeds of $10 - 100$ms can be achieved by keeping the cell thin ($\sim< 5\mu$m) for a twisted nematic crystal cell.

141

6.4.1 Variable-focus microlenses in multifocal multiphoton microscopy

One example of a potential application for variable-focal-length microlens technology is in the implementation of a multiphoton multifocal (fluorescence) direct-view microscope. The microlenses could be arranged in Archimedean spirals (as in a Nipkow arrangement) on a disc. Fast spinning of the disc would allow real-time confocal imaging and different depths within the sample could be imaged by (electrically) varying the focal length of the microlenses: no scanning of the sample would be required. By initially overfilling the objective lens pupil, there would be no loss in resolution due to the change in NA of the microlenses as their focal length is varied. The loss of light caused by such an overfilling of the lens pupil would not be a major concern due to the almost limitless power available from the solid-state pulsed lasers typically used. In order to achieve tunable time-multiplexed operation, a thin liquid crystal cell with an array of patterned electrodes could be used. Such a cell would serve to apply an electrically controllable time delay between pulses emanating from adjacent microlenses.

6.4.2 Variable-focus microlenses for endoscopy

In a patent published in 2001 McCabe [87] has described the design of a confocal endoscope which employs a coherent fibre bundle in conjunction with an array of variable focal length microlenses. The idea is to associate each of an array of microlenses with an individual fibre within a fibre bundle. By using variable-focal-length microlens technology, light can be selectively coupled to designated fibres within the bundle. Because small-core fibres can be used in place of pinholes in confocal microscopes [94, 95, 96], parallelised confocal imaging will result. By electrically modulating the pattern of microlenses which are on and off across the surface of the image fibre real-time imaging will be possible.

6.5 Endoscope design using variable focal length microlenses

A simple design for a confocal endoscope system is depicted by Figure 6.1. Let us assume that the only light incident on the fibre bundle originates from the red microlens marked X. The individual fibre within the bundle which is addressed by this microlens is also indicated in red and marked with an X. We imagine that this individual fibre acts as a point-like source at the distal end of the fibre and serves to illuminate a point on a sample via an objective lens. When the sample is in the focal plane of the objective lens, most of the returned light enters the same fibre from whence it originated. Light returned from planes other than the focal plane of the objective will be defocused on the distal face of the image fibre and thus will be coupled into many fibres including the one from whence it originated. This light traverses the image fibre and is emitted in the backward direction towards the transfer lens. However, if we ensure that every microlens has a different focal length than microlens X, by using a transform lens and a spatial filter we can eliminate all but the light from microlens X and thus fibre X. In this way we can achieve remote optically sectioned images. The microlenses can be electrically switched in patterns similar to the situation in a PAM and the desired field of view on the sample can be imaged.

6.6 Device details

In order the realise the system described in Figure 6.1, we require an array of microlenses which can be individually addressed. Further, we require a means of altering the coupling efficiency between light emanating from the microlens and a fibre. One example of a technology which fulfils these criteria is variable-focal-length microlens technology based on a combination of photoresist lenses and a liquid crystal cell [81, 88, 97]. Such devices are constructed as follows: two substrates of Indium Tin Oxide (ITO) coated glass are first coated with Polyvinyl Alcohol and rubbed with a
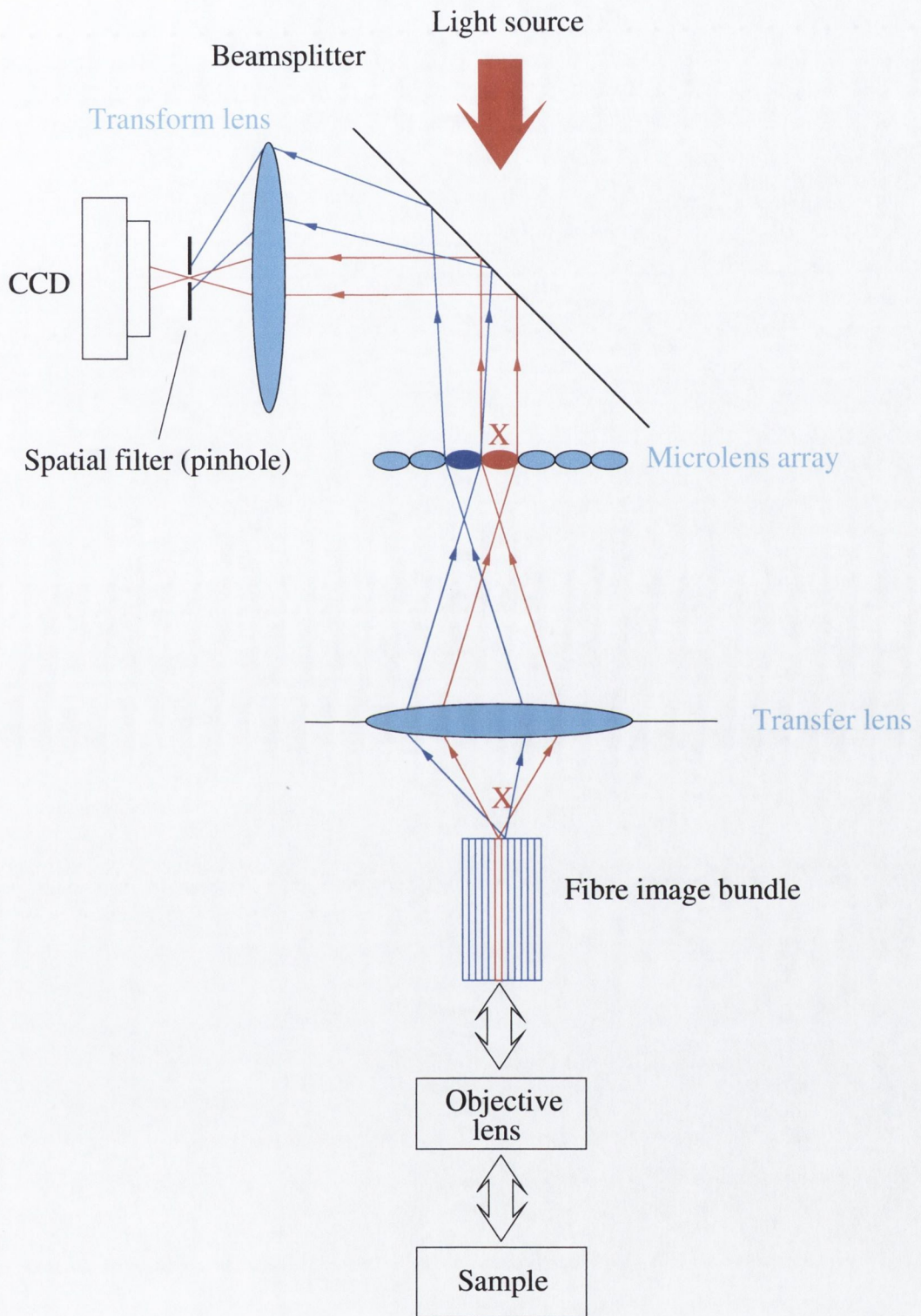
Figure 6.1: Basis for a confocal endoscope employing variable-focal-length microlenses.

144

cloth. This procedure ensures that a liquid crystal cell formed by the two substrates (with rubbing directions anti-parallel) will contain well ordered liquid crystal molecules with a small pre-tilt relative to both substrates. The pre-tilt is required as it ensures that, on application of a voltage, the crystal directors will all rotate in the same sense giving high uniformity. Before constructing the cell, one of the substrates is spin-coated with a layer of positive photoresist[1] which is then exposed through a mask so that there remain islands of photoresist where there was chrome on the mask. The photoresist is then baked so that it melts and is shaped by surface tension. In the case of circular islands the melted photoresist forms sections of a sphere. The thus-formed microlenses are coated with a thin layer of chromium so that electrical contact can be maintained along the surfaces of the microlenses as well as between them (ITO electrode). The cell is constructed by placing the microlens array facing the second ITO-coated glass slide and clamping both in place with 27μm Mylar blocks used as separators. Capillary action is used to fill the cell with nematic liquid crystal which has positive dielectric anisotropy[2] and sealed with UV curable glue.

For light passing through the cell, lensing occurs at the curved photoresist/liquid crystal interface. A voltage applied across the cell electrically switches the liquid crystal; this effectively varies its refractive index for light polarised in parallel with the liquid crystal alignment. The refractive index of the photoresist is 1.64 and the extraordinary refractive index of the liquid crystal can be modulated between 1.74 and 1.52 by the application of a voltage. Hence, the microlens array/liquid crystal cell has a tuneable focal length from a negative (diverging) region at 0V, to positive at around 1.6V, to a smoothly varying range of positive focal lengths for voltages above 1.6V. The voltage is applied to the transparent electrodes deposited on the inside cell surfaces, and the effect on transmitted (polarised) light is as shown in Figure 6.2.

The microlens array we used is a square array of 10×10 microlenses with diameters of 200μm. The focal length of similarly-made 150μm lenses is known from previous work

---

[1] Areas of the photoresist which are exposed to light are removed.
[2] The liquid crystal molecules orientate parallel to an applied electric field
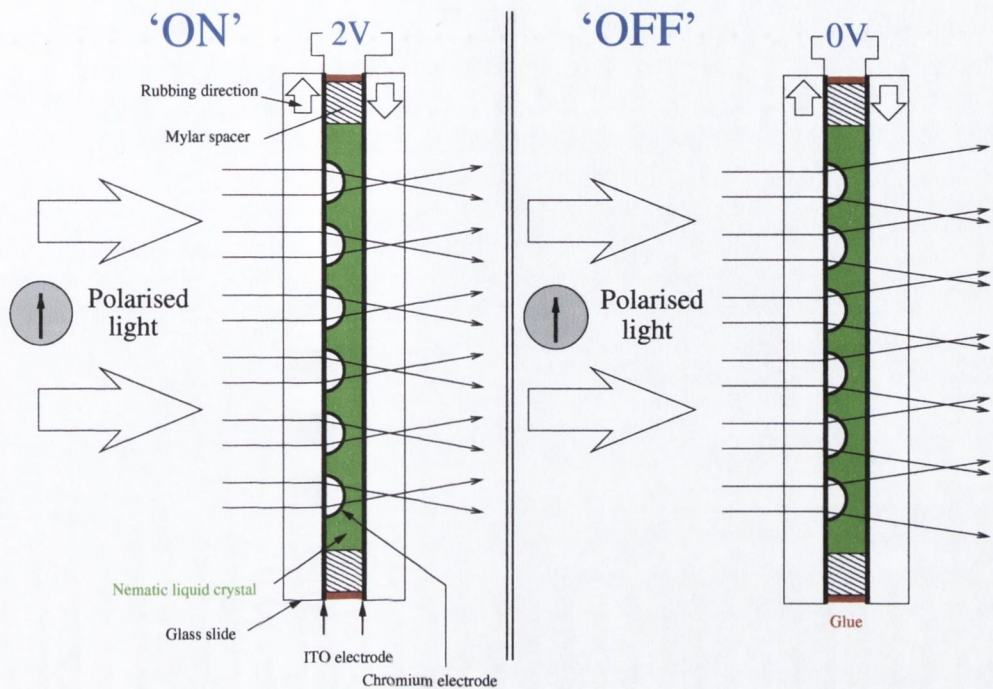
Figure 6.2: The structure of the microlens array/liquid crystal cell.

[98] to be -1570μm at zero applied voltage, to change from negative to positive focal length at 1.6V, and then to reduce monotonically from 3340μm at 2V to 1445μm at 8V giving a focal length variation in the positive region of 1895μm. The focal lengths were measured from the interface between the glass and the photoresist microlens.

6.7 Test system

In order to test the feasibility of our novel design we performed some preliminary experiments to evaluate the coupling from the microlenses previously described, into a single optical fibre. The system shown in Figure 6.3 was used for this purpose. A collimated, plane-polarised Ar^+ laser beam at 457.9nm was used to illuminate an area of the liquid crystal cell containing the microlens array. When a voltage above the 1.6V diverging-to-converging transition voltage is applied across the cell the microlenses focus the incident light to an array of foci. In the cell used, the focal lengths were such

146
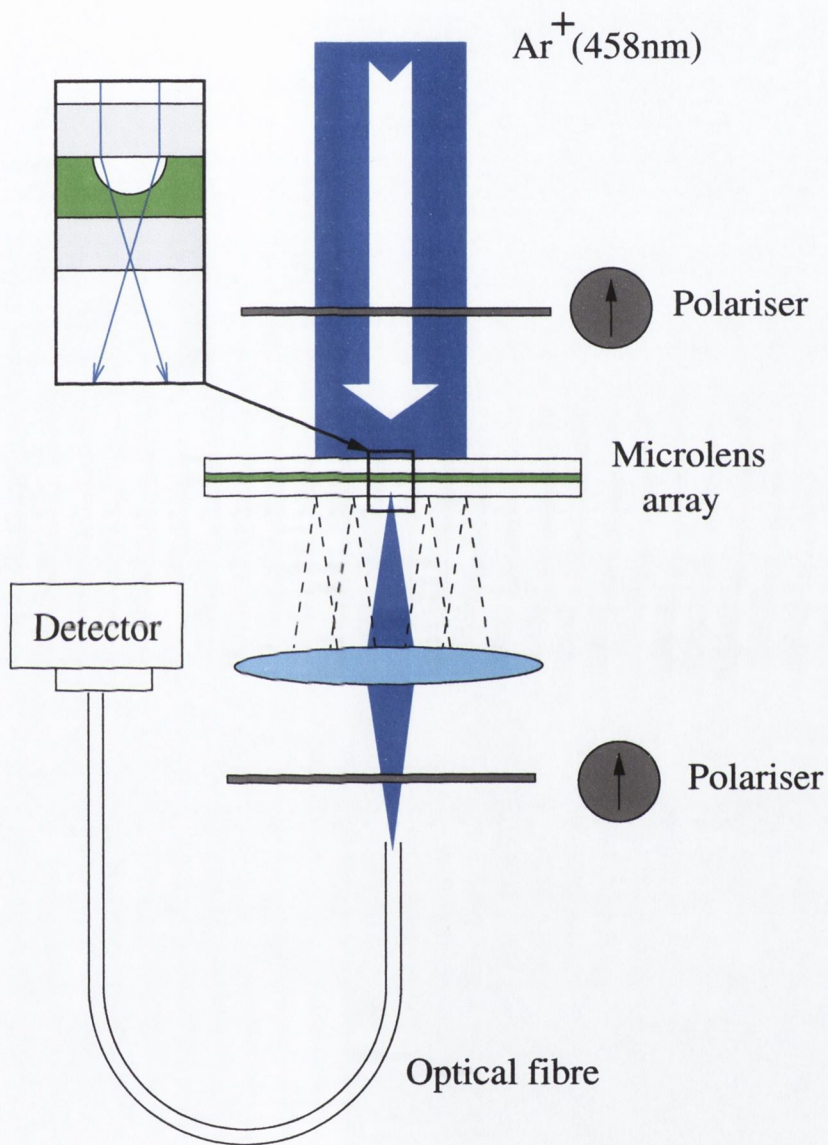
Figure 6.3: The microlens/fibre coupling test system.
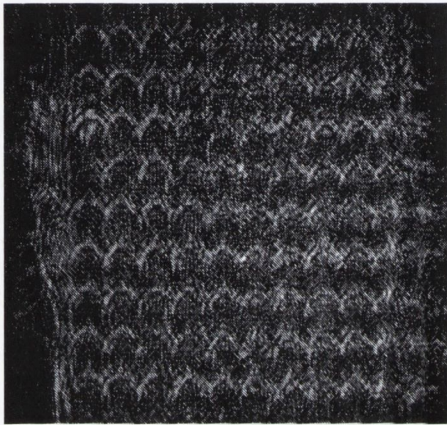
(a)
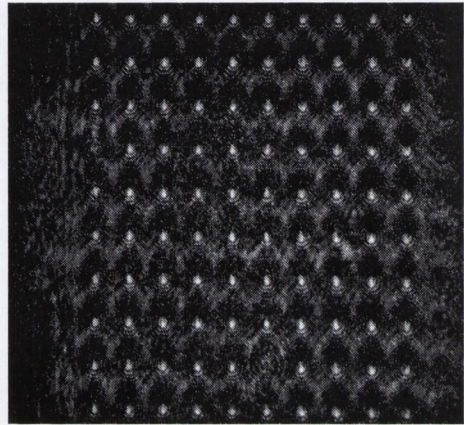
(b)
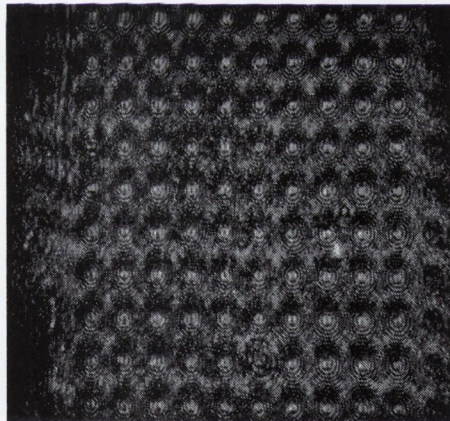
(c)

Figure 6.4: Photographs showing the microlens array output for diverging and converging modes. (a) Taken at 1V, with lenses diverging; (b) taken at 2.25V, with lenses focused; and (c) taken at 3V, with lenses defocused.

that these foci lay inside of one of the 1.1mm thick enclosing glass plates. As we wished to observe coupling for some distance, either side of the foci, along the optical axis, it was necessary to relay the foci to a more convenient position in free space. The diverging light from the foci was captured by a microscope objective and re-focused to form an array of focal spots in a plane containing a CCD camera where the images shown in Figure 6.4 were recorded. The three parts of the figure represent images taken for different voltages across the microlens array cell. The voltage was initially set to $2.25V$ and the objective lens was moved until the foci of the microlenses appeared as an array of tightly focused spots, see Figure 6.4 (b). With the CCD camera and objective lens in the same position, the voltage was set to $1V$ (Figure 6.4 (a)) and $3V$ (Figure 6.4 (c)) and images were again recorded. Comparison of parts (a) and (c) of
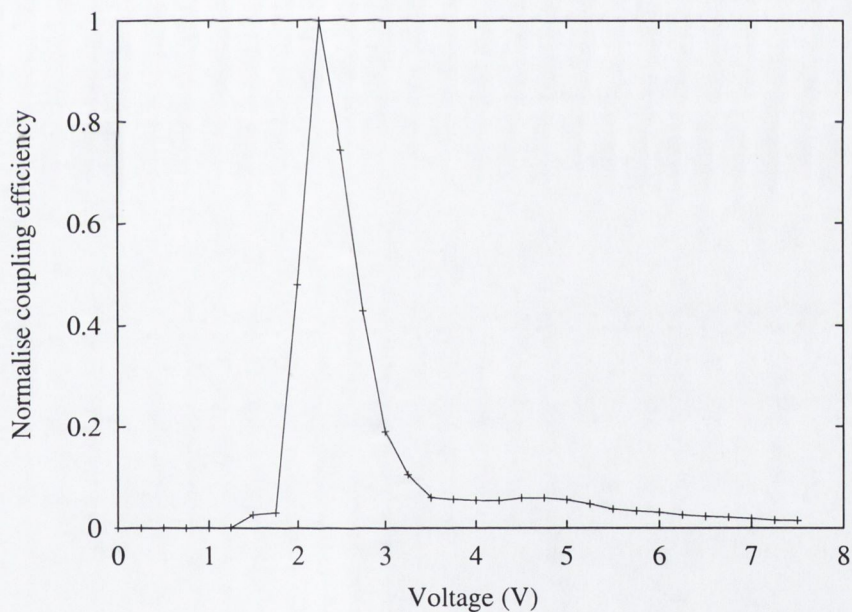
Figure 6.5: Coupling to a single mode fibre using variable focal length microlenses. Variation of the voltage across the microlens cell causes a change in the focal length and thus NA of the microlenses with the result that the coupling efficiency is altered as shown.

the figure with part (b) show a drop in light intensity at each of the foci due to the fact that the foci of the microlenses have been moved to different axial positions. In Figure

6.4 (b) the foci appear uniformly spaced and of uniform intensity. For this particular cell it was not possible to address each microlens individually. However our request for such an addressing system is in the process of being implemented by workers at UCL [88]. In order to test coupling efficiencies, a single-mode (at 457.9nm) optical fibre was placed at one of the foci. The voltage across the cell was varied while the light output from the fibre was measured using a linear photodetector. An example of the coupling witnessed is shown in Figure 6.5. For this particular axial location of the fibre, highest coupling occurred at $\sim 2.25V$; the curve shows a FWHM of $\sim 1V$. The fall-off in coupling efficiency is more rapid towards smaller voltages (across the diverging to converging transition of the microlenses). This is due to the fact the NA of the individual microlenses becomes larger at lower voltages and so the effective spot size at the fibre core is greater than would be expected for foci the other side of the coupling curve. The figure suggests that the voltage range from $1V \rightarrow 2.25V$ would be most suitable for switching of the fibres within an image fibre bundle. In order to further test the feasibility of this technology for use in a confocal endoscope it would be necessary to use individually addressable microlenses for coupling to an image fibre.

6.8 Design improvements

In order to reduce the levels of background light further, a system similar to that depicted by Figure 6.6 could be employed. The inclusion of two additional microlens arrays in the systems ensures that the only light incident on the microlens array nearest the fibre bundle, is incident on microlenses which are designated 'ON'. This is achieved by switching all three microlens arrays in synchronism and using a spatial filter in the transform plane of the second microlens. This spatial filter acts as a source/detector pinhole and should ensure that the background light reaching the detector is much diminished.
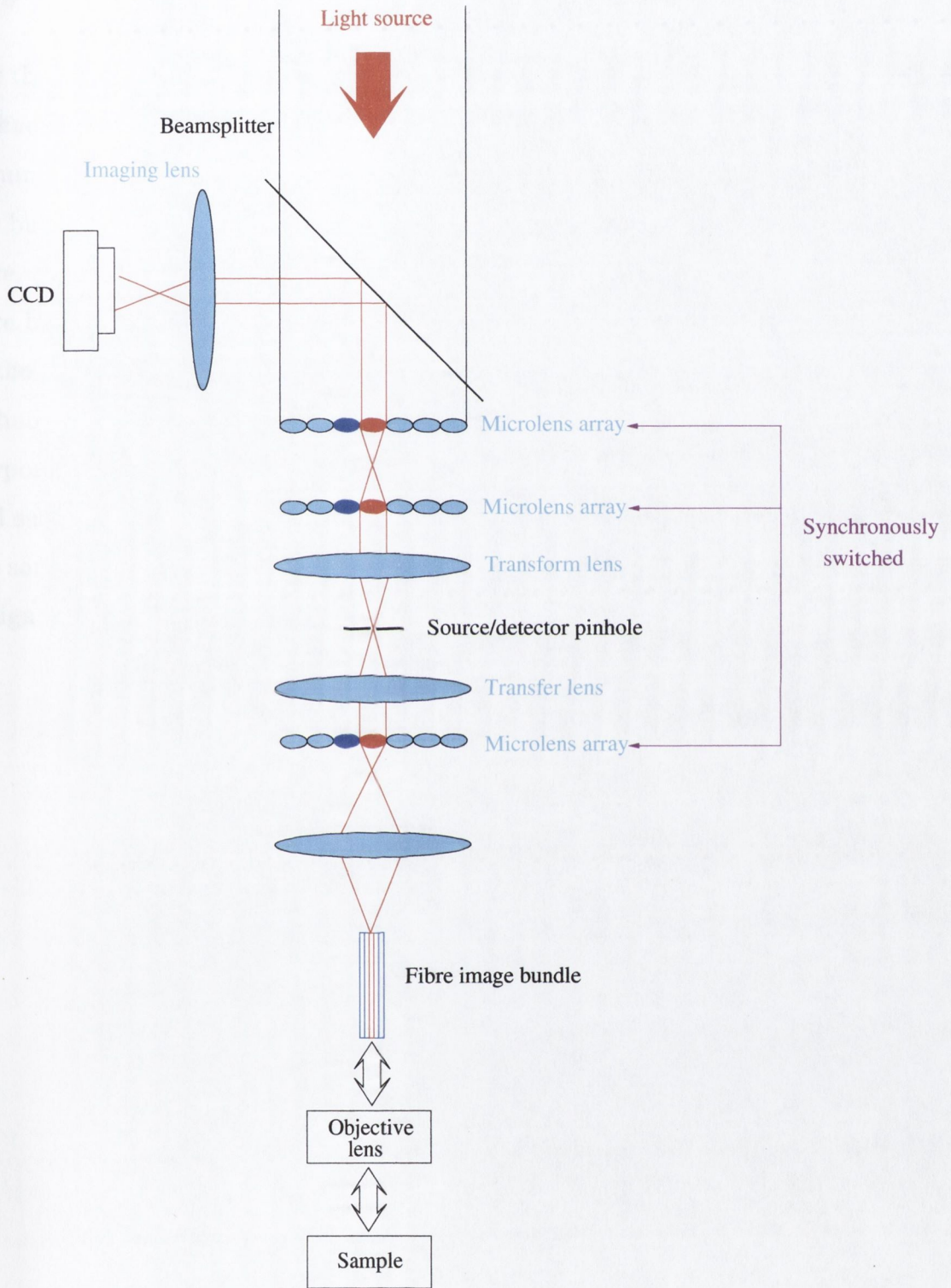
Figure 6.6: The structure of the microlens array/ liquid crystal cell.

6.9   Conclusions

For the first time we have performed an examination of variable-focal-length microlens technology with a view to implementation of a confocal endoscope. Such an endoscope requires addressing of an array of individual fibres within a fibre bundle. Each fibre in the bundle would be associated with a microlens which would control coupling to that fibre. In this way, an array of microlens foci could be scanned across the end of the fibre bundle to achieve imaging with properties similar to a DVM. With fast scanning of the foci, real-time imaging could be possible. Our, preliminary investigation of the technology suggests that the coupling efficiencies we have achieved are adequate for our purpose. Some outstanding issues remain however. For example, the implementation will suffer from a high background level in the depth response unless the microlens in the source plane can be illuminated independently. We have given details of a possible design improvement which would overcome this problem.

Chapter 7

Conclusions

In conclusion, we have performed a study of depth sectioning in direct-view microscope-like systems. The work, in large part, concentrated on the effects of source coherence on the depth-sectioning in such imaging systems.

The motivation for the work centres on the improved throughput of the Nipkow disc offered by the use of coherent (laser) light sources. Such sources as well as having high brightness are well suited to use in DVMs because of their high directionality and uniform nature. In the case of fluorescence-mode DVMs the narrow linewidth of a laser source has the further advantage that efficient excitation of the fluorophore is possible without the need for wasteful spectral filters.

We began by introducing the well-accepted theory which is often used to describe the imaging of confocal imaging systems. In particular, it was demonstrated how this theory has, in the past, been applied to the confocal microscope. This scalar and paraxial theory predicts both a lateral resolution and depth resolution enhancement for the confocal microscope, both of which have been verified by many workers by experiment. We required expressions describing the optical sectioning strength of various direct-view microscope configurations. *i.e.* those using both coherent and incoherent sources and operating in brightfield (reflection) and fluorescence mode. It was demonstrated how such equations are commonly derived from the DVM's optical transfer function.

In Chapter 3, we concentrated on the depth sectioning properties of the fluorescence-

mode DVM. We performed an experimental examination of the predictions of scalar diffraction theory with regard to source coherence in fluorescence-mode direct-view microscopy. For the first time, the experimental depth responses of incoherent and coherent source F-DVMs were directly compared.

Due to the non-ideal nature of our fluorescent samples, it was necessary to adapt the usual equations using a further paraxial modification. This modification, due to its computationally intensive nature, was implemented on a parallel processor network and was found to adequately describe the imaging trends witnessed by experiment. The experimental data showed that, in the case of the particular pinhole arrays examined in the experiment, the incoherent source F-DVM was found to have superior depth resolution than that employing a coherent source. Further theoretical analysis allowed us to show that there are two important effects to be considered when choosing a pinhole array which is appropriate for operation with a coherent source. The first effect was related to the diameter of the pinholes and the second was related to the spacing between pinholes. Inappropriate choice of these parameters was shown to have serious consequences for coherent source depth sectioning.

With regard to these two effects, we presented two guideline figures of merit which should be adhered to in practical F-DVMs in order to ensure that the use of a coherent source does not inhibit resolution. We first detailed a critical cut-off point for the pinhole radius above which it was shown that coherent source F-DVMs suffer from inferior depth resolution to their incoherent source counterparts. Secondly, we showed that, for a truly versatile F-DVM, the spacing between pinholes should be set at 20 times the pinhole radius. This guideline is consistent with one presented in the literature for lateral resolution. The two together, if adhered to, will ensure that the use of a coherent source in a F-DVM will not result in a loss of resolution and the benefits of laser sources, the foremost of which is superior light throughput of the Nipkow disc, can thus be accrued.

Turning our investigations to brightfield or reflection-mode DVMs, we began Chapter 4 by introducing a novel design for a coherent source programmable array microscope

154

which uses a pair of ferroelectric liquid crystal spatial light modulators to achieve versatile confocal imaging. We first investigated the effect of square apertures as opposed to the circular apertures which are commonly used. It was shown that closely spaced square apertures give rise to smaller sidelobes in the depth response than equivalent circular apertures. The effect was shown to become less significant as the aperture spacing is increased. This fact suggests that the computationally efficient equations describing the behaviour of circular aperture DVMs could be used to describe the main trends of the depth imaging in practical PAMs which employ square apertures. We then introduced some limitations of our PAM system and imaging artifacts which we encountered before moving on to present experimental depth responses.

In general, it was found that recorded depth responses were unpredictable in nature due to the fact that they result from interference across a spatially coherent optical wavefront. Any tilts or aberrations in the system could affect the degree of coherence and change the nature of the depth response. We examined the likely effects of aberration on the depth imaging and, in particular, showed some effects of spherical aberration. This study suggested the presence of minimal spherical aberration in our system. The discrepancy between theoretical and experimental curves was related to our use of an inefficient shuttering system. By supplementing a more efficient shutter to the design, the situation could be corrected.

With our PAM, it was possible to record quality confocal images and show some interesting effects of the source coherence. For example, an improvement in the depth resolution when the apertures of the array were spaced closely together. This improvement was also predicted by theory. We briefly investigated the application of aperture correlation to our system and presented an implementation for which the FLC technology is well-suited. The depth sectioning behaviour of aperture correlated arrays was found to be analogous to that of equivalent standard arrays.

The behaviour observed in the PAM system necessitated further theoretical investigation. We thus continued our analysis of coherent source brightfield direct-view microscopes, concentrating on the theoretical side. The increased depth resolution for

closely spaced apertures which was encountered in our coherent source PAM was related to destructive interference resulting from crosstalk between adjacent apertures in the array. This novel effect suggests that small groups of closely spaced pinholes could be used to achieve improved resolution in the imaging of wide-area reflecting samples, such as semiconductor structures. We performed a broad examination of the variation of the depth sectioning of coherent source DVMs with both the number of pinholes in the array and the spacing between them.

It was shown that the number of pinholes increases the height of sidelobes of the depth response, in the case of the most prominent sidelobes their level was found to approach the level of the in-focus peak itself. These prominent sidelobes were ascribed the label 'principal' sidelobe. Our derivation of an equation describing the depth response corresponding to the infinite pinhole array limit allowed to make other statements about the nature of coherent source brightfield imaging. For example we were able to predict the axial location of the principal sidelobes and show how the use of rectangular arrays can reduce them considerably. In fact, we demonstrated that prudent choice of the pinhole spacings in the x and y-directions of a rectangular array can lead to elimination of the principal sidelobes. We also presented an example of a finite rectangular array which exhibits superior optical sectioning to a square array of similar dimensions. Finally, we gave a guideline for the mark-space ratio which should be used in coherent source DVMs of > 15. This guideline is greater than that presented in the literature for lateral resolution and should serve as a limiting guideline in coherent source brightfield DVMs.

Finally, in Chapter 6 we presented a novel design for a confocal endoscope which employs variable-focal-length microlenses to individually address fibres within an image fibre bundle. A preliminary investigation of the technology was performed by using such microlenses to couple light to a single mode optical fibre. The technology shows promise but needs further development (individually addressable microlenses) before a final system can be successfully implemented.

In conclusion, the guidelines set down in this work for optimum pinhole array dimen-

sions are likely to permit quality parallelised confocal imaging with coherent sources, with concomitant advantages of higher throughput of the Nipkow disc.

7.1 Future work

7.1.1 Lateral resolution in fluorescence DVMs employing coherent and incoherent sources

An experimental investigation of the predictions of Fewer *et al.* [31] with regard to the behaviour of lateral resolution with source coherence should be performed. Specifically, the prediction that the lateral resolution is independent of source coherence when the pinhole spacing (in the object plane) is ≥ 20 optical units.

7.1.2 Variable-focus microlenses in multifocal multiphoton microscopy

In Chapter 6 we gave details of a system which could achieve real-time 3-D imaging. The system relies on the use of a spirally arranged variable-focal length microlens array with a multiphoton fluorescence microscope. The variable-focal length microlens technology detailed in Chapter 6 relies on a layer of nematic liquid crystal for its operation and could, in principle, be used in the above system. The success would depend on the magnitude of the perturbative effect that the lateral force caused by spinning the microlens array would have on the liquid crystal.

7.1.3 Variable-focus microlenses in confocal endoscopy

The next step in the study of Chapter 6 would be the realisation of an individually addressable variable-focal length microlens array. With such technology, the system detailed in Figure 6.6 could be constructed and could potentially offer high quality remote confocal imaging without the need for mechanical lateral scanning.

Appendix A

Relevant identities

A.1   The Dirac delta function

The Dirac delta function $\delta(x)$ may be defined by the following equations [1]:

$$\begin{cases} \delta(x) = 0, \quad x \neq 0 \\ \int_{-\infty}^{\infty} \delta(x)dx = 1. \end{cases} \tag{A.1}$$

Evidently, $\delta(x)$ is not a function in the ordinary mathematical sense, it is perhaps more appropriate to think of $\delta(x)$ as a quantity with a certain symbolic meaning. $\delta(x)$ has a useful sifting property [35]:

$$\int_{-\infty}^{\infty} f(y)\delta(x - y)dy = f(x). \tag{A.2}$$

For any function $f(y)$ and at each point of continuity of f. Also, with the notation FT[•] denoting a Fourier transform [35] we have:

$$\text{FT}[\delta(x)] = 1. \tag{A.3}$$

$\delta(x)$ can be employed to mathematically represent a point source.

A.2   Properties of the Fejér Kernel

The Fejér Kernel $\mathbf{F}_n(x)$ is defined:

$$\mathbf{F}_n(x) = \frac{\sin^2\left(\frac{(n+1)x}{2}\right)}{2(n+1)\sin^2(\frac{x}{2})}. \tag{A.4}$$

And has the following properties:

$$\mathbf{F}_n(x) = \mathbf{F}_n(-x), \tag{A.5}$$

and,

$$\mathbf{F}_n(x) = \mathbf{F}_n(x + 2m\pi), \tag{A.6}$$

for m an integer. Further, it can be shown [99] that, for any β chosen in the range
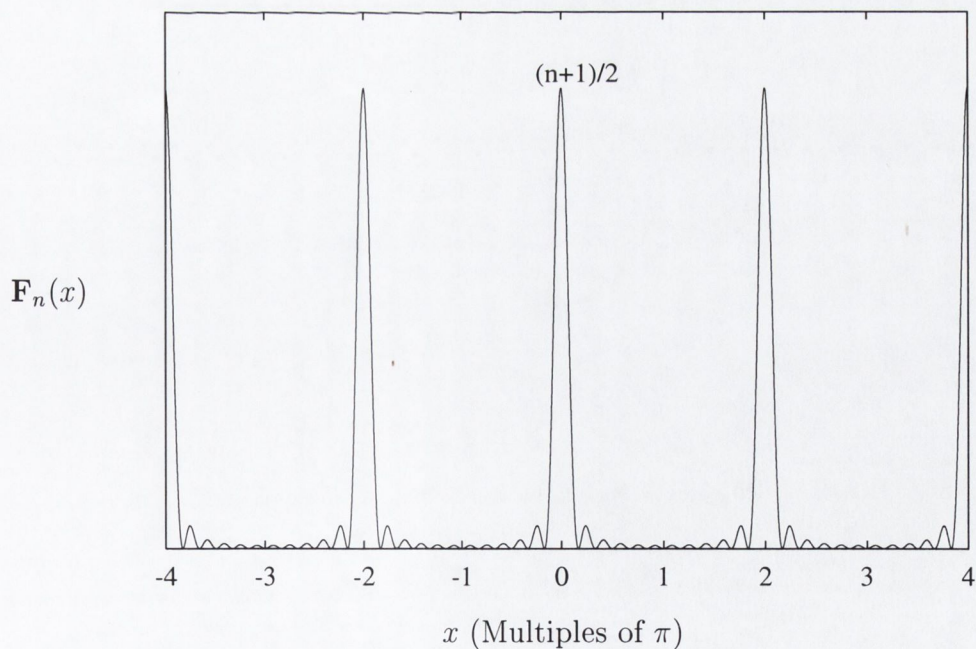
Figure A.1: The Fejér Kernel.

159

$0 < \beta < \pi$ then:

$$|\mathbf{F}_n(x)| \leq \frac{1}{2(n+1)\sin^2\left(\frac{\beta}{2}\right)}, \tag{A.7}$$

for $\beta \leq x \leq \pi$. Which converges uniformly to zero as $n \to \infty$. It now remains to see what happens at $x = 0$. Application of l'Hopital's rule [100] gives:

$$\lim_{x \to 0}\sqrt{\mathbf{F}_n(x)} = \lim_{x \to 0}\frac{\frac{(n+1)}{2}\cos\left(\frac{(n+1)x}{2}\right)}{\sqrt{2(n+1)}\frac{1}{2}\cos\left(\frac{x}{2}\right)} = \sqrt{\frac{n+1}{2}}. \tag{A.8}$$

So we have:

$$\lim_{x \to 0}\mathbf{F}_n(x) = \frac{n+1}{2}. \tag{A.9}$$

Which approaches ∞ as $n \to \infty$. Using the additional property:

$$\int_{-\pi}^{\pi}\mathbf{F}_n(x)dx = \pi. \tag{A.10}$$

We can construct a function $\mathbf{F}'_n(x)$:

$$\mathbf{F}'_n(x) = \frac{1}{\pi}\mathbf{F}_n(x), \tag{A.11}$$

which has the properties of the δ function as $n \to \infty$. Because, $\mathbf{F}_n(x)$ has period 2π, we in fact have:

$$\lim_{n \to \infty}\mathbf{F}'_n(x) = \sum_{k=-\infty}^{\infty}\delta(x - 2\pi k), \tag{A.12}$$

k an integer.

A.3 A Bessel function identity

The following Bessel function identity [101] is used to perform angular integrations in the derivation of many of the equations in the thesis:

$$J_0(z) = \frac{1}{2\pi} \int_{-\pi}^{\pi} \exp\left(jz\sin\theta\right) d\theta, \tag{A.13}$$

with J_0 a zero order Bessel function of the 1st kind and $j = \sqrt{-1}$.

Appendix B

Selected derivations

B.1 Optical sectioning strength of coherent source brightfield DVM employing square apertures

Starting with Equations (2.42) & (4.5) and by introducing the Fourier transform of the detector array $F_{\overline{D}}$ via:

$$F_{\overline{D}}\left(\frac{\boldsymbol{\epsilon}-\boldsymbol{\epsilon}'}{M}\right) = F_D\left(\frac{\boldsymbol{\epsilon}'-\boldsymbol{\epsilon}}{M}\right) = \sum_{l=1}^{N} \exp\left(\frac{-j}{M}[\mathbf{T}_l.(\boldsymbol{\epsilon}'-\boldsymbol{\epsilon})]\right) F_{D_1}\left(\frac{\boldsymbol{\epsilon}'-\boldsymbol{\epsilon}}{M}\right). \quad \text{(B.1)}$$

With the individual detector aperture Fourier transform F_{D_1} given by:

$$F_{D_1}\left(\frac{\boldsymbol{\epsilon}'-\boldsymbol{\epsilon}}{M}\right) = \int D_1(\underline{\mathbf{t}}) \exp\left(\frac{-j}{M}[\underline{\mathbf{t}}.(\boldsymbol{\epsilon}'-\boldsymbol{\epsilon})]\right) d^2\underline{\mathbf{t}}. \quad \text{(B.2)}$$

Assuming equal lenses, we may write:

$$\int D_1(\underline{\mathbf{t}}) \left| \int F_{S_{1A}}\left(\frac{\boldsymbol{\epsilon}}{M}\right) P(2u,\boldsymbol{\epsilon}) \sum_{l=1}^{N}\sum_{i=1}^{N} \exp\left(\frac{-j}{M}[\boldsymbol{\epsilon}.(\underline{\mathbf{T}}_i - \underline{\mathbf{T}}_l - \underline{\mathbf{t}})]\right) d^2\boldsymbol{\epsilon} \right|^2 d^2\underline{\mathbf{t}}. \quad \text{(B.3)}$$

We now, for a moment, concentrate on the summation terms in the innermost integration. We re-express the aperture co-ordinates $\underline{\mathbf{T}}_i$, $\underline{\mathbf{T}}_l$ in terms of the aperture spacing

R via:

$$\underline{\mathbf{T}}_i = (kR, lR) \qquad k, l = 1, 2, \ldots, n$$

$$\underline{\mathbf{T}}_l = (k'R, l'R) \qquad k', l' = 1, 2, \ldots, n. \tag{B.4}$$

For an array of $n \times n = N$ apertures. By letting $\underline{\boldsymbol{\epsilon}} = (\epsilon_1, \epsilon_2)$ we may express the summation terms as:

$$\sum_{k=1}^{n} \sum_{l=1}^{n} \sum_{k'=1}^{n} \sum_{l'=1}^{n} \exp\left(\frac{-jR}{M}[\epsilon_1(k - k') + \epsilon_2(l - l')]\right)$$

$$= \left|\sum_{k=1}^{n} \exp\left(\frac{-jR\epsilon_1 k}{M}\right)\right|^2 \left|\sum_{l=1}^{n} \exp\left(\frac{-jR\epsilon_2 l}{M}\right)\right|^2$$

$$= \left[\frac{\sin^2\left(\frac{\epsilon_1 Rn}{2M}\right)}{\sin^2\left(\frac{\epsilon_1 R}{2M}\right)}\right] \left[\frac{\sin^2\left(\frac{\epsilon_2 Rn}{2M}\right)}{\sin^2\left(\frac{\epsilon_2 R}{2M}\right)}\right]. \tag{B.5}$$

Substitution of this result back into Equation (B.3) gives:

$$I_{\text{PLANE}}(u) = \int\int D_1(t, w) \left| \int\int F_{S_{1A}}\left(\frac{\epsilon_1}{M}, \frac{\epsilon_2}{M}\right) P(2u, \epsilon_1, \epsilon_2) \right.$$

$$\times \left[\frac{\sin^2\left(\frac{\epsilon_1 Rn}{2M}\right)}{\sin^2\left(\frac{\epsilon_1 R}{2M}\right)}\right] \left[\frac{\sin^2\left(\frac{\epsilon_2 Rn}{2M}\right)}{\sin^2\left(\frac{\epsilon_2 R}{2M}\right)}\right]$$

$$\left. \times \exp\left(\frac{j}{M}[\epsilon_1 t + \epsilon_2 w]\right) d\epsilon_1 d\epsilon_2 \right|^2 dt dw. \tag{B.6}$$

With $\underline{\mathbf{t}} = (t, w)$. Because of the circular cut-off of the Pupil function P, it is convenient to express the innermost integral in polar form. With the substitutions $(\epsilon_1, \epsilon_2) = (\rho \cos \phi, \rho \sin \phi)$ and $d\epsilon_1 d\epsilon_2 = \rho d\rho d\phi$ we arrive at Equation (4.5).

B.2 Infinite array limit

In order to derive the infinite array limit of the planar object response of Equation (B.6) we concentrate on the sine terms in the innermost integration. From Equation

(A.4) we have:

$$\left[\frac{\sin^2\left(\frac{\epsilon_1 Rn}{2M}\right)}{\sin^2\left(\frac{\epsilon_1 R}{2M}\right)}\right]\left[\frac{\sin^2\left(\frac{\epsilon_2 Rn}{2M}\right)}{\sin^2\left(\frac{\epsilon_2 R}{2M}\right)}\right] = 4n^2 \mathbf{F}_{n-1}\left(\frac{\epsilon_1 R}{M}\right)\mathbf{F}_{n-1}\left(\frac{\epsilon_2 R}{M}\right). \tag{B.7}$$

For an infinite array, we let $n \to \infty$ in which case Equation (A.12) allows us to write:

$$\lim_{n\to\infty} I_{\text{PLANE}}(u) = \int\int D_1(t,w)\left|\sum_{k=-\infty}^{+\infty}\sum_{l=-\infty}^{+\infty}F_{S_{1A}}\left(\frac{2\pi k}{R},\frac{2\pi l}{R}\right)\right.$$
$$\times P\left(2u,\frac{2\pi kM}{R},\frac{2\pi lM}{R}\right)\exp\left(\frac{2\pi j}{R}[kt+lw]\right)\Bigg|^2 dtdw. \tag{B.8}$$

Where we have dropped all premultiplying constants. Cut-off of the pupil function P gives the following requirement for k, l:

$$k^2 + l^2 \leq \left(\frac{R}{2M\pi}\right)^2. \tag{B.9}$$

B.3 Counting pairs

If k and l are integers which run through a range delimited by $\pm k_{max}$. Such that each of k and l is a member of the set:

$$\{-k_{max}, -k_{max}+1, \ldots, -1, 0, 1, \ldots, k_{max}-1, k_{max}\} \tag{B.10}$$

Then as the summation of Equation (B.8) runs through successive values of k and l we can predict whether the term $k^2 + l^2$ will be odd or even as follows:

- $k^2 + l^2$ even $\Leftrightarrow$ both k, l are even **or** both k, l are odd.

- $k^2 + l^2$ odd $\Leftrightarrow$ either k is even and l is odd **or** k is odd and l is even.

There are two cases to consider:

- Case A: k_{max} is even.

- Case B: k_{max} is odd.

B.3.1 Case A

If k_{max} is even there are a total of $k_{max} + 1$ even numbers in the set and a total of k_{max} odd numbers. Thus, following the criteria outlined above, we can ensure that $k^2 + l^2$ is even by pairing even numbers, a total of $(k_{max} + 1)^2$ pairs. Alternatively, we can ensure that $k^2 + l^2$ is even by pairing odd numbers, a total of $(k_{max})^2$ pairs. We thus have a total of $(k_{max} + 1)^2 + (k_{max})^2$ pairs which give an even number for $k^2 + l^2$. The total number of pairs available is $(2k_{max} + 1)^2$ and so the number of pairs which give an odd value for $k^2 + l^2$ is $2k_{max}(k_{max} + 1)$. Overall $k^2 + l^2$ is even exactly once more than it is odd.

B.3.2 Case B

If k_{max} is odd it is straightforward to show in the same way that again $k^2 + l^2$ is even exactly once more than it is odd.

Appendix C

Sample MPI source code

The source code which implements the theory described in Chapter 3 which accounts for finite film thickness measurements of the depth response. Coherent source case.

```c
/* MPI-adapted version of coherent cource F_DVM (optical sectioning)C program (modified to take into
   account finite sample thickness) .                                    */

/* HEADERS */

#include <stdio.h>
#include <math.h>
#include "complex.h"
#include <mpi.h>
#include <stdlib.h>
#include <string.h>

/* MACROS */

#define SQR(a) ((a)*(a))

/* PARAMS */

#define I complex(0.0, 1.0)
#define NPTS 41
#define UMAX 40.0

/* MPI stuff */
#define REPORT_TAG 101
#define RESULT_TAG_RESULT 102
#define RESULT_TAG_INDEX 103
#define  ORDER_TAG 104
#define  KILL_PROC 0

/* BETA is ratio of fluorescence wavelength to exitation wavelength
   For 458nm exitation, 540nm fluorescence, BETA = 1.18 */

#define beta 1.18
#define U_OFFSET 0.0
```

```
#define NGAUSS_RHO_INT_A 74
#define NGAUSS_RHO_INT_B 74
#define NGAUSS_RHO_INT_C 74
#define NGAUSS_V_INT_A 76
#define NGAUSS_V_INT_B 76
#define NGAUSS_V_INT_C 76
#define NGAUSS_T 70
#define NGAUSS_W 70
#define NGAUSS_Z 20

/* GLOBALS
    +1 to allow for NR conventions */

char outputFilename[128];

double xGaussRho_INT_A[NGAUSS_RHO_INT_A+1], wGaussRho_INT_A[NGAUSS_RHO_INT_A+1];
double xGaussRho_INT_B[NGAUSS_RHO_INT_B+1], wGaussRho_INT_B[NGAUSS_RHO_INT_B+1];
double xGaussRho_INT_C[NGAUSS_RHO_INT_C+1], wGaussRho_INT_C[NGAUSS_RHO_INT_C+1];
double xGaussV_INT_A[NGAUSS_V_INT_A+1], wGaussV_INT_A[NGAUSS_V_INT_A+1];
double xGaussV_INT_B[NGAUSS_V_INT_B+1], wGaussV_INT_B[NGAUSS_V_INT_B+1];
double xGaussV_INT_C[NGAUSS_V_INT_C+1], wGaussV_INT_C[NGAUSS_V_INT_C+1];
double xGaussW[NGAUSS_W+1], wGaussW[NGAUSS_W+1];
double xGaussT[NGAUSS_T+1], wGaussT[NGAUSS_T+1];
double xGaussZ[NGAUSS_Z+1], wGaussZ[NGAUSS_Z+1];
double xV_INT_A[NGAUSS_V_INT_A+1];
double xV_INT_B[NGAUSS_V_INT_B+1];
double xV_INT_C[NGAUSS_V_INT_C+1];
double wV_INT_A[NGAUSS_V_INT_A+1];
double wV_INT_B[NGAUSS_V_INT_B+1];
double wV_INT_C[NGAUSS_V_INT_C+1];

complex factorbeta_INT_A[NGAUSS_RHO_INT_A+1][NPTS+1];
complex factorbeta_INT_B[NGAUSS_RHO_INT_B+1][NPTS+1];
complex factorbeta_INT_C[NGAUSS_RHO_INT_C+1][NPTS+1];
complex factor_INT_C[NGAUSS_RHO_INT_C+1][NPTS+1];

double vp;

/* FUNCTION PROTOTYPES */

void gauleg(float x1, float x2, double x[], double w[], int n);
float bessj0(float x);
float bessj1(float x);
complex h1(double,int);
complex h1beta_INT_A(double,int);
complex h1beta_INT_B(double,int);
complex h1beta_INT_C(double,int);
void nrerror(char*);
void initialise(int, double);
int master(int);
int slave(int, int);
double *dvector(long, long);
double Dconv(double,int);
 double pinholeFT(double, double);

/* main
    A harness which allocates the 'master' tasks to the root process
    and the 'slave' work to all the others, using MPI calls to establish
    which is which.
*/

int main(int argc, char **argv){

  int nproc, myid, rtn;
```

167

```c
  MPI_Init(&argc, &argv);
  MPI_Comm_size(MPI_COMM_WORLD, &nproc);
  MPI_Comm_rank(MPI_COMM_WORLD, &myid);

  if(myid == 0){
    /* run master tasks on process with rank=0 */
    rtn = master(nproc);
  }

  else{
    /* run slave program on all other processes */
    rtn = slave(nproc, myid);
  }
  MPI_Finalize();
  return(rtn);
}

/* MASTER: Dishes work to slaves. Receives results from slaves, dishes more
   work. Kills all slaves when there's no more work to do. */

int master(int nproc){
  int i, j, k,ind,d;
  double integralZ;
  double xSpacing, ySpacing,thickness;
  long xPts, yPts, totalPts, xTmp, yTmp;
  double result[NPTS+1],zout,u1;
  float ref_ind,lambda,NA,L;

  /* MPI stuff */

  MPI_Status report_status,result_status_result,result_status_index,order_status;
  int result_tag_result = RESULT_TAG_RESULT,
      result_tag_index = RESULT_TAG_INDEX,
      order_tag = ORDER_TAG,
      report_tag = REPORT_TAG,
      kill = KILL_PROC;


  char initFilename[128],data1[128]="all";
  FILE *initFile,*outputFile;
  double *xCoord, *yCoord, *r,maxCoord,minCoord;
  int slave_id;
  float Z_limit;
  float TMAX, WMAX, TMIN, WMIN;

  /* Ask user for filenames */

  printf("\n Enter filename containing initialisation data: \n");
  scanf("%s", initFilename);
  if((initFile = fopen(initFilename, "r")) == NULL){
    printf("error");
    exit(1);
  }

  printf("\n Enter filename of output file: \n");
  scanf("%s", outputFilename);

  /* Read params from file */

  fscanf(initFile, "%lf%*[^\n]%lf%*[^\n]", &xSpacing, &ySpacing);
  fscanf(initFile, "%ld%*[^\n]%ld%*[^\n]", &xPts, &yPts);
  fscanf(initFile, "%lf%*[^\n]", &vp);
  fscanf(initFile, "%lf%*[^\n]",&thickness);
  fclose(initFile);
```

168

```c
printf("\nAxial Resolution of a Thick Fluorescent Sample \n");
printf("\nx spacing: %lf\ty spacing: %lf\n", xSpacing, ySpacing);
printf("\t%ld by %ld array\n", xPts, yPts);
printf("pinhole radius: %lf\n\n", vp);
printf("film thickness(micr): %lf\n",thickness);

/* work out x and y Coords for TMAX and TMIN */

totalPts = xPts*yPts;
xCoord   = dvector(1, totalPts);
yCoord   = dvector(1, totalPts);
r        = dvector(1, totalPts);

/* x and y coords */

if (xPts%2 == 0) /* even no. of x points */
  xTmp = xPts/2;
else
  xTmp = (xPts+1)/2;

if (yPts%2 == 0) /* even no. of y points */
  yTmp = yPts/2;
else
  yTmp = (yPts+1)/2;

maxCoord=-1000.0;
minCoord=1000.0;
for (i=-xTmp; i<=-xTmp+xPts-1; i++){
  for (j=-yTmp; j<=-yTmp+yPts-1; j++){
    k = (i+xTmp)*yPts+j+yTmp+1; /* flatten x,y coords into 1D vector */
    xCoord[k] = i*xSpacing;
    yCoord[k] = j*ySpacing;
    if(xCoord[k]>maxCoord)maxCoord=xCoord[k];
    if(xCoord[k]<minCoord)minCoord=xCoord[k];
  }
}

TMAX=-minCoord+30.0;
TMIN=-maxCoord-30.0;

WMAX=TMAX;
WMIN=TMIN;
printf("WMIN= %f \n",WMIN);
printf("WMAX= %f \n",WMAX);

/* Set up the integration limits over which to integrate the thickness */
/* film refractive index */
ref_ind=1.61;

/* excitation wavelength */
lambda=457.9e-9;

/* numerical aperture of objective */
NA=0.6;

/* thickness in microns */
L=thickness;
Z_limit=8.0*M_PI*(L/2.0)*ref_ind*SQR(sin(asin(NA/ref_ind)/2.0))/lambda;
printf("Z_limit = %1.12lf \n",Z_limit);

/* set up arrays for integration stuff */
gauleg(0.0,1.0,xGaussRho_INT_A,wGaussRho_INT_A,NGAUSS_RHO_INT_A);
gauleg(0.0,1.0,xGaussRho_INT_B,wGaussRho_INT_B,NGAUSS_RHO_INT_B);
gauleg(0.0,1.0,xGaussRho_INT_C,wGaussRho_INT_C,NGAUSS_RHO_INT_C);
gauleg(0.0,1.0,xGaussV_INT_A,wGaussV_INT_A,NGAUSS_V_INT_A);
```

169

```
gauleg(0.0,1.0,xGaussV_INT_B,wGaussV_INT_B,NGAUSS_V_INT_B);
gauleg(0.0,1.0,xGaussV_INT_C,wGaussV_INT_C,NGAUSS_V_INT_C);
gauleg(TMIN,TMAX,xGaussT,wGaussT,NGAUSS_T);
gauleg(WMIN,WMAX,xGaussW,wGaussW,NGAUSS_W);
gauleg(-Z_limit,Z_limit,xGaussZ,wGaussZ,NGAUSS_Z);

/* Broadcast these arrays to all processes */

MPI_Bcast(&xGaussRho_INT_A, NGAUSS_RHO_INT_A+1, MPI_DOUBLE, 0, MPI_COMM_WORLD);
MPI_Bcast(&xGaussRho_INT_B, NGAUSS_RHO_INT_B+1, MPI_DOUBLE, 0, MPI_COMM_WORLD);
MPI_Bcast(&xGaussRho_INT_C, NGAUSS_RHO_INT_C+1, MPI_DOUBLE, 0, MPI_COMM_WORLD);
MPI_Bcast(&wGaussRho_INT_A, NGAUSS_RHO_INT_A+1, MPI_DOUBLE, 0, MPI_COMM_WORLD);
MPI_Bcast(&wGaussRho_INT_B, NGAUSS_RHO_INT_B+1, MPI_DOUBLE, 0, MPI_COMM_WORLD);
MPI_Bcast(&wGaussRho_INT_C, NGAUSS_RHO_INT_C+1, MPI_DOUBLE, 0, MPI_COMM_WORLD);
MPI_Bcast(&xGaussV_INT_A, NGAUSS_V_INT_A+1, MPI_DOUBLE, 0, MPI_COMM_WORLD);
MPI_Bcast(&xGaussV_INT_B, NGAUSS_V_INT_B+1, MPI_DOUBLE, 0, MPI_COMM_WORLD);
MPI_Bcast(&xGaussV_INT_C, NGAUSS_V_INT_C+1, MPI_DOUBLE, 0, MPI_COMM_WORLD);
MPI_Bcast(&wGaussV_INT_A, NGAUSS_V_INT_A+1, MPI_DOUBLE, 0, MPI_COMM_WORLD);
MPI_Bcast(&wGaussV_INT_B, NGAUSS_V_INT_B+1, MPI_DOUBLE, 0, MPI_COMM_WORLD);
MPI_Bcast(&wGaussV_INT_C, NGAUSS_V_INT_C+1, MPI_DOUBLE, 0, MPI_COMM_WORLD);
MPI_Bcast(&xGaussT, NGAUSS_T+1, MPI_DOUBLE, 0, MPI_COMM_WORLD);
MPI_Bcast(&wGaussT, NGAUSS_T+1, MPI_DOUBLE, 0, MPI_COMM_WORLD);
MPI_Bcast(&xGaussW, NGAUSS_W+1, MPI_DOUBLE, 0, MPI_COMM_WORLD);
MPI_Bcast(&wGaussW, NGAUSS_W+1, MPI_DOUBLE, 0, MPI_COMM_WORLD);
MPI_Bcast(&xGaussZ, NGAUSS_Z+1, MPI_DOUBLE, 0, MPI_COMM_WORLD);
MPI_Bcast(&wGaussZ, NGAUSS_Z+1, MPI_DOUBLE, 0, MPI_COMM_WORLD);


/* Broadcast array dimensions to all processes */
MPI_Bcast(&xSpacing, 1, MPI_DOUBLE, 0, MPI_COMM_WORLD);
MPI_Bcast(&ySpacing, 1, MPI_DOUBLE, 0 ,MPI_COMM_WORLD);
MPI_Bcast(&xPts, 1, MPI_LONG, 0, MPI_COMM_WORLD);
MPI_Bcast(&yPts, 1, MPI_LONG, 0, MPI_COMM_WORLD);
MPI_Bcast(&vp, 1, MPI_DOUBLE, 0, MPI_COMM_WORLD);
MPI_Bcast(&thickness, 1, MPI_DOUBLE, 0, MPI_COMM_WORLD);

/* Broadcast base for o/p filename */
MPI_Bcast(&outputFilename,128, MPI_CHAR, 0, MPI_COMM_WORLD);

/* start off all (nproc-1) slave procs */
for(i = 1; i <= (nproc-1); i++){
  /* send out value of i to all procs (each i corresponds to a different value
     of defocus)*/
  MPI_Send(&i, 1, MPI_INT, i, order_tag, MPI_COMM_WORLD);
}

/* serve slaves as necessary; kill them when no work remains */
for(i=nproc; i <= NPTS+(nproc-1); i++){
  /* look for report from anywhere */
  MPI_Recv(&slave_id, 1, MPI_INT, MPI_ANY_SOURCE, report_tag,
   MPI_COMM_WORLD, &report_status);
  /* receive result from same proc */
  MPI_Recv(&integralZ, 1, MPI_DOUBLE, slave_id, result_tag_result,
         MPI_COMM_WORLD, &result_status_result);
  /* receive index value from same proc */
  MPI_Recv(&ind, 1, MPI_INT, slave_id, result_tag_index,
   MPI_COMM_WORLD, &result_status_index);
  printf("i= %d \t integralZ= %lf \n",ind,integralZ);
  result[ind] = integralZ;
  if(i <= NPTS){ /* more work to do */
    /* send back new value of i to slave*/
    MPI_Send(&i, 1, MPI_INT, slave_id, order_tag,
     MPI_COMM_WORLD);
  }
  else{ /* no more jobs */
    /* send back kill signal to slave*/
```

```c
      MPI_Send(&kill, 1, MPI_INT, slave_id, order_tag,
        MPI_COMM_WORLD);
    }
  }

  /* write out results to file */

  if((outputFile = fopen(outputFilename, "wt")) == NULL){
    printf("error");
    exit(1);
  }

  for(i=1; i<=NPTS; i++){
    u1=(i-1)*UMAX/(NPTS-1);

    /* NOTE zout is expressed in microns */
    zout=u1*1.0e6*lambda/(8.0*M_PI*ref_ind*SQR(sin(asin(NA/ref_ind)/2.0)));

    fprintf(outputFile, "%1.12lf\t  %lf\n",zout, result[i]);
  }
  return(0);
}

/* slave
   Receives jobs from master, computes result (integralZ), sends result back
   to master and receives a new job if there are any left to do.
   When no jobs are left the slave receives a kill signal
   from the master and terminates.
*/


int slave(int nproc, int myid){

  complex innerSum, integralRho;
  double integralT, integralW;
  double integralZ;
  double sum,prod, exp;
  double *xCoord, *yCoord, *r;
  double xSpacing, ySpacing, thickness,u,u_z;
  long totalPts, xPts, yPts, xTmp, yTmp;
  long i, j, k, l, m, n,d,z;
  int p,going = 1;
  char data2[128],const_string[128];
  FILE  *outputFile;

  /* MPI stuff */
  MPI_Status report_status,result_status_index,result_status_result,order_status;
  int result_tag_result = RESULT_TAG_RESULT,
    result_tag_index = RESULT_TAG_INDEX,
    order_tag = ORDER_TAG,
    report_tag = REPORT_TAG,
    kill = KILL_PROC;

  printf("Hello from slave %d\n", myid);

  /* Get broadcast params from master */

  MPI_Bcast(&xGaussRho_INT_A, NGAUSS_RHO_INT_A+1, MPI_DOUBLE, 0, MPI_COMM_WORLD);
  MPI_Bcast(&xGaussRho_INT_B, NGAUSS_RHO_INT_B+1, MPI_DOUBLE, 0, MPI_COMM_WORLD);
  MPI_Bcast(&xGaussRho_INT_C, NGAUSS_RHO_INT_C+1, MPI_DOUBLE, 0, MPI_COMM_WORLD);
  MPI_Bcast(&wGaussRho_INT_A, NGAUSS_RHO_INT_A+1, MPI_DOUBLE, 0, MPI_COMM_WORLD);
  MPI_Bcast(&wGaussRho_INT_B, NGAUSS_RHO_INT_B+1, MPI_DOUBLE, 0, MPI_COMM_WORLD);
  MPI_Bcast(&wGaussRho_INT_C, NGAUSS_RHO_INT_C+1, MPI_DOUBLE, 0, MPI_COMM_WORLD);
  MPI_Bcast(&xGaussV_INT_A, NGAUSS_V_INT_A+1, MPI_DOUBLE, 0, MPI_COMM_WORLD);
  MPI_Bcast(&xGaussV_INT_B, NGAUSS_V_INT_B+1, MPI_DOUBLE, 0, MPI_COMM_WORLD);
```

```c
MPI_Bcast(&xGaussV_INT_C, NGAUSS_V_INT_C+1, MPI_DOUBLE, 0, MPI_COMM_WORLD);
MPI_Bcast(&wGaussV_INT_A, NGAUSS_V_INT_A+1, MPI_DOUBLE, 0, MPI_COMM_WORLD);
MPI_Bcast(&wGaussV_INT_B, NGAUSS_V_INT_B+1, MPI_DOUBLE, 0, MPI_COMM_WORLD);
MPI_Bcast(&wGaussV_INT_C, NGAUSS_V_INT_C+1, MPI_DOUBLE, 0, MPI_COMM_WORLD);
MPI_Bcast(&xGaussT, NGAUSS_T+1, MPI_DOUBLE, 0, MPI_COMM_WORLD);
MPI_Bcast(&wGaussT, NGAUSS_T+1, MPI_DOUBLE, 0, MPI_COMM_WORLD);
MPI_Bcast(&xGaussW, NGAUSS_W+1, MPI_DOUBLE, 0, MPI_COMM_WORLD);
MPI_Bcast(&wGaussW, NGAUSS_W+1, MPI_DOUBLE, 0, MPI_COMM_WORLD);
MPI_Bcast(&xGaussZ, NGAUSS_Z+1, MPI_DOUBLE, 0, MPI_COMM_WORLD);
MPI_Bcast(&wGaussZ, NGAUSS_Z+1, MPI_DOUBLE, 0, MPI_COMM_WORLD);
MPI_Bcast(&xSpacing, 1, MPI_DOUBLE, 0, MPI_COMM_WORLD);
MPI_Bcast(&ySpacing, 1, MPI_DOUBLE, 0, MPI_COMM_WORLD);
MPI_Bcast(&xPts, 1, MPI_LONG, 0, MPI_COMM_WORLD);
MPI_Bcast(&yPts, 1, MPI_LONG, 0, MPI_COMM_WORLD);
MPI_Bcast(&vp, 1, MPI_DOUBLE, 0, MPI_COMM_WORLD);
MPI_Bcast(&thickness, 1, MPI_DOUBLE, 0, MPI_COMM_WORLD);
MPI_Bcast(&outputFilename,128, MPI_CHAR, 0, MPI_COMM_WORLD);

/* Set up vectors */

totalPts = xPts*yPts;
xCoord   = dvector(1, totalPts);
yCoord   = dvector(1, totalPts);
r        = dvector(1, totalPts);

/* x and y coords */

if (xPts%2 == 0) /* even no. of x points */
  xTmp = xPts/2;
else
  xTmp = (xPts+1)/2;

if (yPts%2 == 0) /* even no. of y points */
  yTmp = yPts/2;
else
  yTmp = (yPts+1)/2;

for (i=-xTmp; i<=-xTmp+xPts-1; i++){
  for (j=-yTmp; j<=-yTmp+yPts-1; j++){
    k = (i+xTmp)*yPts+j+yTmp+1; /* flatten x,y coords into 1D vector */
    xCoord[k] = i*xSpacing;
    yCoord[k] = j*ySpacing;
    if(myid == 1) printf("xCoord= %lf \t yCoord= %lf \n",xCoord[k],yCoord[k]);
  }
}

for(d = 1; d <= 128; d++)  const_string[d]=outputFilename[d];

while(going){

/* receive i (defocus) on which to operate */
MPI_Recv(&i, 1, MPI_INT, 0, order_tag, MPI_COMM_WORLD, &order_status);

/* if i is a kill signal, kill the slave. */
if(i == KILL_PROC)  going = 0;


else{

  for(d = 1; d <= 128; d++) outputFilename[d]=const_string[d];
  /* work out defocus value on which to operate */
  u=(i-1)*UMAX/(NPTS-1);

  /* filename should contain the lowest value of u (in this set of points) */
  sprintf(data2,"%1.2lf",u);
```

```
    strcat(outputFilename,data2);

    /* "outputFilename" contains the filename*/

    integralZ = 0.0;
    for(z=1;z<=NGAUSS_Z;z++) {
      u_z=xGaussZ[z]-(u+U_OFFSET);

      /* set up the appropriate pupil function in a global array factor[NGAUSS_XXXX][NPTS+1] */

      initialise(i,u_z);
      integralT = 0.0;
      for(k=1; k<=NGAUSS_T; k++){
integralW = 0.0;
for(l=1; l<=NGAUSS_W; l++) {
  /* innersum is h1eff (Equation 3.8) */
  innerSum = Complex(0.0,0.0);
  for(m=1; m<=totalPts; m++){
    r[m] = sqrt(SQR(xGaussT[k]+xCoord[m]) + SQR(xGaussW[l]+yCoord[m]));
    integralRho=h1(r[m],i);
    innerSum = Cadd(innerSum,integralRho);
  }   /* end of m-loop */
  for(n=1;n<=totalPts;n++){
    /* sum is an array containing the integralRho's for the 2nd PSF */
    sum=Dconv(r[n],i);
    integralW += wGaussW[l] * Cabsqu(innerSum) * sum;
  }    /* end of n-loop */
}      /* end of l-loop */
integralT += wGaussT[k] * integralW;
      }  /* end of k-loop */
      integralZ += wGaussZ[z] * integralT;
    }    /* end of z-loop   */

    /* send back the results from this process to the master process */

    MPI_Send(&myid, 1, MPI_INT, 0, report_tag, MPI_COMM_WORLD);
    MPI_Send(&integralZ, 1, MPI_DOUBLE, 0, result_tag_result, MPI_COMM_WORLD);
    MPI_Send(&i, 1, MPI_INT, 0, result_tag_index, MPI_COMM_WORLD);
  }
  }
  return(0);
}



/* Fourier transform of individual pinhole */

double pinholeFT(double vp, double omega){
  double temp1;
  int v;

  if((temp1 = omega*vp) == 0.0)
    return 1.0;
  else
    return 2.0*bessj1(temp1)/temp1;
}


void initialise(int id, double u){
  int n,v;
  double temp1, temp2, temp3, temp4;

  for(n=1; n<=NGAUSS_RHO_INT_C; n++){
    temp1 = pinholeFT(vp, xGaussRho_INT_C[n]) * xGaussRho_INT_C[n] * wGaussRho_INT_C[n];
    temp4 = xGaussRho_INT_C[n] * wGaussRho_INT_C[n];
```

173

```
    temp2 = SQR(xGaussRho_INT_C[n]) * 0.5;
    temp3 = temp2/beta;

    factor_INT_C[n][id].r = temp1*cos(u* temp2);
    factor_INT_C[n][id].i = temp1*(-sin(u * temp2));
    factorbeta_INT_C[n][id].r = temp4*cos(u * temp3);
    factorbeta_INT_C[n][id].i = temp4*(-sin(u * temp3));
  }

  for(n=1; n<=NGAUSS_RHO_INT_A; n++){
    temp1 = pinholeFT(vp, xGaussRho_INT_A[n]) * xGaussRho_INT_A[n] * wGaussRho_INT_A[n];
    temp4 = xGaussRho_INT_A[n] * wGaussRho_INT_A[n];
    temp2 = SQR(xGaussRho_INT_A[n]) * 0.5;
    temp3 = temp2/beta;

    factorbeta_INT_A[n][id].r = temp4*cos(u * temp3);
    factorbeta_INT_A[n][id].i = temp4*(-sin(u * temp3));
  }

  for(n=1; n<=NGAUSS_RHO_INT_B; n++){
    temp1 = pinholeFT(vp, xGaussRho_INT_B[n]) * xGaussRho_INT_B[n] * wGaussRho_INT_B[n];
    temp4 = xGaussRho_INT_B[n] * wGaussRho_INT_B[n];
    temp2 = SQR(xGaussRho_INT_B[n]) * 0.5;
    temp3 = temp2/beta;

    factorbeta_INT_B[n][id].r = temp4*cos(u * temp3);
    factorbeta_INT_B[n][id].i = temp4*(-sin(u * temp3));
  }
}


complex h1(double t,int id){
  double temp;
  int i,n;
  complex integralRho;
  integralRho = Complex(0.0, 0.0);

  for(n=1; n<=NGAUSS_RHO_INT_C; n++){
    temp=bessj0(xGaussRho_INT_C[n]*t);
    integralRho.r += factor_INT_C[n][id].r*temp;
    integralRho.i += factor_INT_C[n][id].i*temp;
  }
  return(integralRho);
}

complex h1beta_INT_A(double t,int id){
  double temp;
  int i,n;
  complex integralRho;

  integralRho = Complex(0.0, 0.0);

  for(n=1; n<=NGAUSS_RHO_INT_A; n++){
    temp=bessj0(xGaussRho_INT_A[n]*t);
    integralRho.r += factorbeta_INT_A[n][id].r*temp;
    integralRho.i += factorbeta_INT_A[n][id].i*temp;
  }
  return(integralRho);
}

complex h1beta_INT_B(double t,int id){
  double temp;
  int i,n;
  complex integralRho;
```

174

```c
    integralRho = Complex(0.0, 0.0);

    for(n=1; n<=NGAUSS_RHO_INT_B; n++){
      temp=bessj0(xGaussRho_INT_B[n]*t);
      integralRho.r += factorbeta_INT_B[n][id].r*temp;
      integralRho.i += factorbeta_INT_B[n][id].i*temp;
    }
    return(integralRho);
}

complex h1beta_INT_C(double t,int id){
  double temp;
  int n;
  complex integralRho;

  integralRho = Complex(0.0, 0.0);

  for(n=1; n<=NGAUSS_RHO_INT_C; n++){
    temp=bessj0(xGaussRho_INT_C[n]*t);
    integralRho.r += factorbeta_INT_C[n][id].r*temp;
    integralRho.i += factorbeta_INT_C[n][id].i*temp;
  }
  return(integralRho);
}

/***************************************************/
/*    Convolution integral of Equation (3.7)       */
/*                                                 */
/*        To avoid multiple calls to               */
/*     gauleg we use the fact that we can          */
/*    scale from interval [0,1] to interval        */
/*    [a,b] by                                     */
/*              x -> a + x*(b-a)                    */
/*              W -> w*(b-a)                        */
/*                                                 */
/*                                                 */
/***************************************************/

double Dconv(double r,int id){
  complex integralRho;
  double prefactor, alpha, integralV,sum;
  int n,v;
  if (vp == 0){
      integralRho=h1(r/beta,id);
      sum=Cabsqu(integralRho);
  }

  else if (r < vp){
    integralV = 0.0;

    /***************************************************/
    /*                  INTEGRAL A                     */
    /***************************************************/
    for(n=1; n<=NGAUSS_V_INT_A; n++){
      xV_INT_A[n] = (vp-r)*xGaussV_INT_A[n];
      wV_INT_A[n] = (vp-r)*wGaussV_INT_A[n];
      prefactor=wV_INT_A[n] * xV_INT_A[n];
      integralRho=h1beta_INT_A(xV_INT_A[n]/beta,id);
      integralV += prefactor * Cabsqu(integralRho);
    }
    sum = 2.0 * M_PI * integralV;

    integralV = 0.0;
```

```c
/**************************************************/
/*                  INTEGRAL B                    */
/**************************************************/

   for(n=1; n<=NGAUSS_V_INT_B; n++) {
     xV_INT_B[n]=2.0*r*xGaussV_INT_B[n]+(vp-r);
     wV_INT_B[n]=2.0*r*wGaussV_INT_B[n];


     if((SQR(xV_INT_B[n])+SQR(r)-SQR(vp))/(2.0*r*xV_INT_B[n])>1.0){
integralV=0.0;
     }

     else
{
  alpha = acos((SQR(xV_INT_B[n])+SQR(r)-SQR(vp)) / (2.0*r*xV_INT_B[n]));
  prefactor=wV_INT_B[n] * xV_INT_B[n] * alpha;

  integralRho=h1beta_INT_B(xV_INT_B[n]/beta,id);
  integralV += prefactor * Cabsqu(integralRho);

}
   }

   sum += 2.0 * integralV;

 }

 else {
   integralV = 0.0;
/**************************************************/
/*                  INTEGRAL C                    */
/**************************************************/

   for(n=1; n<=NGAUSS_V_INT_C; n++){
     xV_INT_C[n]=2.0*vp*xGaussV_INT_C[n]+(r-vp);
     wV_INT_C[n]=2.0*vp*wGaussV_INT_C[n];

     if((SQR(xV_INT_C[n])+SQR(r)-SQR(vp))/(2.0*r*xV_INT_C[n])>1.0){
integralV=0.0;
     }

     else{
alpha = acos((SQR(xV_INT_C[n])+SQR(r)-SQR(vp)) / (2.0*r*xV_INT_C[n]));
prefactor=wV_INT_C[n] * xV_INT_C[n] * alpha;
integralRho=h1beta_INT_C(xV_INT_C[n]/beta,id);
integralV += prefactor * Cabsqu(integralRho);
     }
   }
   sum = 2.0 * integralV;
 }
 return(sum);
}
```

Bibliography

[1] M. Born and E. Wolf, *Principles of Optics*, Pergamon Press, 1990.

[2] E. Hecht, *Optics*, Addison-Wesley, third ed., 1998.

[3] I. M. Watt, *The Principles and Practice of Electron Microscopy*, Cambridge University Press, Sydney, second ed., 1997.

[4] S. M. McMurry, *Quantum Mechanics*, Addison-Wesley, 1993.

[5] D. W. Pohl, W. Denk, and M. Lanz, "Optical stethoscopy image recording with resolution $\lambda/2$," *Appl. Phys. Lett.* **44**, pp. 651–653, 1984.

[6] A. Lewis, M. Isaacson, A. Harootunian, and A. Muray, "Development of a 500 Å spatial resolution light microscope," *Ultramicroscopy* **13**(227), 1984.

[7] T. R. Corle and G. S. Kino, *Confocal Scanning Optical Microscopy and Related Imaging Systems*, Academic Press, San Diego, 1996.

[8] J. Z. Young and F. Roberts, "A flying-spot microscope," *Nature* **167**(231), 1951.

[9] M. Minsky, "Microscopy apparatus," Dec. 19, 1961. US Patent No. 3,013,467.

[10] M. Minsky, "Memoir on inventing the confocal scanning microscope," *Scanning* **10**, pp. 128–138, 1988.

[11] T. Wilson and C. Sheppard, *Theory and Practice of Scanning Optical Microscopy*, Academic Press, London, 1984.

[12] W. Lukosz, "Optical systems with resolving powers exceeding the classical limit," *J. Opt. Soc. Am.* **56**, pp. 1463–1472, 1966.

[13] T. Wilson, *Confocal Microscopy*, Academic Press, London, 1990.

[14] D. T. Fewer, *Confocal Microscopy: Real-Time Imaging and Applications*. PhD thesis, Trinity College Dublin, 1998.

[15] I. J. Cox and C. J. R. Sheppard, "Scanning optical microscopes incorporating a digital framestore and microcomputer," *Applied Optics* **22**, pp. 1474–1478, 1983.

[16] D. K. Hamilton and T. Wilson, "Scanning optical microscopy by objective lens scanning," *J. Phys. E:Sci. Intrum.* **19**, pp. 52–54, 1982.

[17] K. Carlsson, K. Danielsson, P. E. Lenz, R. Liljeborg, A. Majlöf, and N. Åslund, "Three-dimensional microscopy using a confocal laser scanning microscope," *Optics Letters* **10**, pp. 53–55, 1985.

[18] T. Suzuki and Y. Horikawa, "Development of a real-time scanning laser microscope for biological use," *Applied Optics* **25**, pp. 4115–4121, 1986.

[19] M. D. Egger and M. Petráň, "New reflected-light microscope for viewing unstained brain and ganglion cells," *Science* **157**, pp. 305–307, 1967.

[20] M. Petráň, M. Hadravský, M. D. Egger, and R. Galambos, "Tandem-scanning reflected-light microscope," *J. Opt. Soc. Am.* **58**(5), pp. 90–93, 1968.

[21] P. Nipkow, "Kaiserliches patentamt," Jan. 6, 1884. Patentschrift Nr. 30,104.

[22] G. Q. Xiao, T. R. Corle, and G. S. Kino, "Real-time confocal scanning optical microscope," *Appl. Phys. Lett.* **53**, pp. 716–718, 1988.

[23] A. Boyde, M. Petráň, and M. Hadravský, "Tandem scanning reflected-light microscope of internal features in whole bone and tooth samples," *J. Microsc.* **132**, pp. 1–7, 1983.

[24] A. Boyde, S. J. Jones, M. L. Taylor, L. A. Wolfe, and T. F. Watson, "Fluorescence in the tandem scanning microscope," *J. Microsc.* **157**, pp. 39–49, 1990.

[25] E. M. McCabe, D. T. Fewer, A. C. Ottewill, S. J. Hewlett, and J. Hegarty, "Direct-view microscopy: optical sectioning strength for finite sized, multiple-pinhole arrays," *J. Microsc.* **184**(1), pp. 95–105, 1996.

[26] S. C. Baer, "Optical apparatus providing focal-plane-specific illumination," 1970. US Patent No. 3,547,512.

[27] S. Yin, G. Lu, J. Zhang, F. T. S. Yu, and J. N. Mait, "Kinoform-based nipkow disc for a confocal microscope," *Applied Optics* **34**, pp. 5695–5698, 1995.

[28] T. Wilson, R. Juškaitis, M. A. A. Neil, and M. Kozubek, "Confocal microscopy by aperture correlation," *Optics Letters* **21**(23), pp. 1879–1881, 1996.

[29] R. Juškaitis, T. Wilson, M. A. A. Neil, and M. Kozubek, "Efficient real-time confocal microscopy with white light sources," *Nature* **383**, pp. 804–806, 1996.

[30] S. J. Hewlett, D. T. Fewer, and E. M. McCabe, "Influence of source coherence and aperture distribution on the imaging properties in direct-view microscopy," *J. Opt. Soc. Am. A* **14**(5), pp. 1066–1075, 1997.

[31] D. T. Fewer, S. J. Hewlett, and E. M. McCabe, "Imaging in fluorescence direct-view microscopy," *Optics Comms.* **152**(4-6), pp. 393–402, 1998.

[32] C. J. R. Sheppard and T. Wilson, "The theory of the direct-view confocal microscope," *J. Microsc.* **124**, pp. 107–117, 1981.

[33] T. Wilson and S. J. Hewlett, "Optical sectioning strength of the direct-view microscope employing finite-sized pin-hole arrays," *J. Microsc.* **163**(2), pp. 131–150, 1991.

[34] H. von Helmholtz *J. f. Math.* **57**(7), 1859.

[35] J. W. Goodman, *Introduction to Fourier Optics*, McGraw-Hill, second ed., 1996.

[36] I. J. Cox, C. J. R. Sheppard, and T. Wilson, "Super-resolution by confocal fluorescent microscopy," *Optik* **60**, pp. 391–396, 1982.

[37] G. J. Brakenhoff, "Imaging modes of confocal scanning light microscopy," *J. Microsc.* **117**, pp. 233–242, 1979.

[38] G. J. Brakenhoff, P. Blom, and P. Barends, "Confocal scanning light microscopy with high aperture immersion lenses," *J. Microsc.* **117**, pp. 233–242, 1979.

[39] M. Glass and T. Dabbs, "The experimental effect of detector size on confocal lateral resolution," *J. Microsc.* **164**(2), pp. 153–158, 1991.

[40] D. T. Fewer, S. J. Hewlett, E. M. McCabe, and J. Hegarty, "Direct-view microscopy: experimental investigation of the dependence of the optical sectioning characteristics on pinhole-array configuration," *J. Microsc.* **187**(1), pp. 54–61, 1997.

[41] H. H. Hopkins, "The frequency response of a defocused optical system," *Proc. Roy. Soc. A, (Royal Society of London)* **231**, pp. 91–103, 1955.

[42] F. W. D. Rost, *Fluorescence Microscopy*, vol. 1, Cambridge University Press, Sydney, 1995.

[43] J. B. Pawley, *Handbook of Biological Confocal Microscopy*, Plenum Press, New York, 1995.

[44] T. Tanaami, Y. Sugiyama, and K. Mikuriya, "High speed confocal laser microscopy," *Yokogawa technical report* **19**, pp. 7–10, 1994.

[45] A. H. Buist, M. Müller, J. Squier, and G. J. Brakenhoff, "Real-time two-photon absorption using multipoint excitation," *J. Microsc.* **192**, pp. 217–226, 1998.

[46] M. Straub and S. W. Hell, "Multifocal multiphoton microscopy: a fast and efficient tool for 3-D fluorescence imaging," *Bioimaging* **6**, pp. 177–185, 1998.

[47] W. Denk, J. H. Strickler, and W. W. Webb, "Two-photon laser scanning fluorescence microscopy," *Science* **248**, pp. 73–76, 1990.

[48] T. Nielsen, M. Fricke, D. Hellweg, and P. Andresen, "High efficiency beam splitter for multifocal multiphoton microscopy," *J. Microsc.* **201**(3), pp. 368–376, 2000.

[49] A. Egner and S. W. Hell, "Time multiplexing and parallelization in multifocal multiphoton microscopy," *J. Opt. Soc. Am. A.* **17**(7), pp. 1192–1201, 2000.

[50] M. Schrader, U. G. Hofmann, and S. W. Hell, "Ultrathin fluorescent layers for monitoring the axial resolution in confocal and two-photon fluorescence microscopy," *J. Microsc.* **191**(2), pp. 135–140, 1998.

[51] Q. S. Hanley, P. J. Verveer, M. J. Gemkow, and T. M. Jovin, "An optical sectioning programmable array microscope implemented with a digital micromirror device," *J. Microsc.* **196**(3), pp. 317–331, 1999.

[52] S. W. Hell, G. Reiner, C. Cremer, and E. H. K. Stelzer, "Aberrations in confocal fluorescence microscopy induced by mismatches in refractive index.," *J. Microsc.* **169**, pp. 391–405, 1993.

[53] H. Ling and S.-W. Lee, "Focusing of electromagnetic waves through a dielectric interface," *J. Opt. Soc. Am. A.* **1**(9), pp. 965–973, 1984.

[54] T. D. Visser and S. H. Wiersma, "Spherical aberration and the electromagnetic field in high-aperture systems," *J. Opt. Soc. Am. A.* **8**, pp. 1404–1410, 1991.

[55] P. Török, P. Varga, Z. Laczik, and G. R. Booker, "Electromagnetic diffraction of light focused through a planar interface between materials of mismatched refractive indices: an integral representation," *J. Opt. Soc. Am. A.* **12**(2), pp. 325–332, 1995.

[56] S. Kimura and C. Munakata, "Depth resolution of the fluorescent confocal scanning optical microscope," *Applied Optics* **29**(4), pp. 489–494, 1990.

[57] T. Wilson and A. R. Carlini, "Size of the detector in confocal imaging systems.," *Optics Letters* **12**, pp. 227–229, 1987.

[58] P. Török, S. J. Hewlett, and P. Varga, "The role of specimen-induced spherical aberration in confocal microscopy," *J. Microsc.* **188**(2), pp. 158–172, 1997.

[59] P. Török, P. Varga, and G. Németh, "Analytical solution of the diffraction integrals and interpretation of wave-front distortion when light is focused through a planar interface between materials of mismatched refractive indices," *J. Opt. Soc. Am. A.* **12**(12), pp. 2660–2671, 1995.

[60] P. S. Pacheco, *Parallel Programming with MPI*, Morgan Kaufman, San Francisco, CA, 1997.

[61] J. F. Rabek, *Experimental methods in polymer chemistry: physical principles and applications*, Wiley-Interscience, 1980.

[62] D. T. Fewer, S. J. Hewlett, and E. M. McCabe, "Laser sources in direct-view-scanning, tandem-scanning, or nipkow-disk-scanning microscopy," *Applied Optics* **37**(2), pp. 380–385, 1998.

[63] C. M. Taylor, P. J. Smith, and E. M. McCabe, "A programmable array microscope demonstrator : Application of a ferroelectric liquid crystal SLM," in *Three-Dimensional and Multidimensional Microscopy: Image Acquisition Processing VII, José-Angel Conchello, Carol J. Cogswell, Tony Wilson, Editors*, vol. 3919 of *Proceedings of SPIE*, pp. 21–29, 2000.

[64] P. J. Smith, C. M. Taylor, A. J. Shaw, and E. McCabe, "Programmable array microscopy using a ferroelectric liquid crystal SLM," *Applied Optics* **39**(16), pp. 2664–2669, 2000.

[65] C. M. Taylor and E. M. McCabe, "Programmable array microscope employing two ferroelectric liquid crystal spatial light modulators," in *Three-Dimensional and Multidimensional Microscopy: Image Acquisition Processing VIII, José-Angel Conchello, Carol J. Cogswell, Tony Wilson, Editors*, vol. 4261 of *Proceedings of SPIE*, pp. 33–39, 2001.

[66] IBM Corporation, "Electronically scanned confocal imaging system," *IBM Technical Disclosure Bulletin* **36**(06B), pp. 261–262, 1993.

[67] M. Liang, R. L. Stehr, and A. W. Krause, "Confocal pattern period in multiple-aperture confocal imaging systems with coherent illumination," *Optics Letters* **22**(11), pp. 751–753, 1997.

[68] L. A. Yoder *Adv. Imaging* **11**(6), 1996.

[69] S. Chandrasekhar, *Liquid Crystals*, Cambridge university press, 2nd ed., 1992.

[70] P. J. Verveer, Q. S. Hanley, P. W. Verbeek, L. J. van Vliet, and T. M. Jovin, "Theory of confocal fluorescence imaging in the programmable array microscope (PAM)," *J. Microsc.* **189**(3), pp. 192–198, 1998.

[71] Q. S. Hanley, P. J. Verveer, and T. M. Jovin, "Spectral imaging in a programmable array microscope by Hadamard transform fluorescence spectroscopy," *Applied Spectroscopy* **53**(1), pp. 1–10, 1999.

[72] Displaytech Inc., 2602 Clover Basin Drive, Longmont, CO 80503, *SLM Developer Kit User's Manual*, 1997.

[73] Displaytech Inc., 2602 Clover Basin Drive, Longmont, CO 80503, *Ferroelectric Liquid Crystal Light Valves; User's Manual*, Jan. 1996.

[74] T. Wilson and A. R. Carlini, "The effect of aberrations on the axial response of confocal imaging systems," *J. Microsc.* **154**(3), pp. 243–256, 1989.

[75] H. J. Matthews, D. K. Hamilton, and C. J. R. Sheppard, "Aberration measurement by confocal interferometry," *Journal of Modern Optics* **36**(2), pp. 233–250, 1989.

[76] M. J. E. Golay, "Multi-slit spectrometry," *J. Opt. Soc. Am.* **39**(6), pp. 437–444, 1949.

[77] M. Harwit and N. J. A. Sloane, *Hadamard Transform Optics*, Academic, New York, 1979.

[78] J. R. Leger, J. Schuler, N. Morphis, and R. Knowlden, "Optical antialiasing filters based on complementary Golay codes," *J. Opt. Soc. Am.* **36**(20), pp. 4692–4701, 1997.

[79] H. Talbot, "Facts relating to optical science 4," *Phil. Mag.* **9**, pp. 401–409, 1836.

[80] D. Daly, *Microlens arrays*, Taylor & Francis, London and New York, 1st ed., 2001.

[81] L. G. Commander, S. E. Day, C. H. Chia, and D. R. Selviah, "Microlenses immersed in nematic liquid crystal with electrically controllable focal length," in *Third European Optical Society 'Microlens Arrays' Topical Meeting*, vol. 5, pp. 72–75, 1995.

[82] H. J. Tiziani and H.-M. Uhde, "Three-dimensional analysis by a microlens-array confocal arrangement," *Applied Optics* **33**(4), pp. 567–572, 1994.

[83] H. J. Tiziani, R. Achi, R. N. Krämer, and L. Wiegers, "Theoretical analysis of confocal microscopy with microlenses," *Applied Optics* **35**(1), pp. 120–125, 1996.

[84] A. F. Gmitro and D. Aziz, "Confocal microscopy through a fiber-optic imaging bundle," *Optics Letters* **18**(8), pp. 565–567, 1993.

[85] R. Juškaitis, T. Wilson, and T. F. Watson, "Real-time white light reflection confocal microscopy using a fibre-optic bundle," *Scanning* **19**, pp. 15–19, 1996.

[86] Y. S. Sabharwal, A. R. Rouse, L. Donaldson, M. F. Hopkins, and A. F. Gmitro, "Slit-scanning confocal microendoscope for high-resolution *in vivo* imaging," *Applied Optics* **38**(34), pp. 7133–7144, 1999.

[87] E. McCabe, "Optical imaging systems," Apr. 4, 2001. Irish patent No. S99 0004.

[88] L. G. Commander, S. E. Day, and D. R. Selviah, "Variable focal length microlenses," *Optics Comms.* **177**, pp. 157–170, 2000.

[89] "BBC web archive: http://www.bbc.co.uk/qed/superspecs.shtml." Adspecs production office, Oxford centre of innovation, Mill St., Oxford, OX2 OJX.

[90] M. Chang, "Total internal reflection lens," *Applied Optics* **24**(9), pp. 1256–1259, 1985.

[91] D. W. Berreman, "Variable focus liquid crystal lens system," 1980. US Patent No. 4,190,330.

[92] I. C. Khoo and S. T. Wu, *Optics and nonlinear optics of liquid crystals*, World scientific publishing, Singapore, 1st ed., 1993.

[93] S. Nose, S. Masuda, and S. Sato, "Optical properties of a liquid crystal microlens with a symmetric electrode structure," *Jpn. J. Appl. Phys.* **30**(12b), pp. 2110–2112, 1991.

[94] S. Kimura and T. Wilson, "Confocal scanning optical microscope using single-mode optical fibre for detection," *Applied Optics* **30**(16), pp. 2143–2150, 1991.

[95] T. Dabbs and M. Glass, "Fiber optic confocal microscope: FOCON," *Applied Optics* **31**(16), pp. 3030–3035, 1992.

[96] T. Wilson, "Image formation in two-mode fibre-based confocal microscopes," *J. Opt. Soc. Am. A.* **10**, pp. 1535–1543, 1993.

[97] L. G. Commander, S. E. Day, and D. R. Selviah, "Electrode designs for tunable microlenses," in *Fourth European Optical Society 'Microlens Arrays' Topical Meeting*, pp. 48–53, 1997.

[98] L. G. Commander, *Variable Focal Length Liquid Crystal Immersed Microlenses*. PhD thesis, University of London, 1998.

[99] A. J. Weir, *Lebesgue integration and measure*, Cambridge university press, 1973.

[100] M. R. Spiegel, *Theory and problems of advanced calculus*, McGraw-Hill book company, metric ed., 1974.

[101] M. Abramowitz and I. A. Stegun, *Handbook of mathematical functions*, New-York: Dover, 1965.

Publications

P. J. Smith, C. M. Taylor and E. M. McCabe, "Optical Sectioning Using Finite-Sized, Multiple Aperture Arrays in Fluorescence Direct-View Microscopy; Experimental Results", in Three-Dimensional and Multidimensional Microscopy: Image Acquisition Processing VI, José-Angel Conchello, Carol J. Cogswell, Tony Wilson, Editors, Proceedings of SPIE **3605**, pp. 236-240, 1999.

C. M. Taylor, P. J. Smith and E. M. McCabe, "A Programmable Array Microscope Demonstrator : Application of a Ferroelectric Liquid Crystal SLM", in Three-Dimensional and Multidimensional Microscopy: Image Acquisition Processing VII, José-Angel Conchello, Carol J. Cogswell, Tony Wilson, Editors, Proceedings of SPIE **3919**, pp. 21-29, 2000.

P. J. Smith, C. M. Taylor, E. M. McCabe, D. R. Selviah, S. E. Day, L. G. Commander, "Variable-focus microlenses as a potential technology for endoscopy" in Three-dimensional and Multidimensional Microscopy: Image Acquisition Processing VII, José-Angel Conchello, Carol J. Cogswell, Tony Wilson, Editors, Proceedings of SPIE **3919**, pp. 187-192, 2000.

P. J. Smith, C. M. Taylor, A. J. Shaw and E. M. McCabe,"Programmable Array Microscopy using a Ferroelectric Liquid Crystal SLM", Applied Optics **39**(16), pp. 2664-2669, 2000.

C. M. Taylor and E. M. McCabe. "Programmable Array Microscope employing two ferroelectric liquid crystal spatial light modulators", in Three-Dimensional and Multidimensional Microscopy: Image Acquisition Processing VIII, José-Angel Conchello, Carol J. Cogswell, Tony Wilson, Editors, Proceedings of SPIE **4261**, pp. 33-39, 2001.

P. J. Smith, C. M. Taylor, E. M. McCabe, D. R. Selviah, S. E. Day, L. G. Commander. "Switchable fiber coupling using variable-focal-length microlenses". Review of Scientific Instruments **72**(7), pp. 3132-4, July 2001.